OPTICAL PHASED ARRAYS FOR HIGH SPEED, NON-MECHANICAL BEAM STEERING APPLICATIONS

A Dissertation

by

DWAYNE DENTON MACIK

Submitted to the Office of Graduate and Professional Studies of
Texas A&M University
in partial fulfillment of the requirements for the degree of

DOCTOR OF PHILOSOPHY

Chair of Committee,	Christi K. Madsen
Committee Members,	Ohannes Eknoyan
	Jim Ji
	Alexey Belyanin
Head of Department,	Miroslav M. Begovic

August 2017

Major Subject: Electrical Engineering

ABSTRACT

Optical beam steering has many applications ranging from sensing and detecting to light and image projection. A hybrid annealed proton exchange waveguide with a vertically integrated arsenic trisulfide waveguide on a lithium niobate substrate was used to create a low-loss, high-speed optical phased array that allows for the non-mechanical steering of 1550 nm light on an integrated optic platform. The high electro-optic coefficient of the x-cut y-propagating $LiNbO_3$ (r_{33} = 30.8 pm/V) is utilized by electrode structures fabricated on the $LiNbO_3$ substrate to create low-power, low-loss beam steering with high-speed bandwidths, capable of 10 GHz and larger, as demonstrated by commercial $LiNbO_3$ modulators. The introduction of the higher refractive index As_2S_3 waveguide is critical because it leads to a highly confined optical mode. The design, simulation, and fabrication of this device are presented here.

For measurements and as a preliminary proof of concept, two different platforms have been employed in series to leverage EO tuning. An APE:$LiNbO_3$ optical phased array was fabricated and edge coupled to a silicon nitride 8x8 waveguide array that condenses the output pitch and utilizes the Triplex^{TM} waveguide technology. To characterize and tune this device, a 3 lens imaging system was utilized to produce both near- and far- field intensity patterns of the output of the OPA on a static image plane. At the image plane, a high resolution infrared camera was used to observe the resulting intensity pattern. The control software for tuning the OPA can read the intensity incident at a specified position on the detector array, and has an electronically controlled pulse width modulation hardware interface to drive the electro-optic phase shifters. Beam steering was achieved using an iterative tuning algorithm to maximize the intensity at a specified location.

DEDICATION

To my family

ACKNOWLEDGEMENTS

I would like to thank my committee chair and advisor, Dr. Christi K. Madsen, for the opportunity to pursue this advanced degree in her research group and the knowledge she has provided over the years. I would also like to acknowledge Dr. Ohannes Eknoyan, Dr. Jim Ji, and Dr. Alexey Belyanin for serving on my committee and for taking the time to provide insightful discussions on my work. I thank Chen Zhang for helping in the lab and for being a friend. I thank Tyler Bravo for writing the software used for measurements. I would also like to thank Yuxiao Liu and Ran Huang for their help and friendships.

I thank my mom and dad for instilling hard work and dedication in me and for encouraging me to set my goals and to never give up. I thank my sister for her support and belief in me. Lastly, I thank my wife for always being there, for all her love, and for putting her degree on hold while I complete mine.

CONTRIBUTORS AND FUNDING SOURCES

Contributors

This work was supervised by a dissertation committee consisting of advisor Professor Christi K. Madsen and Professors Ohannes Eknoyan and Jim Ji of the Department of Electrical Engineering and Professor Alexey Belyanin of the Department of Physics.

The electron beam lithography in Chapter 3 was carried out at the University of Houston with the help of Chen Zhang. The measurement software used in Chapter 4 was developed by Tyler Bravo. The Si_3N_4 waveguide arrays used in Chapter 4 were fabricated by Lionix BV and use the Triplex^{TM} waveguide technology.

All other work for the dissertation was completed by the student, under the advisement of Dr. Christi K. Madsen of the Department of Electrical Engineering.

Funding Sources

This work was made possible in part by the Missile Defense Agency under Grant Number HQ0147-12-C-6018.

Its contents are solely the responsibility of the authors and do not necessarily represent the official views of the Missile Defense Agency.

NOMENCLATURE

ACPS	Asymmetric coplanar strip
Al	Aluminum
APE	Annealed proton exchange
APE:$LiNbO_3$	APE diffused waveguide ($LiNbO_3$ substrate)
As_2S_3	Arsenic trisulfide
BOE	Buffered oxide etch
Cr	Chromium
CPW	Coplanar waveguide
DC	Direct current
DI	Deionized
DUT	Device under test
DOF	Degrees of freedom
EBL	Electron beam lithography
EO	Electro-optic
FDM	Finite difference method
FMM	Film mode matching
GDSII	Graphic Database System
IR	Infrared
LC	Liquid crystal
$LiNbO_3$	Lithium niobate

MFD	Mode field diameter
NA	Numerical aperture
NMBS	Non-mechanical beam steering
OPA	Optical phased array
OPL	Optical path length
OVA	Optical vector analyzer
PCB	Printed circuit board
PIN	P-doped:intrinsic:N-doped (modulator)
PLC	Planar lightwave circuit
PMMA	Polymethyl methacrylate
PWM	Pulse width modulation
RF	Radio frequency
RIE	Reactive ion etch
SEM	Scanning electron microscopy
SiO_2	Silicon dioxide
Si_3N_4	Silicon nitride
SOI	Silicon-on-insulator
Ti	Titanium
TO	Thermo-optic
W	Tungsten

TABLE OF CONTENTS

Page

LIST OF FIGURES

Page

LIST OF TABLES

Page

CHAPTER I

INTRODUCTION*

I.A. Background and Literature Review

Free-space optical beam steering, by means of optical phased arrays, has made tremendous strides in recent years. One reason for this progress is that optical systems are not hindered by electromagnetic interference and, therefore, can be utilized in sensing and signal processing applications. Conventional mechanical approaches, such as microelectromechanical (MEMs) mirrors [1], have shortcomings, particularly with the unreliability of moving parts and relatively slow steering speeds. The non-mechanical approach, as presented here, can even further improve the reliability and usefulness of these applications compared with these mechanical approaches.

Non-mechanical beam steering using OPAs has been employed by many different technologies over the years. Devices based on liquid crystal technology [2-3] that allow for wide steering angles have been developed, but have slow steering speeds and require multiple stages (or cascading), which provides added complexity to the manufacturing of the device. For example, Kim et al. use an LC device that allows for high steering angles of ±15°, but Resler et al. show that liquid crystal devices exhibit slow steering speeds that are orders of magnitudes lower than competing technologies.

---

* Part of the data reported in this chapter is reprinted from D. D. Macik and C. K. Madsen, "Fabrication of $LiNbO_3$-As_2S_3 waveguides for beam steering applications," *Proc. SPIE*, vol. 9970, pp. 99700H-1 – 99700H-10, 2016 and D. D. Macik, T. E. Bravo, S. M. Pentecost, F. A. Espinal, and C. K. Madsen, "Optimization of electro-optic phase shifters for integrated optical phased arrays," *Proc. SPIE*, vol. 10181, pp. 1018105-1 – 1018105-10, 2017.

Another technology that draws much attention for its use with NMBS applications is the silicon-on-insulator platform [4-11]. While this type of device is fabricated on a single chip and some of these SOI devices allow for two-dimensional steering of the output beam, most lack in steering speed due to the use of thermo-optic phase shifters that cause these speeds to suffer. The approach by Doylend et al. makes use of a small lateral waveguide pitch, which permits a higher steering angle, but requires a high 2π-power of 215±15 mW with the use of slow TO phase shifters. The non-uniform output waveguides used by Hutchison et al. have further increased the steering angle to 80° on this platform. This non-uniformity of the output array elements causes the grating lobes to be suppressed, which allows the main lobe to be steered throughout the entire element factor without power transferring to the grating lobes. However, more noise is introduced into the system because this design permits increased side lobe levels. The use of relatively slow TO phase shifters with inefficient 2π-power of 160 mW also hinders the performance of this device. The use of PIN modulators by Aflatouni et al. has alleviated much of the speed issues, but higher losses are introduced into the optical circuit. PIN modulators consist of an intrinsic semiconductor surrounded by a p-doped and an n-doped area. This area is within the guiding region of the device and uses the free carrier plasma dispersion effect to modulate the optical signal.

The use of Silicon nitride devices has also been employed in NMBS applications. These devices are fabricated with the Triplex$^{\mathrm{TM}}$ [12] waveguide technology and make use of ring resonators to build a beamforming [13-15] network. These devices, however, are used on the receiving end of a ku-band antenna array.

The various platforms mentioned above lack in steering speeds, but this can be improved by means of NMBS using lithium niobate optical phased arrays [16-19]. These devices take advantage of the high electro-optic coefficient of $LiNbO_3$, which allows for a π-phase shift at lower voltages and much faster steering speeds. Although faster steering speeds result with the use $LiNbO_3$ OPAs, all that have been previously fabricated require fiber arrays to be coupled to the output waveguides for optical processing. The main reason for this is that diffused waveguides, which are typically fabricated on a $LiNbO_3$ substrate, have large optical mode sizes that require a large waveguide pitch. This large pitch greatly reduces the achievable maximum steering angle.

Table I displays a comparison of a number of different platforms used for NMBS by summarizing the most important parameters that contribute to the device's performance. N is the number of array elements in the array and helps determine the array factor width (far-field beam width) which is approximately $\psi = (\lambda/Nd)(180°/\pi)$. A number of array elements is not included with the LC platform because these devices are not based on optical phased arrays. The waveguide pitch, d, determines the maximum steering angle of the array where the 2π-steering range is approximately $\theta_{max} = (\lambda/d)(180°/\pi)$. While the high number of array elements used on the uniform silicon-on-insulator platform leads to a smaller far-field beam width, the decreased pitch of the array elements in our hybrid As_2S_3 – $LiNbO_3$ device leads to an increased maximum steering angle.

High steering speeds are important in applications, such as sensing and signal processing. The technologies listed in Table I, other than those used on the $LiNbO_3$

platform, use phase modulation techniques, such as TO or PIN modulators. These platforms have demonstrated speeds up to only the MHz range. However, commercially available $LiNbO_3$ modulators for telecommunication applications are already capable of speed bandwidths of 10 GHz and larger.

Table I
Comparison of NMBS OPA parameters and results from various platforms [21]

Platform	**N**	**d**	**θ_{max}**	**Speed**
LC	-	-	30° [3] (λ=1.55 μm)	1 Hz [2]
SOI	16 [6]	3.5 μm [6]	25° [6] (λ=1.555 μm)	7.3 kHz [8] (TO) 200 MHz [10] (PIN)
SOI (non-uniform)	128 [11]	-	80° [11] (λ=1.27 μm)	- (TO) [11]
$LiNbO_3$ **(output to fiber array)**	8 [16]	250 μm [16]	0.3° [16] (λ=1.32 μm)	18 GHz [16]
InP	8 [22]	5.5 μm [22]	16° [22] (λ=1.54 μm)	1 MHz [22]
Si_3N_4	8 [15]	-	- Off-chip (λ=2.8-2.35cm) [15]	- (TO) [15]
As_2S_3-$LiNbO_3$	8 [20]	2.6 μm [20]	34° (λ=1.55 μm) [20]	18 GHz [16]
$LiNbO_3$/Si_3N_4	8 [21]	6.2 μm [21]	14° (λ=1.55 μm) [21]	18 GHz [16]

In this work, x-cut y-propagating lithium niobate is used to form a low-loss hybrid annealed proton exchange – arsenic trisulfide optical phased array on a single chip. Our hybrid As_2S_3 – $LiNbO_3$ OPA provides a vertically integrated platform for accomplishing both electro-optic control and makes use of the tight mode confinement of As_2S_3 for closer waveguide pitch, which leads to higher maximum steering angles. A diffused APE optical phased array with 127µm input and output pitch is also fabricated on this substrate. Both OPAs use the high electro-optic coefficient (r_{33} = 30.8 pm/V) of lithium niobate, enabling fast phase shifting for high speed non-mechanical beam steering. As a preliminary proof-of-concept, the latter is coupled to a Triplex^{TM} Si_3N_4 waveguide array with an output pitch of 6.2µm. Control software is used to tune each element of the array in order to optimize the far-field intensity pattern and steer the beam to a desired angle. This allows for both fast steering speeds and moderately wide steering angles.

I.B. Organization of Dissertation

This dissertation is organized in chapters that help develop an understanding of the working principles of non-mechanical beam steering through the use of optical phased arrays and how this device is fabricated. The following chapters include the theory behind this work, the fabrication of a NMBS OPA, and the measurements/results obtained from a fabricated OPA.

Chapter 1 includes the background of non-mechanical beam steering devices and a short literature review on different platforms that have been used to realize this NMBS. This chapter also provides the organization of this dissertation.

To give better insight of the working principles, chapter 2 explains the theory behind all of the components that make up our hybrid As_2S_3 – $LiNbO_3$ OPA. The relevant properties of lithium niobate are discussed along with the theory of optical waveguides.

Coupled mode theory and the electro-optic effect are also explained. These separate components lead to the overall theory of optical phased arrays. This chapter also includes simulations of different parts of the optical phased array from the annealed proton exchange waveguides to the As_2S_3 waveguides and from the As_2S_3 tapers to the aluminum electrodes. The overall phased array is also simulated to show the performance with different parameters.

Chapter 3 describes the fabrication process of the As_2S_3 – $LiNbO_3$ OPA. The three main fabrication stages, which include the fabrication of the annealed proton exchange waveguides, the arsenic trisulfide waveguides, and the aluminum electrodes, are explained thoroughly from wafer dicing to the last step of sample polishing.

Chapter 4 contains an in depth look at the measurement setup, which includes staging, a Fourier optics system, and voltage control hardware and software. Measurement results obtained from the optical phased array are also discussed and compared to simulation results.

Chapter 5 includes the conclusion that summarizes the research of this dissertation. This chapter also contains a section of future work that can help reduce fabrication times and improve the overall performance of the device.

CHAPTER II

DEVICE THEORY AND SIMULATIONS*

A fundamental understanding of the device theory is essential to comprehend the working principles of an optical phased array used for non-mechanical beam steering. Therefore, wave theory and, in particular, wave guiding in uniaxial crystals is explained in this chapter. This will lead to coupled mode theory as well as the electro-optic effect that is taken advantage of in the phase tuning of the OPAs.

II.A. Wave Theory in Dielectric Waveguides

The differential form of Maxwell's equations in a time varying situation written in terms of the electric field **E** (V/m), magnetic flux density **B** (Wb/m^2), magnetic field **H** (A/m), and electric flux density **D** (C/m^2), are given by [23]

$$\nabla \times \mathbf{E} = -\frac{\partial \mathbf{B}}{\partial t} \tag{1}$$

$$\nabla \times \mathbf{H} = \mathbf{J} + \frac{\partial \mathbf{D}}{\partial t} \tag{2}$$

$$\nabla \cdot \mathbf{D} = \rho_v \tag{3}$$

$$\nabla \cdot \mathbf{B} = 0 \tag{4}$$

---

* Part of the data reported in this chapter is reprinted from D. D. Macik and C. K. Madsen, "Fabrication of LiNbO$_3$-As$_2$S$_3$ waveguides for beam steering applications," *Proc. SPIE*, vol. 9970, pp. 99700H-1 – 99700H-10, 2016.

where ρ_v is the volume density of free charges and **J** is the density of free currents. When in a lossless source-free nonconducting medium (1)-(4), reduce to

$$\nabla \times \mathbf{E} = -\mu \frac{\partial \mathbf{H}}{\partial t} \tag{5}$$

$$\nabla \times \mathbf{H} = \varepsilon \frac{\partial \mathbf{E}}{\partial t} \tag{6}$$

$$\nabla \cdot \mathbf{E} = 0 \tag{7}$$

$$\nabla \cdot \mathbf{H} = 0 \tag{8}$$

where ε and μ are the electric permittivity and magnetic permeability of the medium, respectively. Equations (5)-(8) are first-order differential equations related by the electric and magnetic fields. By taking the curl of (5) and using (6), it becomes

$$\nabla \times \nabla \times \mathbf{E} = -\mu \frac{\partial}{\partial t}(\nabla \times \mathbf{H}) = -\mu\varepsilon \frac{\partial^2 \mathbf{E}}{\partial t^2}\,. \tag{9}$$

Given that $\nabla \times \nabla \times \mathbf{E} = \nabla(\nabla \cdot \mathbf{E}) - \nabla^2 \mathbf{E} = -\nabla^2 \mathbf{E}$ because of (7), (9) becomes

$$\nabla^2 \mathbf{E} - \mu\varepsilon \frac{\partial^2 \mathbf{E}}{\partial t^2} = 0\,. \tag{10}$$

The permittivity, ε, and permeability, μ, are related to their respective free space values $\varepsilon_0 = 8.854 \times 10^{-12}$ (F/m) and $\mu_0 = 4\pi \times 10^{-7}$ (H/m), by

$$\varepsilon = \varepsilon_0 \mathrm{n}^2 \tag{11}$$

$$\mu = \mu_0 \tag{12}$$

and $u_p = 1/\sqrt{\mu\varepsilon} = 1/\mathrm{n}\sqrt{\mu_0\varepsilon_0}$, therefore,

$$\nabla^2 \mathbf{E} - \frac{1}{u_p^2} \frac{\partial^2 \mathbf{E}}{\partial t^2} = 0\,. \tag{13}$$

This same derivation can be done starting with (6), giving

$$\nabla^2\mathbf{H} - \frac{1}{u_p^2}\frac{\partial^2\mathbf{H}}{\partial t^2} = 0\,. \tag{14}$$

Equations (13) and (14) are the homogeneous Helmholtz equations. For optical field solutions, a space and time varying field propagating in the z-direction with propagation constant β can be defined as

$$\mathbf{E}(\mathbf{r},t) = \mathbf{E}(\mathbf{r})e^{j(\mathrm{\omega t}-\mathrm{\beta z})}\,. \tag{15}$$

Solving (13) with (15) and substituting $c = 1/\sqrt{\mu_0\varepsilon_0}$ and $k = n\omega/c$ yields

$$\nabla^2\mathbf{E} + (k^2 - \beta^2)\mathbf{E} = 0\,. \tag{16}$$

The same can be done with the magnetic field and (14) giving

$$\nabla^2\mathbf{H} + (k^2 - \beta^2)\mathbf{H} = 0\,. \tag{17}$$

II.B. Light Propagation in Uniaxial Crystals

Lithium niobate is the substrate of choice in this research because of its favorable optical, electro-optic, and photorefractive properties, among others [24]. It also has a high ferroelectric Curie temperature (approximately 1210°C) [25] that allows for reasonably fast diffusion times at high temperatures. $LiNbO_3$ is a uniaxial anisotropic crystal [26] characterized by the symmetric 3x3 dielectric tensor with axes of an orthogonal coordinate transformed to its principal axes, as follows

$$[\varepsilon] = \begin{bmatrix} \varepsilon_{11} & 0 & 0 \\ 0 & \varepsilon_{22} & 0 \\ 0 & 0 & \varepsilon_{33} \end{bmatrix}. \tag{18}$$

When this dielectric tensor is used with the above-mentioned electric field and electric flux density vectors, the relationship is

$$\mathbf{D} = \varepsilon_0[\varepsilon]\mathbf{E}\,. \tag{19}$$

The electric energy that is stored in a crystal is given by

$$w = \frac{1}{2}\boldsymbol{E} \cdot \boldsymbol{D}\,. \tag{20}$$

Substituting equations (18) and (19) into (20), and representing the electric flux density vector **D** in its vector components gives

$$w = \frac{1}{2\varepsilon_0}\left(\frac{D_x^2}{\varepsilon_{11}} + \frac{D_y^2}{\varepsilon_{22}} + \frac{D_z^2}{\varepsilon_{33}}\right). \tag{21}$$

If $D_i/\sqrt{2\varepsilon_0 w}$ is replaced with *I*, where $i = x, y, z$ and $\varepsilon_{jj} = \mathrm{n}_i^2$ equation (21) becomes

$$\frac{x^2}{\mathrm{n}_x^2} + \frac{y^2}{\mathrm{n}_y^2} + \frac{z^2}{\mathrm{n}_z^2} = 1\,. \tag{22}$$

This is known as the index ellipsoid and has the principal axes *x*, *y*, and *z*. The radii along the directions of these axes are the principal refractive indices n_x, n_y, and n_z, respectively.

Because $LiNbO_3$ has a trigonal crystal structure [27], the index ellipsoid is rotationally symmetric with respect to the *z* axis, or optical axis. This means that $LiNbO_3$ is optically uniaxial [26], where $\mathrm{n}_x = \mathrm{n}_y = \mathrm{n}_o$, $\mathrm{n}_z = \mathrm{n}_e$, and $\mathrm{n}_o > \mathrm{n}_e$. For the two rays of light present that are orthogonal and linearly-polarized in nature, there is only a single direction in which these two waves see the same refractive index, and this is the optical *z* axis. The first light ray is the ordinary ray and is independent of the angle θ, so it always sees the refractive index n_o. This is evident from the index ellipsoid in Fig. 1. The other ray is known as the extraordinary ray and is dependent on the angle θ. The refractive index seen by the extraordinary ray, $n_e(\theta)$, is

$$\begin{cases} \mathrm{n}_e^2(\theta) = y^2 + z^2 \\ z = \mathrm{n}_e(\theta) \cdot \sin(\theta) \end{cases} . \tag{23}$$

Equation (22) can now be written as

$$\frac{x^2}{\mathrm{n}_o^2} + \frac{y^2}{\mathrm{n}_o^2} + \frac{z^2}{\mathrm{n}_e^2} = 1 . \tag{24}$$

The substitution of equation (23) into (24) yields

$$\mathrm{n}_e(\theta) = \frac{\mathrm{n}_e \mathrm{n}_o}{\sqrt{\mathrm{n}_e^2 \cos^2(\theta) + \mathrm{n}_o^2 \sin^2(\theta)}} . \tag{25}$$

From the above equation, the extraordinary wave sees $\mathrm{n}_e(\theta) = \mathrm{n}_e$ at $\theta = 0°$ to $\mathrm{n}_e(\theta) = \mathrm{n}_o$ at $\theta = 90°$.

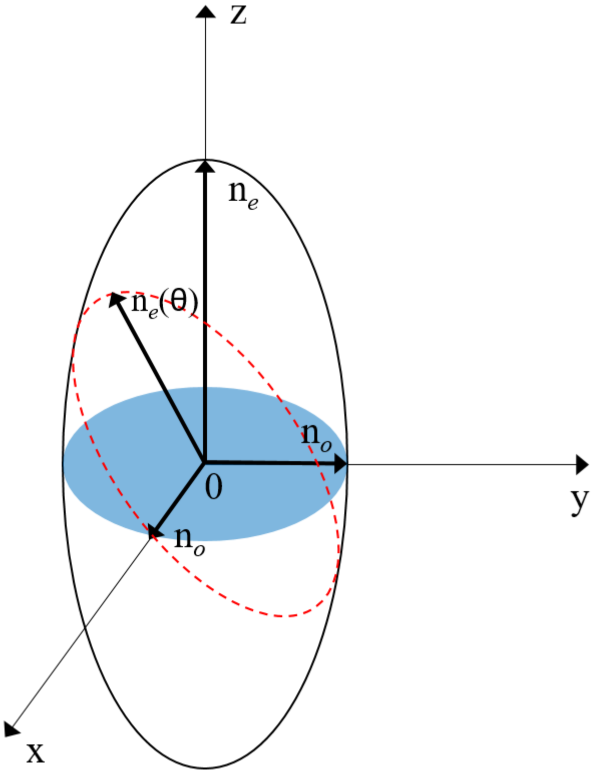

Fig. 1 Index ellipsoid of negative uniaxial crystal.

In x-cut lithium niobate, which is used in this research, the vertically polarized transverse magnetic (TM) mode sees the ordinary index and the horizontally polarized transverse electric (TE) mode sees the extraordinary refractive index, as visualized in Fig. 2.

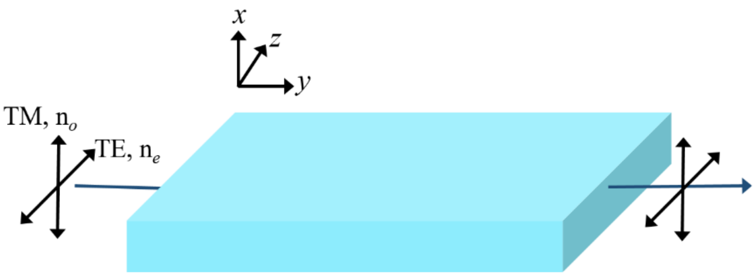

Fig. 2 x-cut y-propagating lithium niobate. The vertically polarized TM mode sees the ordinary index and the horizontally polarized TE mode sees the extraordinary index.

For devices to be designed properly and in order for them to work correctly in the desired spectral area, the wavelength dependent refractive indices must be known. An equation that relates refractive index and wavelength was first put forth by Wolfgang Sellmeier and is known as the Sellmeier dispersion equation. The Sellmeier equation is of the form [28]

$$\mathrm{n}^2(\lambda) = 1 + \frac{C_1\lambda^2}{\lambda^2 - C_2} + \frac{C_3\lambda^2}{\lambda^2 - C_4} + \frac{C_5\lambda^2}{\lambda^2 - C_6} \tag{26}$$

where C_i are the Sellmeier coefficients. Extensive research has been carried out on the refractive indices for specific wavelengths [29] and on the temperature dependence of the indices for various wavelengths [30]. In this research, the telecommunications wavelength of 1.55 µm is used. An infrared corrected Sellmeier equation for the wavelengths from 0.4-5.0 µm has been created [28]. In studies that have used only the single oscillator model of the Sellmeier equation, it has been found that the refractive indices for the respective ends of the spectrum deviate greatly. Therefore, a three oscillator model is used, as in (26), to fit the data from the experiment. This fit produces the Sellmeier coefficients found in Table II.

Table II
Sellmeier Coefficients [10]

Coefficient	**n_o**	**n_e**
C_1	2.6734	2.9804
C_2	0.01764	0.02047
C_3	1.2290	0.5981
C_4	0.05914	0.0666
C_5	12.614	8.9543
C_6	474.6	416.08

When these coefficients are used in (26) with the wavelength of 1.55 μm, $\mathrm{n}_o = 2.2111$ and $\mathrm{n}_e = 2.1376$.

II.C. Step-Index Waveguides

A wave guiding region is created by having a higher index contrast material between two lower index materials. The simplest structure is a slab planar waveguide, which is shown in Fig. 3. To satisfy the wave guiding condition for a region, n_1, $\mathrm{n}_1 > \mathrm{n}_2 \geq \mathrm{n}_3$. In terms of the propagation constant β, this relationship can be expressed as $k_0\mathrm{n}_1 > \beta > k_0\mathrm{n}_2 \geq k_0\mathrm{n}_3$. We can define three constants *q*, *h*, and *p* with the form

$$q \equiv \sqrt{\beta^2 - k_0^2 n_1^2} \tag{27}$$

$$h \equiv \sqrt{k_0^2 n_2^2 - \beta^2} \tag{28}$$

$$p \equiv \sqrt{\beta^2 - k_0^2 n_3^2}\,. \tag{29}$$

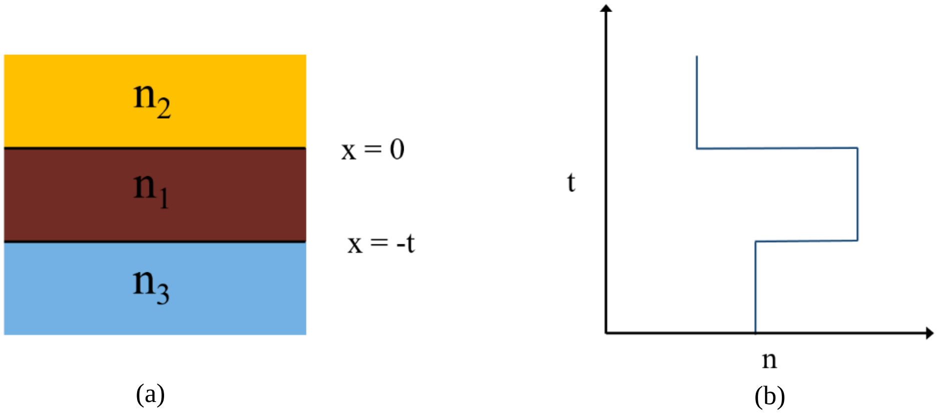

Fig. 3 Planar wave guiding structure. a) Waveguide structure with b) index profile.

For the TE mode, (16) has solutions of the form

$$E_y(x) = \begin{cases} Ae^{-qx} & x > 0 \\ B\cos(hx) + C\sin(hx) & 0 \le x \le -t\,. \\ De^{p(x+t)} & x < -t \end{cases} \tag{30}$$

Applying boundary conditions for continuous electric and magnetic fields gives the eigenvalue equation [26]

$$\tan(ht) = \frac{q+p}{h - \frac{qp}{h}}\,. \tag{31}$$

The simplest way to solve this equation is to plot each side individually and find the intercepts as seen in Fig. 4. The number of intersecting points is the number of modes allowed to propagate in the wave guiding region. Because we are plotting against *h*, these intersecting points give us the allowed h values. Knowing h from (28) and that $\beta = k_0 \mathrm{n}_{eff}$, we can find the effective index from

$$\mathrm{n}_{eff} = \sqrt{\mathrm{n}_2^2 - \left(\frac{h}{k_0}\right)^2}\,. \tag{32}$$

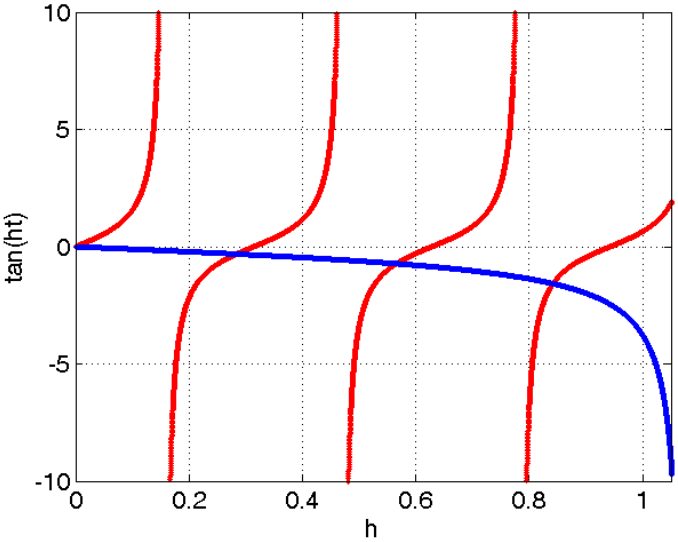

Fig. 4 Eigenvalue equation plotted with the following parameters: λ = 1 μm, $\mathrm{n}_1 = 1.5$, $\mathrm{n}_2 = 1$, $\mathrm{n}_3 = 1.49$, and t = 10 μm.

II.D. Rib Waveguides

Rectangular rib waveguides are 2-D planar waveguides that are of the form as pictured in the drawing in Fig. 5. This configuration is the same as the chalcogenide waveguides used in this research.

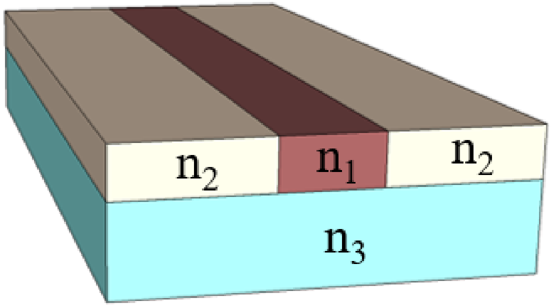

Fig. 5 Rectangular rib waveguide structure.

Because these particular waveguides have this added dimension, there are additional complexities in solving for the modes that are brought about by extra boundary conditions. Methods commonly used for solving for the modes are the Marcatili method [32] and the effective index method [33]. Both of these methods break up the waveguide into a 3x3 grid, as shown in Fig. 6. The wave guiding core is represented by n_1. The cladding layer is separated into equal segments represented by n_2-n_9 and may be the same depending on the device architecture. The main difference in these two methods is that the Marcatili method ignores regions n_2, n_4, n_7, and n_9, whereas the effective index method takes into account all nine regions.

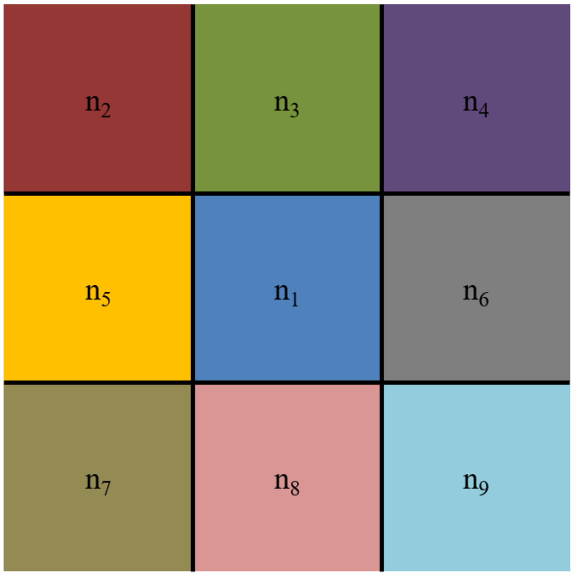

Fig. 6 Grid representation of 2-D rib waveguide.

The Marcatili method works effectively for well-confined modes, but because these outer corner regions are ignored, results deviate greatly for modes that are weakly confined. This method solves the wave equation in each individual region and then adds boundary conditions for the horizontal and vertical directions. Once this is complete, the value for the effective index that satisfies the wave equation for all regions is found.

The effective index method works much better for solving for modes that are weakly confined. This is because all regions are included in the calculations. First, the effective indices for the dimension that limits guiding are found. This is done for each column and leaves a 3x1 grid. The same process is now used on this grid to find the final solutions.

Because these methods are approximate, the FimmWave mode solver package is used to aid in the simulation and design of the devices in this thesis. FimmWave uses mode solving techniques, such as the film mode matching method and the finite difference mode solver. The FMM method is vector based and ideal for rectangular waveguides with small features that can be represented as a finite number of rectangles. The FDM solver is vector based and ideal for high-step refractive index profiles. Various parameters such as refractive index, waveguide dimensions, type of modes to solve for, etc. are entered into the software. FimmWave then solves for the desired number of modes to see each mode's characteristics.

II.E. Diffused Waveguides

Diffused waveguides are similar to rib waveguides, but instead of having a step-index profile, they have a graded-index profile, as seen in Fig. 7. This makes it difficult to identify abrupt boundary positions. As a result, the eigenvalue equation becomes an eigen-integral equation [26].

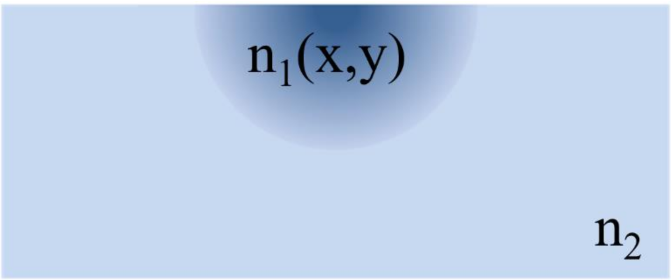

Fig. 7 Diffused waveguide with graded index profile.

For the one dimensional case, the eigen-integral equation is of the form

$$\int_{(x_{t_1})_m}^{(x_{t_2})_m} \sqrt{\mathrm{k}_0^2 \mathrm{n}^2(x) - \beta_m^2}\, dx = \left(m + \frac{1}{2}\right)\pi \qquad m = 1,2,3,\ldots \tag{33}$$

Given that $\beta_m = k_0 \mathrm{n}_{eff,m}$ and $k_0 = 2\pi/\lambda$, (33) becomes

$$\frac{2\pi}{\lambda}\int_{(x_{t_1})_m}^{(x_{t_2})_m} \sqrt{\mathrm{n}^2(x) - \mathrm{n}^2_{eff,m}}\, dx = \left(m + \frac{1}{2}\right)\pi \qquad m = 1,2,3,\ldots \tag{34}$$

where $\mathrm{n}_{eff,m}$ is the effective index of the mode m. With addition of a second dimension, this becomes a double integral, which is more complex to solve. Hence, we use commercially available mode solver packages that quickly carry out these calculations.

II.F. Electro-Optic Tuning

II.F.1. Pockels Effect

In order for steering of the far-field pattern to occur, a voltage must be applied across the output elements to create a refractive index change, which in turn, will induce a phase shift. This phenomenon is known as the linear electro-optic effect, or the Pockels effect, and is found in crystals such as $LiNbO_3$, where the change in refractive index is proportional to an applied electric field [26]. This option for tuning is among the fastest and has inherently low loss, while thermo-optic tuning is commonly used in devices fabricated on silicon, which is an order of magnitude slower [8]. When discussing the Pockels effect, it is more convenient to use the impermeability, *B*.

$$B = \frac{1}{(\varepsilon/\varepsilon_0)} = \frac{1}{\mathrm{n}^2}\,. \tag{35}$$

Equation (24) can, therefore, be expressed as

$$B_{11}x^2 + B_{22}y^2 + B_{33}z^2 + 2B_{23}yz + 2B_{31}zx + 2B_{12}xy = 1\,. \tag{36}$$

When an electric field is applied, the modified index ellipsoid (36) is written as

$$B_1'x^2 + B_2'y^2 + B_3'z^2 + 2B_4'yz + 2B_5'zx + 2B_6'xy = 1\,. \tag{37}$$

The impermeability and the electric field vector, $\mathbf{E}^e$, are related through the electro-optic tensor and is expressed as

$$\Delta B_i = B_i' - B_i = \frac{1}{\mathrm{n}_i^2} = \sum_{j=1}^{3} r_{ij}E_j \tag{38}$$

where r_{ij} is the electro-optic tensor. Written in matrix form, (38) becomes

$$\begin{bmatrix} \Delta\frac{1}{\mathrm{n}_1^2} \\ \Delta\frac{1}{\mathrm{n}_2^2} \\ \Delta\frac{1}{\mathrm{n}_3^2} \\ \Delta\frac{1}{\mathrm{n}_4^2} \\ \Delta\frac{1}{\mathrm{n}_5^2} \\ \Delta\frac{1}{\mathrm{n}_6^2} \end{bmatrix} = \begin{bmatrix} r_{11} & r_{12} & r_{13} \\ r_{21} & r_{22} & r_{23} \\ r_{31} & r_{32} & r_{33} \\ r_{41} & r_{42} & r_{43} \\ r_{51} & r_{52} & r_{53} \\ r_{61} & r_{62} & r_{63} \end{bmatrix} \begin{bmatrix} E_x^e \\ E_y^e \\ E_z^e \end{bmatrix} \tag{39}$$

In negative uniaxial crystals with trigonal structure, such as LiNbO3, the electro-optic tensor reduces to

$$r_{ij} = \begin{bmatrix} 0 & -r_{22} & r_{13} \\ 0 & r_{22} & r_{13} \\ 0 & 0 & r_{33} \\ 0 & r_{51} & 0 \\ r_{51} & 0 & 0 \\ -r_{22} & 0 & 0 \end{bmatrix}. \tag{40}$$

For LiNbO3, the coefficients for the electro-optic tensor are given by [31]

$$r_{ij} = \begin{bmatrix} 0 & -3.4 & 8.6 \\ 0 & 3.4 & 8.6 \\ 0 & 0 & 30.8 \\ 0 & 28 & 0 \\ 28 & 0 & 0 \\ -3.4 & 0 & 0 \end{bmatrix} {}^{\mathrm{pm}}\!/_{\mathrm{V}}\,. \tag{41}$$

The refractive indices of the ordinary ray, n_y, and the extraordinary ray, n_z, with an electric field applied along the optical axis are given by

$$\begin{cases} \mathrm{n}_y = \mathrm{n}_o - \Delta\mathrm{n}_o, & \Delta\mathrm{n}_o = \frac{1}{2} r_{13}\mathrm{n}_o^3 E_z^e \\ \mathrm{n}_z = \mathrm{n}_e - \Delta\mathrm{n}_e, & \Delta\mathrm{n}_e = \frac{1}{2} r_{33}\mathrm{n}_e^3 E_z^e \end{cases}. \tag{42}$$

The change in the extraordinary refractive index is critical for x-cut, y-propagating APE waveguides fabricated on $LiNbO_3$. This APE configuration supports the propagation of the TE mode, which sees n_e. As is apparent in (42), it will take advantage of the r_{33} electro-optic coefficient, which is the largest for $LiNbO_3$.

Because the TE mode on x-cut y-propagating $LiNbO_3$ is being used, the change in refractive index for a conventional single length channel electrode is, thus, given by

$$|\Delta\mathrm{n}_e| = \frac{1}{2}\mathrm{n}_e^3 r_{33} E_z \tag{43}$$

where $n_e = 2.1378$ is the extraordinary refractive index, $r_{33} = 30.8$ pm/V is the electro-optic coefficient, and E_z is the electric field with approximate magnitude of $|E| \approx V/G$ where V is the applied voltage and G is the electrode gap. Because the electric field and optical field do not uniformly overlap, the effective index change within a cross section of the optical mode can be expressed as

$$|\Delta n_e(V)| = \frac{1}{2} n_e^3 r_{33} \frac{V}{G} \Gamma \tag{44}$$

where Γ is the overlap factor between the electric and optical fields and is given by the overlap integral

$$\Gamma = \frac{G}{V}\iint E|E'|^2 dA \qquad (45)$$

where E is the applied electric field and E' is the normalized optical field distribution. Then, the total phase shift over the interaction length L is given by

$$\Delta\beta L = \frac{\pi}{2} n_e^3 r_{33} \frac{V}{G} \Gamma \frac{\mathrm{L}}{\lambda} \qquad (46)$$

where λ is the free-space wavelength. Therefore, the voltage required for a particular phase shift is

$$V = (\Delta\phi) \frac{G\lambda}{\pi L \Gamma n_e^3 r_{33}} \qquad (47)$$

where $\Delta\phi = \Delta\beta L/2$ is the desired phase shift. In this channel electrode array, every electrode is the same length and each one is controlled individually. This allows for different voltages to be applied across each electrode that causes a phase difference between each element in the array, allowing for the array factor to be steered [34]. Therefore, with a phase shift of $\Delta\phi$, the angle that the beam is steered, θ, is given by $sin(\theta) = (\Delta\phi/2\pi)(\lambda/d)$. The electrode configuration and phase difference are pictured in Fig. 8.

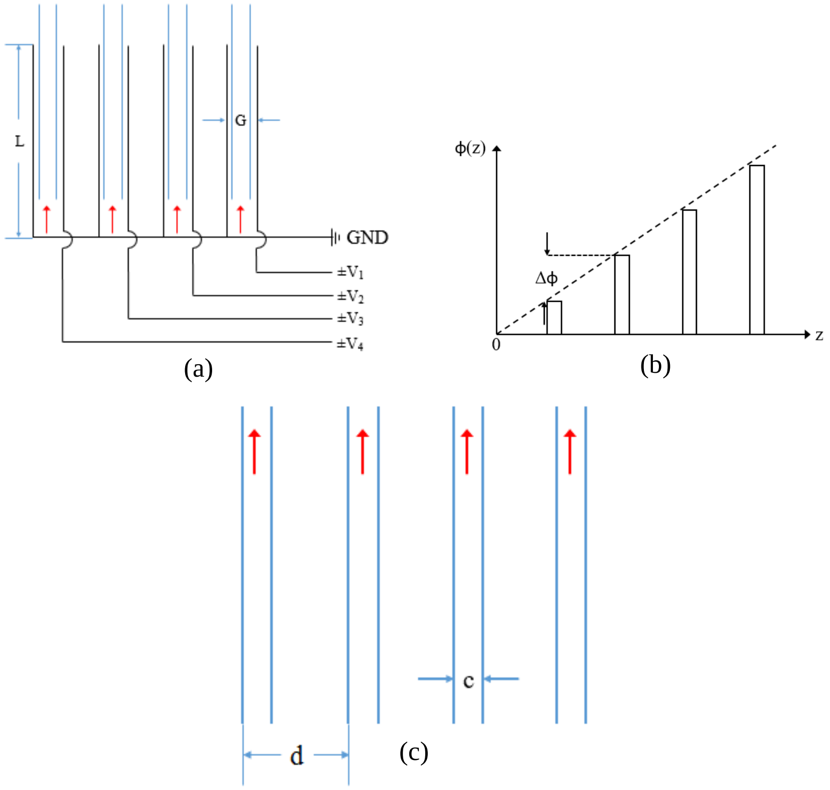

Fig. 8 a) Channel Electrode Array, b) phase distribution of channel array, and c) output of As2S3 waveguide array [20].

II.F.2. Coplanar Strip Electrodes

A coplanar strip electrode consists of two parallel metallic strips separated by a gap. The gap between the electrodes creates an electric field with two directions, horizontal and vertical. This is shown by the electric field lines in Fig. 9. Because of the properties of $LiNbO_3$ discussed earlier, the crystal cut is important in determining which electro-optic coefficient is used for specific polarizations during tuning. This also affects the placement of the electrodes.

The two optical mode polarizations that propagate along the waveguide are the TE and TM modes. The TM is oriented in the vertical direction and the TE mode is oriented in the horizontal direction. As is apparent from (39), in order to take advantage of the r_{33} electro-optic coefficient, the optical mode polarization and the electric field must be oriented in the z-direction. Therefore, if tuning of the TM mode is desired, the device must be fabricated on z-cut y-propagating $LiNbO_3$. This requires a vertical electric field, which means the electrode must be fabricated on top of the waveguide. This configuration will lead to extra losses and will not allow for a true vertical field. A true vertical electric field can be obtained by placing one electrode on the top and one on the bottom of the substrate, but is not feasible due to the thickness of the substrate. Tuning of the TE mode by using the r_{33} electro-optic coefficient is much easier in that it requires a horizontal electric field. Therefore, in x-cut y-propagating $LiNbO_3$, the electrodes can be placed one on each side of the waveguide. This is ideal in that APE waveguides fabricated on x-cut y-propagating $LiNbO_3$ only allow for the TE mode to propagate.

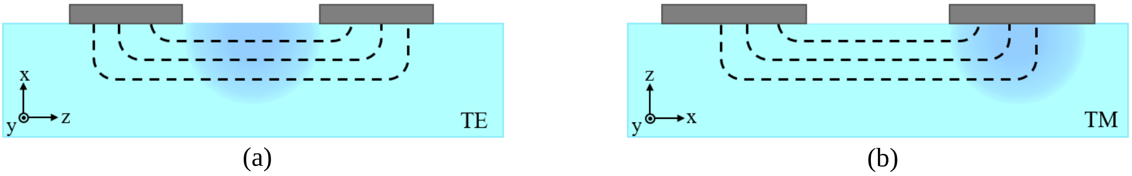

(a) (b)

Fig. 9 Electrode orientation and $LiNbO_3$ crystal cut for a) TE and b) TM polarization for tuning with the r_{33} electro-optic coefficient.

A great amount of work has gone into the design and optimization of CPS electrodes in order to get the best tuning with the least amount of power. In order for low V_π voltages to be obtained, velocity and impedance matching, low electrode losses, electrode lengths, and the electro-optic mode overlap integral must be optimized [35]. One way to begin optimizing these parameters is by creating asymmetric coplanar strip electrodes, where the ground plane is much wider than the signal plane [36]. 50 Ω impedance matching can be obtained with a gap to width ration of 0.65 for CPS electrodes [36] and 1.7 for ACPS electrodes [37]. However, this is an idealized number in that the buffer layer and electrode thicknesses, as well as the electro-optic mode overlap, were not considered.

As the switching frequency increases, these devices must operate at high electrical efficiency because of limitations in available drive power and power dissipation [34]. The drive power and bandwidth are dependent on the microwave properties of the electrode. Therefore, the impedance, microwave attenuation, and velocity mismatch as a function of electrode gap, width, thickness, and buffer layer must be considered. The buffer layer is used in order to reduce optical losses due to the metal electrodes. The introduction of this buffer layer also decreases the total capacitance brought forth by the electrodes because the dielectric constant of the buffer layer material (SiO_2) is much smaller than that of $LiNbO_3$. An increase in the electrode and buffer layer thicknesses results in a reduction in velocity mismatch. The characteristic impedance of a transmission line is given as [34]

$$Z = \frac{1}{v_m C} \tag{48}$$

where v_m is the phase velocity and is given by

$$v_m = \frac{1}{\sqrt{LC}}. \tag{49}$$

The characteristic impedance of an air field line is given by

$$Z = \frac{1}{cC_0} \tag{50}$$

where c is the speed of light in free space and C_0 is the capacitance per unit length of this air-filled line. The speed of light in free space can be represented by

$$c = \frac{1}{\sqrt{LC_0}}. \tag{51}$$

When (49) is divided by (51) and squared, the result is

$$\left(\frac{c}{v_m}\right)^2 = \frac{C}{C_0} \equiv \varepsilon_{eff} \tag{52}$$

where $\boldsymbol{\varepsilon_{eff}}$ is the effective relative permittivity. Therefore, the effective microwave refractive index is

$$\mathrm{n}_{eff}^{m} = \sqrt{\varepsilon_{eff}} \tag{53}$$

The capacitances C and C_0 for ACPS electrodes with finite electrode thickness and having a buffer layer are

$$C = \varepsilon_0(1 + \varepsilon_r)\frac{K(x')}{K(x)} - C_b + C_t \tag{54}$$

$$C_0 = 2\varepsilon_0\frac{K(x')}{K(x)} + C_t \tag{55}$$

where $\boldsymbol{\varepsilon_r}$ is the dielectric constant of LiNbO$_3$, K is the complete elliptic integral of the first kind, $x = 1/\sqrt{1 + W/G}$, and $x' = \sqrt{1 - x^2}$ (W is the width of the signal electrode). C_b and C_t are the increased capacitance due to the buffer layer and electrode thicknesses, respectively, and are given by

$$C_b = b_1 \varepsilon_b \varepsilon_0 ln(1 + b_2 x) ln\left(b_3 + b_3 \frac{t_b}{G}\right) \tag{56}$$

$$C_t = \pi \varepsilon_0 \frac{a_1 - a_2 ln(W/G) + a_3 ln(a_4 + t/G)}{ln(4G/t) + \frac{1}{8}(t/G)^2} \tag{57}$$

where ε_b is the dielectric constant of the buffer layer, t_b is the thickness of the buffer layer, and t is the thickness of the electrode. The coefficients b_1, b_2, b_3, a_1, a_2, a_3, and a_4 are found from the results obtained from Green's function method [34]. Multiple optical phased arrays have been fabricated with various electrode parameters. Table III displays the various parameters along with the calculated π-voltage at a wavelength of 1.55 µm for each case.

Table III
Electrode parameters and resulting V_π [21]

Gap (µm)	Length (µm)	V_π (V)
9	6000	9.1
	7000	7.8
	8000	6.8
10	6000	10.1
	7000	8.7
	8000	7.6
	9000	6.7

II.G. Coupled Mode Theory

In order to create a device with small output array pitch, the optical mode must be coupled from the diffused waveguides into a higher index material, but coupling between guided modes in parallel waveguides must be prevented. Considering the simplest case of two identical waveguides placed in close proximity to one another with a uniform step-index change, as in Fig. 10, one can find the coupled mode equations for waveguides A and B.

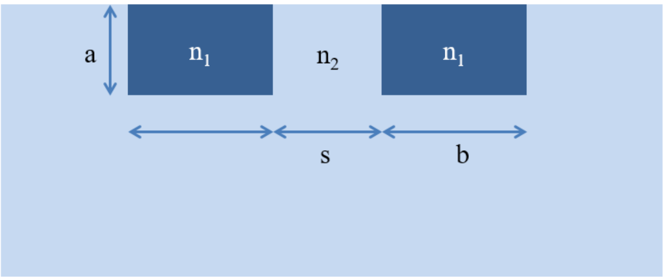

Fig. 10 Two identical parallel waveguides positioned as a directional coupler.

The equations governing the coupling between the waveguides are [26]

$$\left.\begin{aligned}\frac{dA(z)}{dz} &= -j\kappa_{ab}B(z)e^{j(\beta_a-\beta_b)z}\\ \frac{dB(z)}{dz} &= -j\kappa_{ba}A(z)e^{j(\beta_b-\beta_a)z}\end{aligned}\right\} \tag{58}$$

where $\kappa_{ab} = \kappa_{ba}$ is the coupling coefficient. For slab waveguide coupling, κ_{ab} is given by

$$\kappa_{ab} = \frac{2h^2q}{\beta\left(t+\frac{2}{q}\right)(h^2+q^2)}e^{-qs} \tag{59}$$

where q and h are defined in (27) and (28), respectively. As can be seen from (59), the coupling depends significantly on the spacing between the waveguides.

While this coupling works great for identical waveguides in close proximity, the use of tapered couplers is needed for waveguides with different cross-sectional dimensions [38] or different refractive indices. To get efficient coupling, the waveguides must be phase matched ($\beta_a = \beta_b$). This is achieved by introducing the second waveguide with a small taper tip and a gradual slope. For our devices, the mode is coupled into an As_2S_3 rib waveguide via a tapered section of As_2S_3.

Recall that κ_{ab} depends on the spacing between the waveguides. Because of this, we could put the coupling taper for the rib waveguide directly on top of the diffused waveguide. However, with Ti:$LiNbO_3$ waveguides, a surface bump is created, which does not allow this to be done without significant losses. APE waveguides have little effect on the surface topology of the substrate; therefore, the taper tips of the As_2S_3 rib waveguide are placed directly on top of them. In theory, this should allow for much higher coupling and lower loss from the diffused waveguide to the rib waveguide. The vertical integration of As_2S_3 waveguides is used because of the higher index, which allows for a much smaller bending radius than pure Ti:$LiNbO_3$ or APE waveguides. This smaller bending radius leads to the ability to fabricate much smaller devices [39].

X-cut y-propagating $LiNbO_3$ has an extraordinary refractive index of 2.1378, and the annealed proton exchange process creates an index change of approximately 0.019. This slight index difference does not allow for tight bends or closely spaced waveguide structures. Fig. 11 shows that even with a waveguide pitch of 24 µm, mode coupling still occurs between adjacent single-mode diffused waveguides that have a $1/e^2$ horizontal mode width of 12.6 µm.

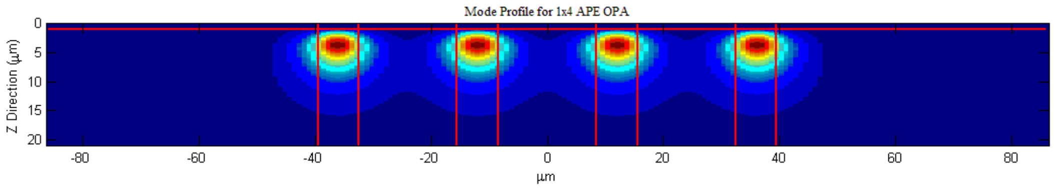

Fig. 11 Mode profile for a 1x4 APE OPA [20].

Therefore, a high index As$_2$S$_3$ rib waveguide is vertically integrated on top of the APE waveguides. This allows for the optical mode to couple from the APE waveguide into the As$_2$S$_3$ waveguide, which gives the ability to closely space the output array for wider steering angles. A large effective index contrast between the APE and As$_2$S$_3$ waveguides prevents the optical mode from coupling into the As$_2$S$_3$ waveguide if it is at its single mode propagation width. Therefore, a mode size converter is created by means of a taper region. The taper helps reduce the effective index mismatch between the APE and As$_2$S$_3$ waveguides and allows the mode to couple into the As$_2$S$_3$[16]. The As$_2$S$_3$ taper structure is pictured in Fig. 12.

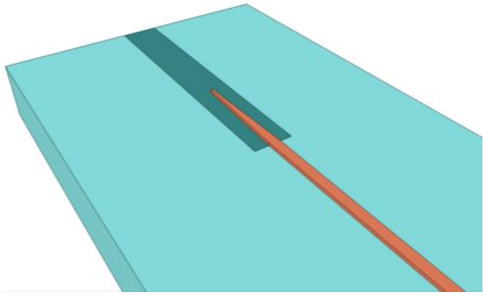

Fig. 12 As$_2$S$_3$ taper vertically integrated on APE waveguide.

Fig. 13 shows a FIMMPROP simulation of the optical mode progression at different positions along the taper length. As can be seen, a higher percentage of the optical mode goes into the As_2S_3 the further along the taper it is. A taper length of 200µm and a single simulated optical mode allows for 98.8% of the light to be coupled into the As_2S_3 waveguide that tapers from 0.6µm-1.6µm with a resulting As_2S_3 $1/e^2$ horizontal mode size of 1.3 µm.

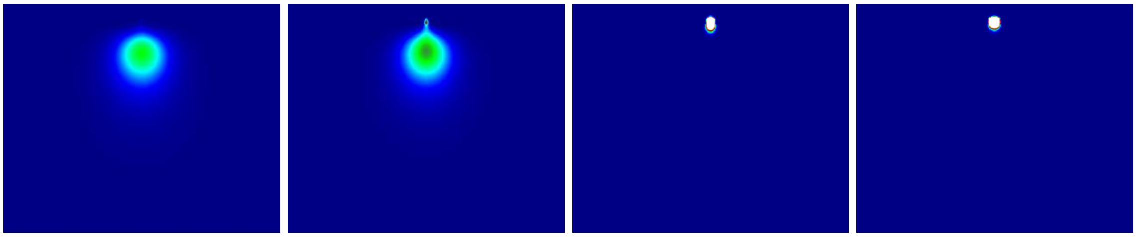

Fig. 13 Optical mode coupling into As_2S_3 waveguide as it travels the length of the taper [20].

However, when more modes are added to increase the accuracy of the simulation, the coupled power highly decreases, as was evident from measurements. Table IV, shows that only 12.4% of the power in the fundamental mode is coupled into the As_2S_3 with a taper length of 200 µm. Also, a taper length of 9.5 mm is required to couple only 72.9% of the power. Fig. 14 shows a plot with the output power of taper lengths up to 20 mm.

Table IV
Taper Simulation Data for Multiple Modes with 0.6 µm - 1.6 µm taper Length

Taper Length (µm)	200	500	1000	5000	9500
Power in Fundamental Mode	12.4%	14.9%	19.6%	56.0%	72.9%

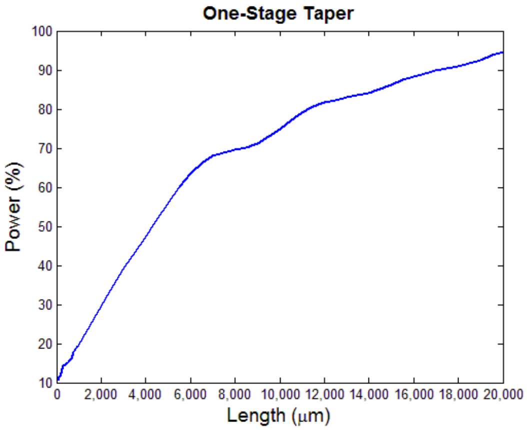

Fig. 14 Plot of taper length of a one-stage taper and the respective coupled power.

This result led to a redesign of the As_2S_3 tapers. A two-stage taper was designed, which helped to drastically reduce the required taper length for the desired output power. The first stage of the taper consisted of a section that tapered from 0.6 µm – 1.0 µm and a second section that tapered from 1.0 µm – 1.6 µm. With a first section taper length of 2.5 mm and a second section taper length of 100 µm, the power coupled in the fundamental mode is 72.2%. This overall length is a 72.6% reduction in the length required to couple this amount of power with the one-stage taper above. Fig. 15 shows a plot with the output power with first stage taper lengths up to 7 mm and all having a second stage length of 100 µm.

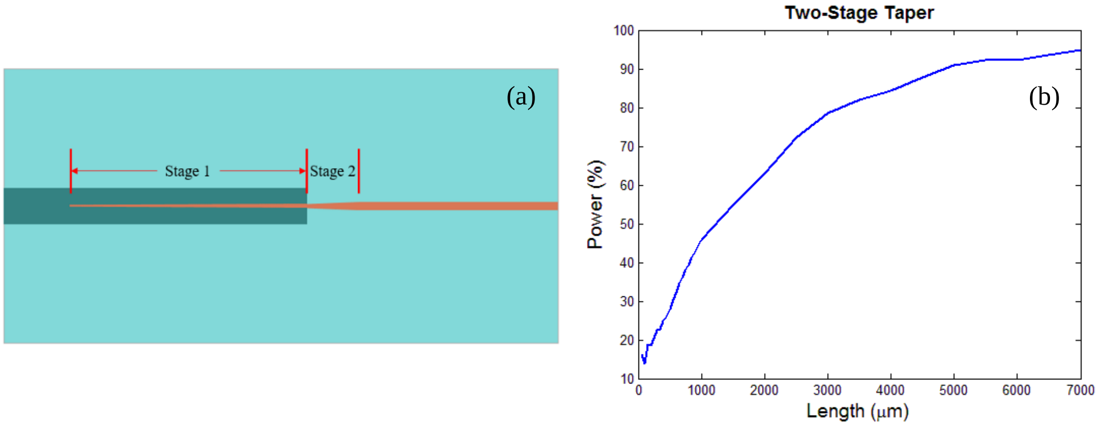

Fig. 15 a) Drawing of two-stage taper and b) plot of taper length of a two-stage taper and the respective coupled power.

This two-stage taper design was further improved by having the first stage taper from 0.5 µm – 0.8µm and the second stage taper from 0.8 µm – 1.6 µm, with the second stage having a taper length of 160 µm. To compare with the results from above, with a first-stage taper length of 2.5 mm and second-stage taper length of 160 µm, the power coupled in the fundamental mode is 78.7%. Fig. 16 shows a plot of the output power with first stage taper lengths up to 7 mm and all having a second stage length of 160 µm.

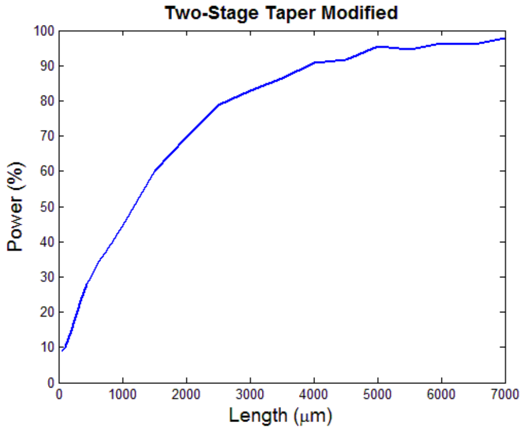

Fig. 16 Plot of taper length of the modified two-stage taper and the respective coupled power.

Because of manual alignment and other factors, fabrication tolerances must also be taken into account when simulating the As_2S_3 tapers. Fig. 17 shows an example of when the As_2S_3 waveguide is vertically misaligned from the APE waveguide. Both misalignment and taper length can lead to unwanted excess losses, as well as power coupling into higher order modes.

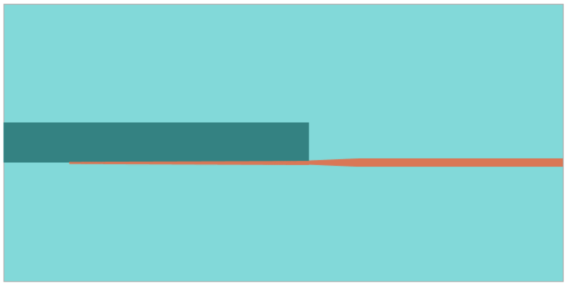

Fig. 17 As2S3 vertical misalignment.

Fig. 18 shows the output power of the fundamental TE mode of the As_2S_3 waveguide with a vertical misalignment offset from 0.5 μm to 3.5 μm. This is displayed for first stage taper lengths ranging from 2.5 mm to 4.5 mm. As can be seen, as the alignment gets worse, so does the output power. The misalignment tolerance is estimated to be within 2 μm. Therefore, taper lengths greater than 2.5 mm within this error have adequate power output. It is also interesting to note that the taper lengths displayed have better performance with a 0.5 μm offset than a centered waveguide with no offset.

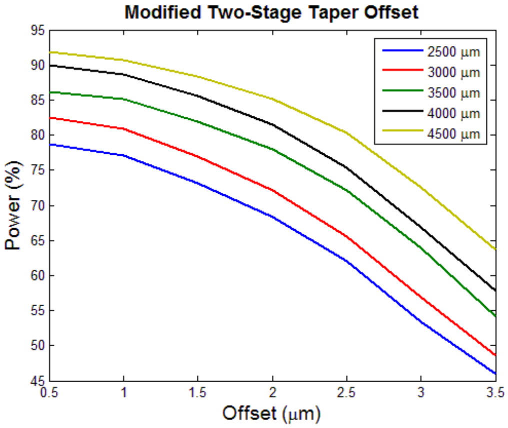

Fig. 18 Output power loss due to As_2S_3 misalignment.

II.H. Beam Steering Theory

Ideally, the farfield pattern of the optical phased array can be represented by Fraunhofer diffraction [40]:

$$U(\mathrm{X}) = C\sum_{j=1}^{N}\int_{(j-1)p}^{jp} T_j(z)exp\left\{-i2\mathrm{X}\left[(j-1)\left(p-\frac{\Delta\phi}{2\mathrm{X}}+z\right)\right]\right\}dz \qquad (60)$$

where the deflection parameter $X = \left(\frac{\pi}{\lambda_g}\right) sin\nu$, ν is the diffraction angle, p is the period, Δφ is the voltage-induced phase difference between elements, and T_j(z) is the transmission function of the jth element. So, the far-field intensity pattern is

$$I(\mathrm{X}) = |U(\mathrm{X})|^2 = (AF)(EF) \tag{61}$$

where AF is the array factor and EF is the element factor. Different electrode configurations can be utilized to steer the far-field intensity pattern of the optical phased array: the channel electrode structure, the prism electrode structure, and the phase-staggered prism electrode structure.

II.H.1. Channel Electrode

In the channel electrode structure, AF is represented by

$$AF = \frac{sin^2\left\{N\left(\frac{\pi d}{\lambda}x - \frac{\Delta\phi}{2}\right)\right\}}{sin^2\left\{\left(\frac{\pi d}{\lambda}x - \frac{\Delta\phi}{2}\right)\right\}} \tag{62}$$

and EF is represented by

$$EF = \left|F\left(T_j\right)\right|^2 \tag{63}$$

where $F(T_j)$ is the Fourier transform of the transmission function of the jth element. This is expressed as

$$F\left(T_j\right) = \int_{(j-1)p}^{jp} T_j(z) exp(-i2Xz) dz\,. \tag{64}$$

The element factor can be expressed in terms of the channel width, c, as

$$EF = \left(\frac{c}{d}\right)^2 \frac{sin^2\left(\frac{c\mathrm{x}}{\lambda}\right)}{\left(\frac{c\mathrm{x}}{\lambda}\right)^2}. \tag{65}$$

Therefore, the far-field intensity distribution can be expressed as

$$I(\mathrm{X}) = \frac{sin^2\left\{N\left(\frac{\pi d}{\lambda}x - \frac{\Delta\phi}{2}\right)\right\}}{sin^2\left\{\left(\frac{\pi d}{\lambda}x - \frac{\Delta\phi}{2}\right)\right\}}\left(\frac{c}{d}\right)^2 \frac{sin^2\left(\frac{c\mathrm{x}}{\lambda}\right)}{\left(\frac{c\mathrm{x}}{\lambda}\right)^2}. \tag{66}$$

As can be seen, the element factor is independent of voltage, allowing only the array factor to be steered. This permits continuous steering, but limits it to the width of the element factor. More precisely, it is limited to ± half the distance of the undeflected position of the first-order lobe [41].

II.H.2. Prism Electrode

The prism electrode array consists of electrodes that are laid diagonally across the output waveguides, Fig. 19 a). This structure results in a saw tooth phase distribution as pictured in Fig. 19 b).

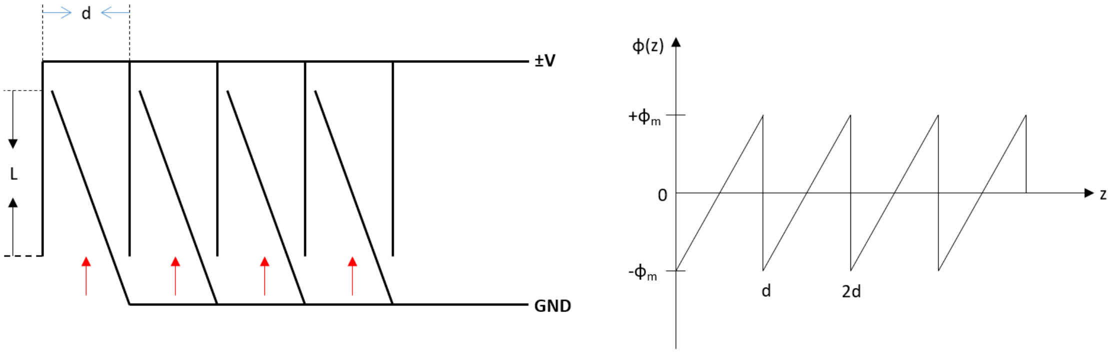

Fig. 19 a) Prism electrode array and b) phase distribution of prism array.

The configuration of this structure allows element factor to be manipulated by an applied voltage, but because there is no phase difference between the elements in the array, the array factor cannot be steered. The array factor can then be expressed in terms of the number of output waveguides and their pitch as

$$AF = \frac{sin^2\{N(dX)\}}{sin^2\{(dX)\}}. \tag{67}$$

The element factor is now dependent upon the applied voltage and can be expressed as

$$EF = d^2 \frac{sin^2(dX - \phi_m)}{(dX - \phi_m)^2}. \tag{68}$$

This leads the far-field intensity distribution to be

$$I(X) = \frac{sin^2\{N(dX)\}}{sin^2\{(dX)\}} \; d^2 \frac{sin^2(dX - \phi_m)}{(dX - \phi_m)^2}. \tag{69}$$

Because the array factor is no longer dependent upon the applied voltage, only the element factor can be steered. This allows for non-continuous or discrete beam steering. Spots can only be resolved when the max of the element factor is steered to an angle of a max of the array factor.

II.H.3. Phase Staggered Prism Electrode

The phase-staggered prism electrode array is the same as the prism array, but it allows a difference to be placed between the elements of the array. This, in turn, lets both the array factor and the element factor to be steered. Fig. 20 shows the array configuration along with the output phase distribution.

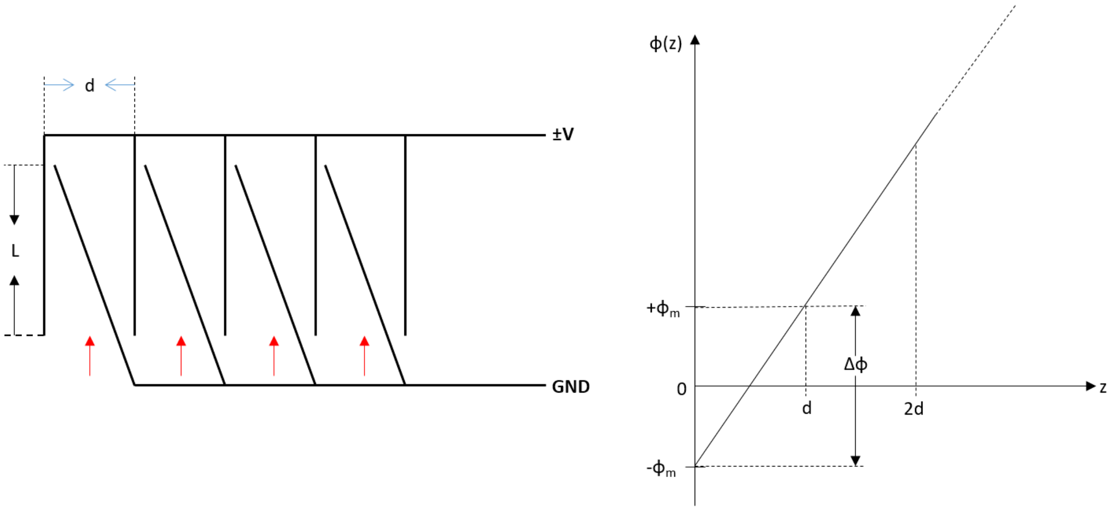

Fig. 20 a) Phase-staggered prism electrode array. b) Phase distribution of the phase-staggered prism array.

The array factor is the same as the array factor of the channel electrode array, and the element factor is the same as the element factor of the prism electrode array. Therefore, the far-field intensity distribution can be expressed as

$$I(X) = \frac{sin^2\left\{N\left(\frac{\pi d}{\lambda}x - \frac{\Delta\phi}{2}\right)\right\}}{sin^2\left\{\left(\frac{\pi d}{\lambda}x - \frac{\Delta\phi}{2}\right)\right\}}\ d^2\,\frac{sin^2(dX-\phi_m)}{(dX-\phi_m)^2}. \tag{70}$$

This allows for wide-angle continuous beam steering. The prism electrode and phase-staggered prism electrode structures become impractical as the width of the waveguides decreases. Therefore, in this work the channel electrode structure is utilized.

II.H.4. Resolvable Spots

The number of resolvable spots *m* is given by the angular deflection divided by the spacing between beam positions [40]

$$m = \frac{N\Delta\phi}{\pi}. \tag{71}$$

The phase shift in any single channel with electrode pair length *L* can be written as

$$\Delta\phi = \frac{n_e^3 r_{33} V L}{\lambda G}. \tag{72}$$

Now, the number of resolvable spots can be written as

$$m = \frac{2 n_e^3 r_{33} V L}{\pi \lambda G}. \tag{73}$$

Where *L* is the length of the electrode pairs.

II.H.5. Optical Phased Array Simulations

Running simulations on this ideally quantified system results in the data shown in Fig. 21.This has a FWHM output spot size of ($\psi = (\lambda/Nd)(180°/\pi)$) 4.27° and a maximum 2π-steering angle of ($\theta_{max} = (\lambda/d)(180°/\pi)$) of ± 17°. The V-π voltage of an electrode with a length of 7000 μm and gap of 10 μm was found to be 8.66 V at a wavelength of 1.55 μm. The second image in Fig. 21 shows the far-field intensity pattern of diffused waveguides in $LiNbO_3$ with a pitch of 24 μm and waveguide width of 7 μm. The vertical green lines depict the non-redundant scan zone or, in other words, the maximum allowable steering angle. As is evident, this increased pitch greatly reduces the steering angle and increases the strength of the side lobes.

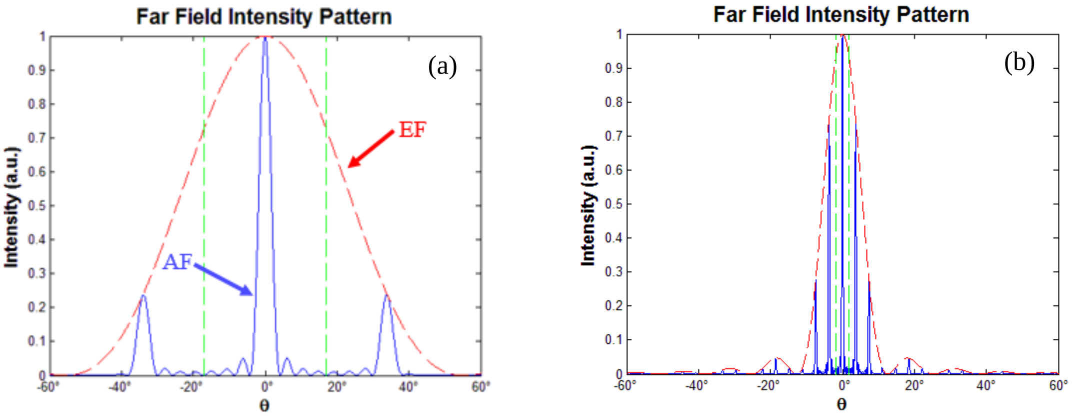

Fig. 21 Far field intensity pattern of 8 output a) hybrid array and b) diffused array, respectively.

When a voltage is applied to the electrodes of the array elements to create a phase difference between adjacent elements, the array factor is shifted within the element factor. Fig. 22 displays the array factor being shifted inside the element factor. In the left figure, a phase difference of 0.5π is applied to adjacent array elements. In the right figure, a phase difference of 0.9π is applied to adjacent array elements. As is evident, if a phase difference of π were to be applied to adjacent elements in the array, the main lobe and first order side lobe would be shifted to the vertical green dashed lines and would have equal magnitudes. Therefore, the scan zone is limited to slightly smaller than a π phase shift.

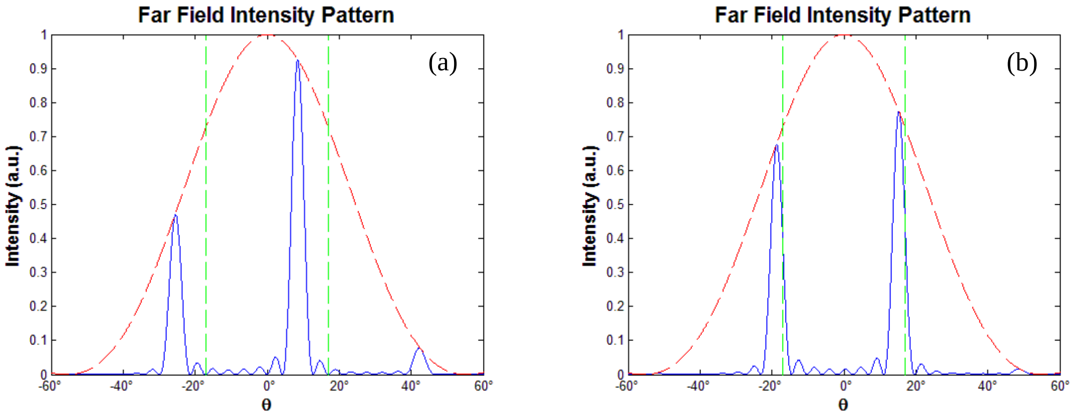

Fig. 22 Far field intensity pattern of 8 output hybrid array shifted by a) 0.5π and b) 0.9π.

CHAPTER III

DEVICE FABRICATION[*]

This chapter focuses on the fabrication of the hybrid $LiNbO_3$ – As_2S_3 optical phased array, as well as the APE:$LiNbO_3$ OPA. The only differences between the two processes is that for the APE:$LiNbO_3$ OPA, the APE waveguides are fabricated fully to the edge of the sample and the fabrication of the As_2S_3 waveguides is skipped. There are three main steps involved in creating the $LiNbO_3$ – As_2S_3 OPA, which include the fabrication of the APE waveguides, the fabrication of the As_2S_3 waveguides, and the fabrication of the Al electrodes. Each step in the process will be examined and explained thoroughly.

III.A. Annealed Proton Exchange Waveguide Fabrication

In order for light to be guided, there must be an area of higher refractive index surrounded by one of lower refractive index. To be able to produce this index contrast, a method known as annealed proton exchange is used. A hydrogen source, in this case benzoic acid, is used to drive hydrogen ions into the $LiNbO_3$ substrate to replace lithium ions, which creates a region of higher refractive index that enables input light to be guided in a controlled manner. APE waveguides fabricated in this x-cut substrate only cause an increase in the extraordinary refractive index, which means only the TE mode is allowed

---

[*] Part of the data reported in this chapter is reprinted from D. D. Macik and C. K. Madsen, “Fabrication of $LiNbO_3$-As_2S_3 waveguides for beam steering applications,” *Proc. SPIE*, vol. 9970, pp. 99700H-1 – 99700H-10, 2016.

to propagate. The first part of the fabrication process involves creating these APE waveguides.

III.A.1. Sample Preparation

This device is fabricated on an x-cut y-propagating $LiNbO_3$ substrate from Crystal Technology, LLC that is 1mm thick. The 3 inch $LiNbO_3$ wafer is diced, using a MicroAutomation 1100 Wafer Dicing Saw, into four 3 cm x 2 cm samples. The dicing diagram used in this step is shown in Fig. 23. After dicing, great care is taken in cleaning the samples to remove residual particles and to prevent further contamination in the latter phases of fabrication. First, soapy water is used to clean the sample. Then, solvents that include acetone, methanol, and isopropanol are used to further clean the sample and prevent spotting. The sample is dried with an inert gas such as nitrogen.

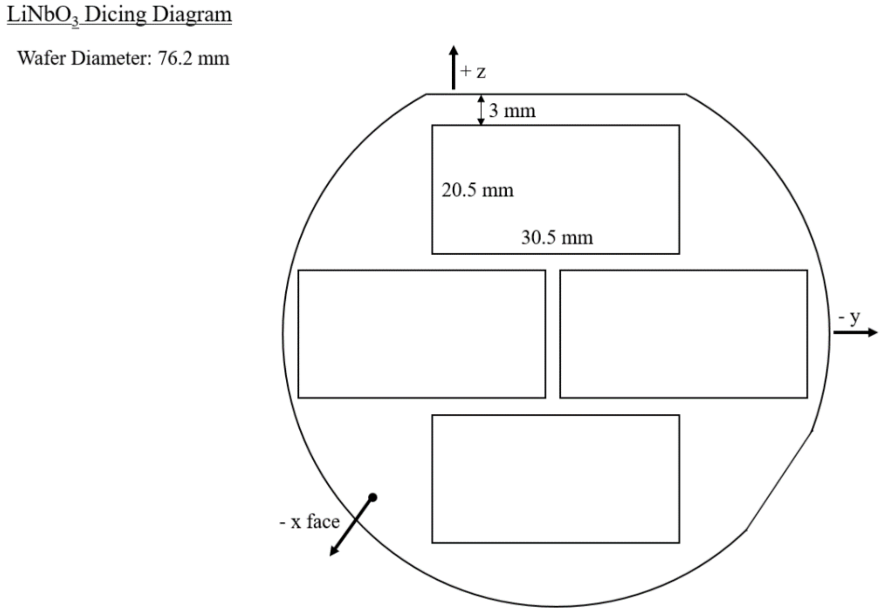

Fig. 23 Dicing diagram used for dicing a 3 in $LiNbO_3$ wafer for further processing

III.A.2. Deposition

An AJA International DC/RF Magnetron Sputtering system is used to deposit high quality thin films with great surface uniformity. The AJA consists of a main chamber that houses the sputtering guns and is kept in a high-vacuum state until targets need to be changed or the chamber needs to be cleaned. To prevent from having to vent the main chamber every time samples are loaded, there is also a load-lock. The load-lock is much smaller than the main chamber and can, therefore, be evacuated in a more timely manner.

Fig. 24 AJA International, Inc. RF/DC Magnetron Sputtering System.

This is also advantageous because some of the targets are sensitive to air and remain under high-vacuum for most of their lifetime. As seen in Fig. 25, the load-lock consists of a platform to place a sample holder. The platform is attached to a loading arm that is used to push the samples into the main chamber. The load-lock rapidly pumps down to 10^{-5} Torr.

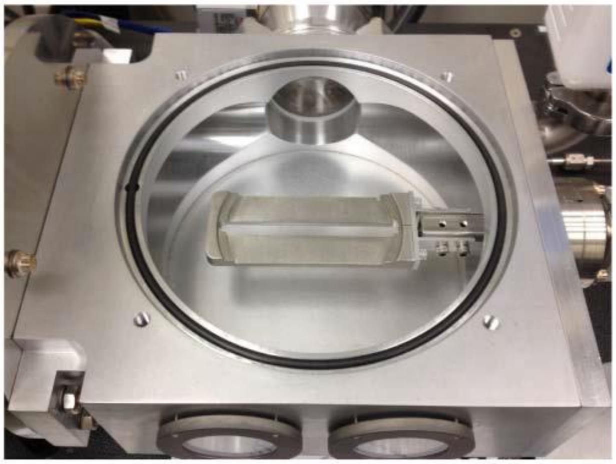

Fig. 25 Load-lock with sample holder platform.

The targets and sputtering gun are located inside the main chamber. The gun consists of a ground, cathode, inner magnet, and outer ring of magnets, Fig. 26. There is a gap between the ground and the cathode that must be clear of debris. If some conductive particles get wedged in this gap, a short will be caused that can damage the target and the gun itself. A water chilling system is used to keep the guns and targets at 15°C throughout the deposition process.

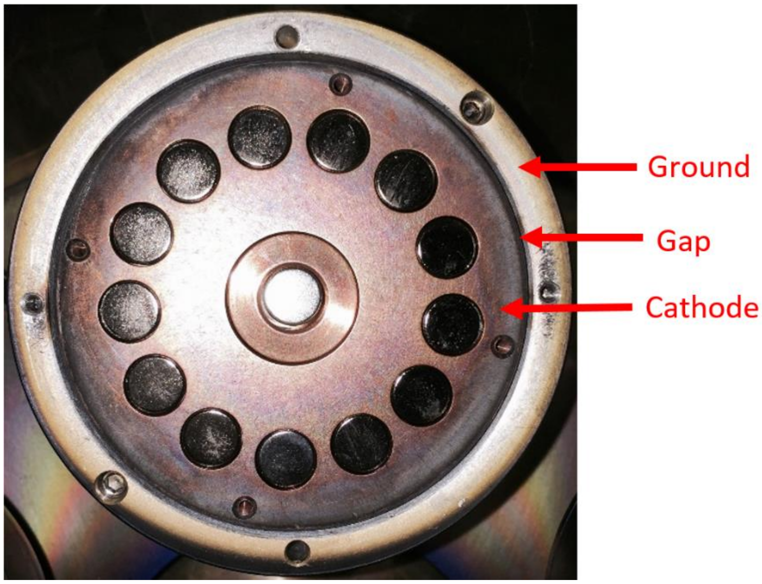

Fig. 26 AJA sputtering gun assembly.

For the APE process, a silicon dioxide film is deposited and will be used as a masking layer for the substrate in the exchange step, which helps prevent the substrate from being exchanged in unwanted regions. In particular, RF magnetron sputtering is used to deposit this thin film of SiO_2. Argon and Oxygen are flowed at 40 sccm and 1.5 sccm, respectively. The sputtering system is operated at 3 mT with an RF power of 200 W. An approximately 150 nm thick layer of SiO_2 is deposited onto the surface of the $LiNbO_3$ substrate.

III.A.3. Photolithography

Photolithography is used to create openings with 7µm widths in the SiO_2 masking layer where the APE waveguides will be formed. This process simply transfers an image from a mask by exposing a light sensitive substance to UV light. The mask layout is designed in software such as OptiBPM, L-Edit or KLayout, and the pattern is transferred to a quartz plate where it is formed with chrome. Because openings are wanted and positive photolithography is employed, an image reversed or negative mask is designed and pictured in Fig. 27.

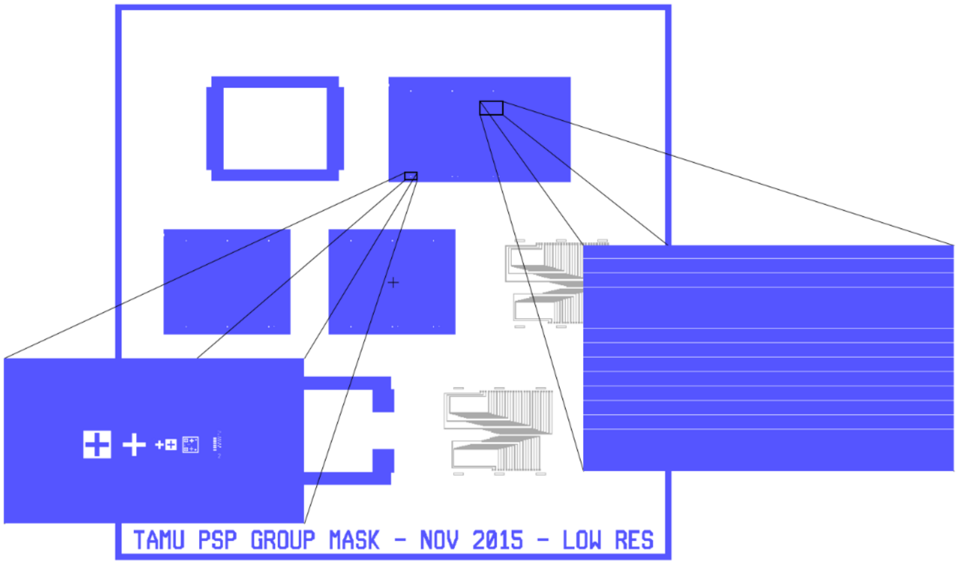

Fig. 27 Image reversed photolithography mask for APE waveguides. Top projection – straight patterns for APE waveguides. Bottom projection – alignment marks for Tungsten alignment.

After the deposition of the SiO_2 masking layer, a layer of approximately 1.4 µm thick AZ5214e photoresist is spin coated onto the sample at 4000 RPM for 40 seconds. Once this uniform layer of photoresist is formed, a soft bake step takes place at 125°C for 1 minute and 15 seconds. A Karl Suss MA6 contact mask aligner is used to carry out the photolithography. This machine uses i-line lithography at 365 nm wavelength UV radiation. A dosage of 85 mJ/cm^2 is used which, along with the intensity of the UV lamp, determines the exposure time. The mask is loaded onto the machine and aligned to the sample, and then, exposure takes place. After exposure, the sample is developed with AZ726 developer for approximately 30 seconds. To complete the lithography process, the sample is hard baked in a dehydration oven for 8 minutes. Some of the waveguides extend across the entire sample, while others only extend partially, Fig. 28. The waveguides that extend across the entire sample are used in an intermediate step to measure the loss characteristics of the APE waveguides. Those that extend only partially over the sample are used for the vertical coupling to the As_2S_3 waveguides. Some samples have been fabricated with all waveguides extending across the entire sample. These will be used for coupling to a Si_3N_4 waveguide array. It is also important to note that the APE waveguides have a pitch of 127 µm. This is important in order to provide easy coupling to a standard fiber array and to the standardized inputs of the Si_3N_4 waveguide pitch.

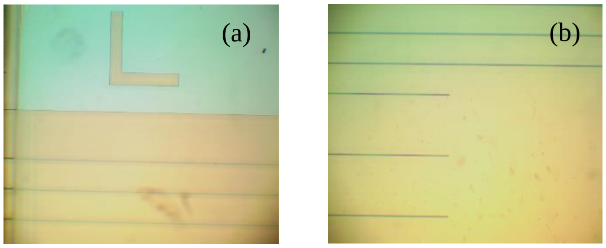

Fig. 28 Photolithographically patterned sample after development showing waveguides that a) extend fully and b) partially across the sample.

III.A.4. Etching

Now that the pattern is transferred to the sample, the areas where the SiO_2 masking layer is exposed (areas where waveguides will be formed) must be etched in order to bare the $LiNbO_3$ surface for the exchange. Dry etching is used in this case because of the anisotropic characteristics and the higher selectivity than wet etching, Fig. 29.

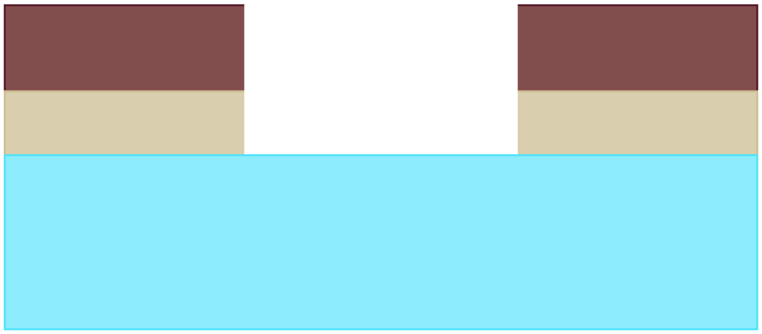

Fig. 29 Anisotropic dry etch. SiO_2 layer etched by RIE after photoresist development.

Reactive ion etching is used to perform the etching in this step with a Plasmalab System 100 from Oxford Plasma Technology. The RIE is operated at a pressure of 10 mT with RF and ICP powers set to 100 W and 200 W, respectively. The temperature if the substrate is maintained at 15°C while 25 sccm of CHF_3 and 5 sccm of Ar are flowed. This mixture of a 5:1 ratio of CHF_3:Ar gases used for this etching process gives an etch rate of approximately 60nm/min. Once this process is complete, the remaining photoresist is stripped with AZ400T photostripper. The middle picture in Fig. 30 shows the sample after RIE with the photoresist still present, and the right photo shows the sample after stripping the photoresist leaving only the SiO_2 masking layer and bare substrate. The "L" shape and the horizontal lines are the areas that have been etched and are the $LiNbO_3$ substrate.

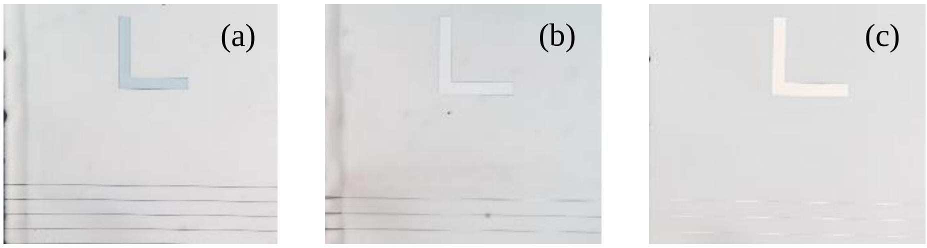

Fig. 30 Sample (a) after photolithography, (b) after reactive ion etching, and (c) after photoresist stripping.

III.A.5. Proton Exchange

Now that the waveguide areas have been opened, the proton exchange process can begin. As mentioned above, benzoic acid is used as the hydrogen source that creates the index difference needed for guiding light. Benzoic acid (C_6H_5COOH) is a colorless powdered solid at room temperature and must be heated to at least 122°C to melt and become a liquid. The desired exchange temperature in this experiment is 200°C, which allows for the exchange to be performed for a shorter length of time [42]. The setup for performing the proton exchange process consists of a thermal probe, an insulating sleeve surrounding the beaker of benzoic acid with a magnetic stirrer, and a hotplate, as pictured in Fig. 31. The proton exchange process is extremely temperature dependent and, therefore, an insulated beaker is used to keep the benzoic acid melt at a constant 200°C. The insulating sleeve is removable and made of a fiber glass mesh with a polytetrafluoroethylene (PTFE) lid. A PTFE sample holder is attached to the lid, which can be easily inserted into the beaker while the sleeve is placed around it.

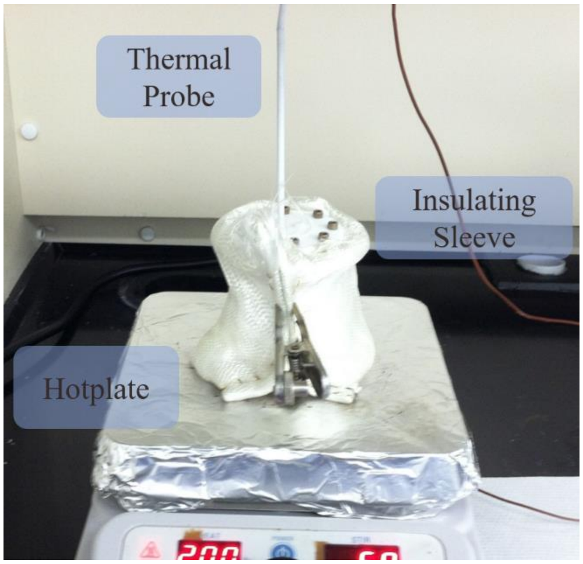

Fig. 31 Proton exchange setup with main parts labeled.

A small 100 mL beaker is filled with 80 mL benzoic acid powder, placed on the hotplate, and allowed to reach 200°C. When the benzoic acid has become a liquid, a magnetic stirrer is placed in the melt to help maintain a consistent temperature throughout the beaker. When the exchange temperature is reached, the sample is placed on the holder and cautiously lowered into the melt. Extreme caution must be taken at this step to prevent thermal shock and the sample breaking. Once thermal equilibrium is reached, the sample is submerged and exchanged for 30 minutes. After this is complete, the sample is removed from the melt with extreme caution, once again, and allowed to cool. Any residual benzoic acid that may have dried on the sample is then removed with isopropanol and by gently cleaning with a q-tip.

III.A.6. Annealing

PE waveguides are unstable and suffer from degradation of the electro-optic coefficients [43]. They are also step index waveguides that will exhibit additional losses with fiber-to-waveguide coupling. To fight against these characteristics and restore the electro-optic properties [44], the samples are annealed in a diffusion furnace to create a diffused profile [45]. This diffused profile more closely resembles that of a typical single mode fiber. The temperature used for the annealing step is 400°C. The sample is placed on a ceramic holder, or boat, and placed in the center of the furnace. Breathing air is flowed through the furnace at 30 sccm to aid in the process. The anneal process is carried out for 1 hour 45 minutes and results in a graded index diffused waveguide with an index change of approximately 0.019. The entire process flow for APE waveguides is pictured in Fig. 32.

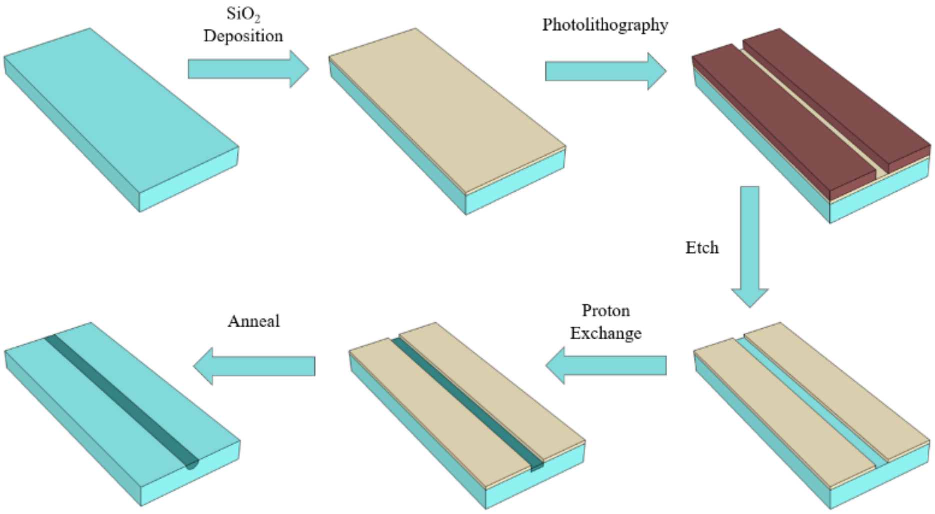

Fig. 32 Fabrication process flow for annealed proton exchange waveguides [20].

III.A.7. Polishing

After the waveguides have been formed, the edges of the sample must be polished to reduce optical losses when butt coupling a fiber to the waveguide. Dicing leaves the edges of the sample extremely rough and, therefore, a Struers MD Diamond Grit Polishing machine with diamond grit polishing pads of 15 µm, 3 µm, and 0.5 µm are used to make the edges as smooth as possible. Fig. 33 displays the edge of the sample after polishing with each respective pad. As can be seen, the right most picture shows the sample edge is free from visible defects, which will greatly reduce losses due to coupling.

Fig. 33 Edges of sample after polishing with the a) 15μm, b) 3μm, and c) 0.5μm pads, respectively.

A top view of the sample before and after polishing can be seen in Fig. 34. As is apparent, there is a visible roughness on the edge of the sample before polishing. After polishing, the edge is visibly smooth, which is ideal for edge coupling.

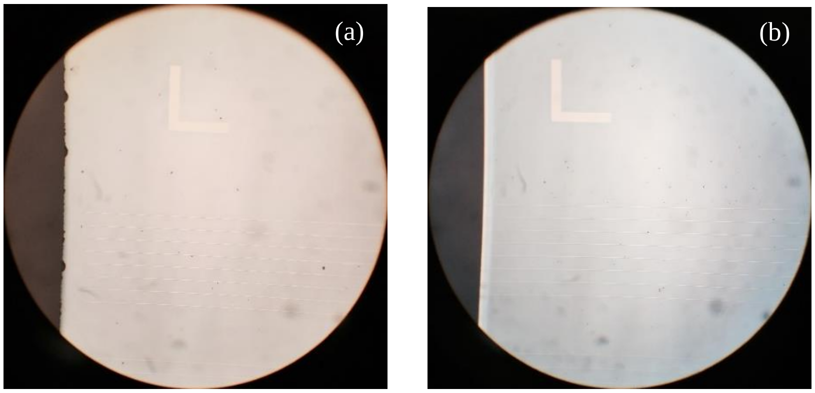

Fig. 34 Sample a) before and b) after polishing.

Now that the formation of the APE waveguides is complete, the waveguides are tested for optical quality. A LUNA OVA is used to find the insertion loss of the device. A fiber is butt coupled to the left and right edges of the sample that have been polished. The LUNA scans a wavelength range from 1525 nm – 1600 nm. Fig. 35 shows a plot of the insertion loss of a 3cm long $LiNbO_3$ APE waveguide that was exchanged for 30 minutes at 200°C and annealed for 1 hour and 45 minutes at 400°C. As is evident, the loss is approximately 2.5dB.

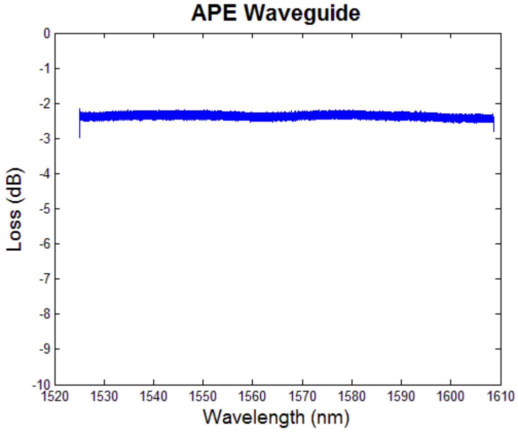

Fig. 35 Insertion loss for a 3cm long APE waveguide in $LiNbO_3$.

The mode profile of the APE waveguides are also characterized in order to determine fiber-to-waveguide mode mismatch. This is carried out by a ThorLabs Beam Profiler. The mode profile of a fabricated APE sample is pictured in Fig. 36. The measured mode field diameter of this APE waveguide is 10.66 µm. This data was entered into MATLAB where the mismatch factor and mismatch/coupling loss were calculated with the mode field diameter of a single mode fiber taken to be 10.7 µm. The MFD of the APE waveguide is very close to that of a standard single mode fiber, which will greatly reduce losses brought on by edge coupling.

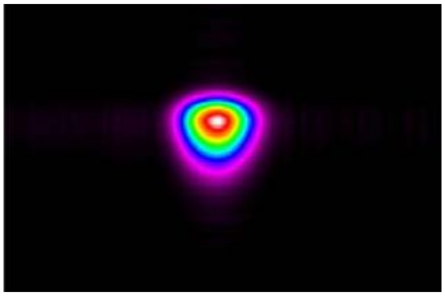

Fig. 36 Mode profile of annealed proton exchange sample with MFD of 10.66 µm.

III.B. Arsenic Trisulfide Waveguide Fabrication

The next step in the fabrication process is the formation of the As_2S_3 waveguides. The integration of these higher index (n=2.437) rib waveguides allows for a much more highly confined optical mode. This, in turn, allows for much higher steering angles because of the closer waveguide spacing that is permitted.

III.B.1. Sample Preparation

To begin the fabrication process for the As_2S_3 waveguides, the SiO_2 masking layer is removed by another photolithography step. This step preserves alignment marks and uses a buffered oxide etch (BOE) to remove only the SiO_2 in a windowed region where the As_2S_3 waveguides (and later the aluminum electrodes) will be placed.

III.B.2. Deposition

Next, a 600 nm layer of As_2S_3 is RF magnetron sputtered onto the sample. A protective layer consisting of a 150 nm layer of SiO_2 and a 45 nm layer of titanium (Ti) is also deposited to help protect the As_2S_3 from oxygen and $(CH_3)_4NOH$ based developers and strippers. Fig. 37 is an image of the view inside the deposition chamber during the

As_2S_3 deposition. The sample is attached to the sample holder, which is suspended and rotated above the target material. This allows the material to be uniformly deposited onto the surface of the sample.

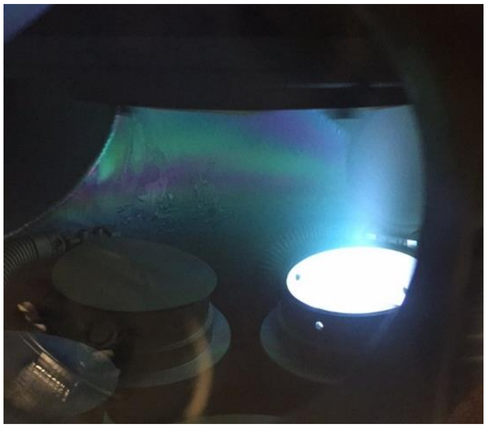

Fig. 37 View inside sputtering chamber during As_2S_3 deposition.

III.B.3. Electron Beam Lithography

Electron beam lithography is used to pattern the As_2S_3 waveguides because of the small taper tip widths needed for coupling the TE mode from the APE waveguides. Therefore, a subsequent photolithography step is performed to allow for the patterning of tungsten alignment marks. Once the photoresist is patterned and developed, a 250 nm layer of W is DC sputtered on top. Special care must be taken with the samples in this step to prevent the tungsten from being deposited where the As_2S_3 waveguides will be patterned because the tungsten will not be able to be removed at these locations. Fig. 38 displays a picture of the samples attached to the sample holder with the centers and edges covered for protection from tungsten.

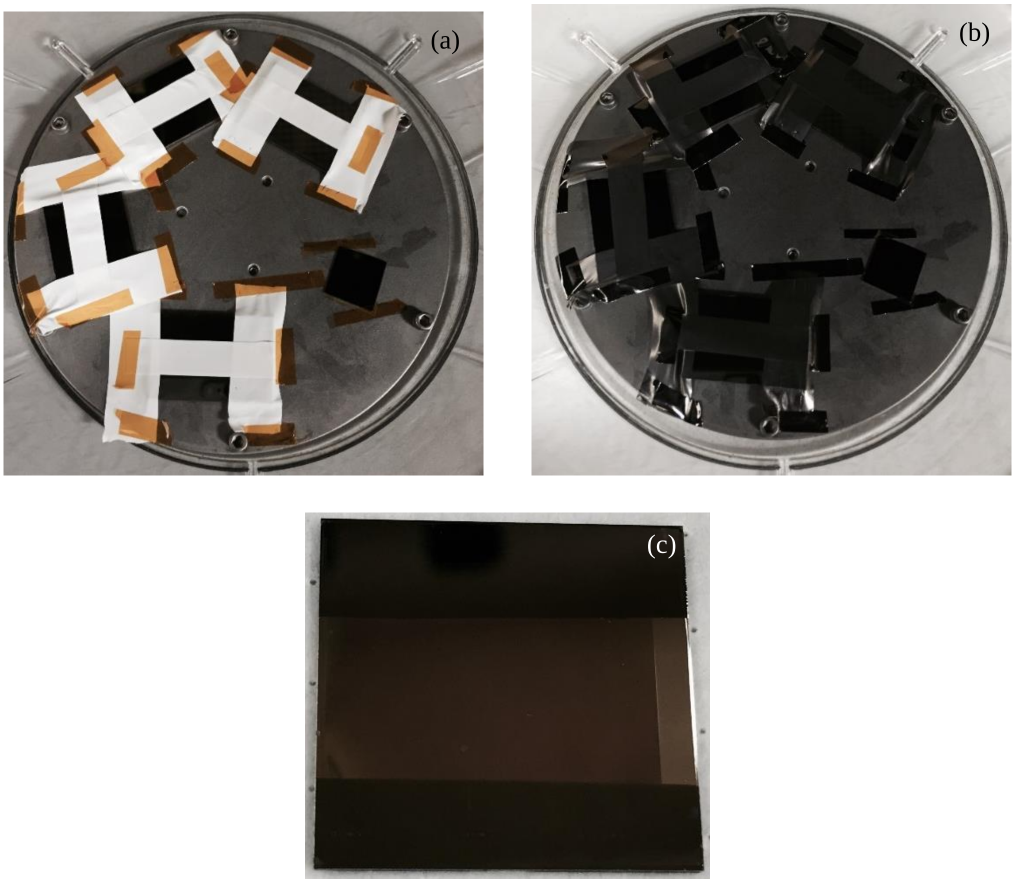

Fig. 38 Samples on sample holder with centers and edges covered (a) before and (b) after tungsten deposition and (c) after removing protective cover and sample from holder.

After photolithography, acetone is used to lift-off the W where the resist remains to create the alignment marks. The sample is suspended face down in a beaker filled with acetone. It is left in this state for 3 minutes, after which, the beaker with the sample in it is placed in a sonicator for an additional 3 minutes. It is imperative to deposit a silicon dioxide protective layer that is of precise thickness. If this layer becomes excessively thick, the stress between the SiO_2 and Ti layers becomes too high causing the Ti to peel off during the lift-off process. This occurrence is pictured in Fig. 39 with a silicon dioxide protective layer thickness of 200 nm.

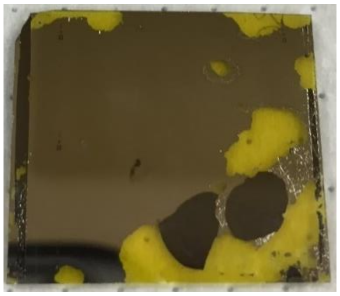

Fig. 39 Sample with 200 nm thick SiO_2 protective layer after tungsten lift-off exhibiting titanium peel off.

Fig. 40 shows an image of the cross hair alignment mark used for EBL and the smaller photolithography alignment marks below.

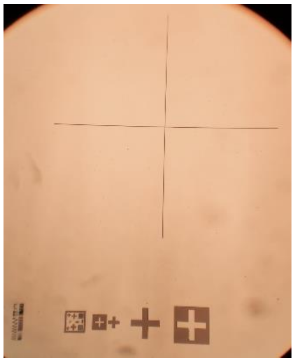

Fig. 40 Large cross hair EBL alignment mark on top and photolithography alignment marks on bottom.

For the electron beam lithography process, a JOEL JBX 5500FS electron beam writer at the University of Houston Nanofabrication Facility is used. PMMA positive resist with a mixture of 950C 9% PMMA and the corresponding thinner with a volume ratio of 1:3 is spin coated on to the surface of the sample at 2500 RPM for 1 minute. The sample is soft-baked on a hotplate at 180°C for 2 minutes. After that, the samples are placed, one at a time, on a piece-wise sample holder, as seen in Fig. 41. The sample is placed face down and in such a manner that the write area is exposed in the quarter circle region and must be aligned within the angle offset tolerance of the electron beam writer.

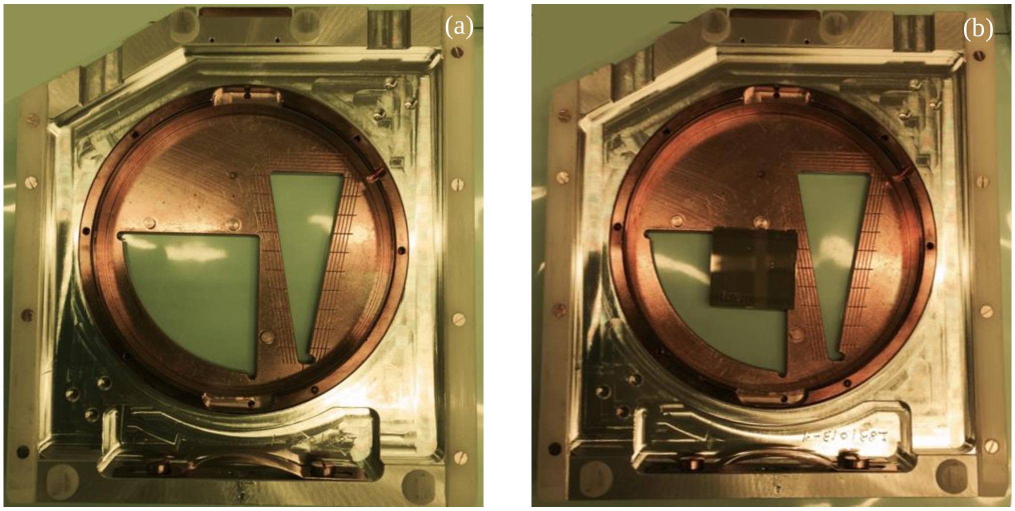

Fig. 41 Electron beam lithography piece-wise sample holder (a) without and (b) with sample in place.

A GDSII mask file of the waveguide layout is input into the e-beam writer software. A screenshot of the GDSII file can be seen in Fig. 42. This software aligns a specified point of the mask file to the tungsten alignment marks that were created earlier. Once the alignment is complete, the As_2S_3 waveguides are patterned with a dosage of 350 μC/cm^2 and subsequently developed in a mixture of 100 mL IPA and 50 mL DI water for 1 minute with agitation. For further details of the electron beam lithography step, see [46].

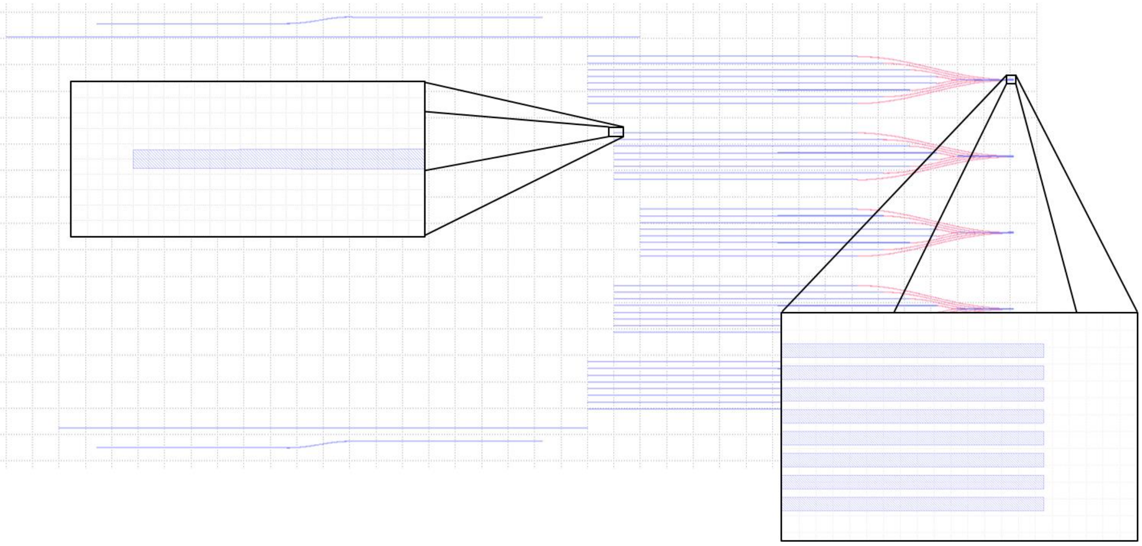

Fig. 42 GDSII Waveguide layout of As_2S_3 waveguides. Left projection: Taper tip of an input waveguide. Right projection: Output waveguide array.

III.B.4. Etching

After the As_2S_3 waveguides are patterned and developed, an oxygen ash is performed to remove residual resist. A 30nm layer film of chromium (Cr) is deposited by a Lesker PVD 75 e-beam evaporation and lift-off is performed. Once that is finished, another RIE step with the same parameters as above is completed. The etch rates are approximately 10 nm/min for Ti, 60 nm/min for SiO_2, and 1000 nm/min for As_2S_3. Fig. 43 displays the As_2S_3 waveguide structure up to this point. As seen in the upper left image, the As_2S_3 taper tips are aligned on top of the faintly visible APE waveguides. These are fanned out at a 127 µm pitch, which allows for easy coupling of a 1x8 PLC fiber array to the APE waveguides. The upper right image exhibits the output of the As_2S_3 waveguide array with 1.6 µm width and 1µm pitch.

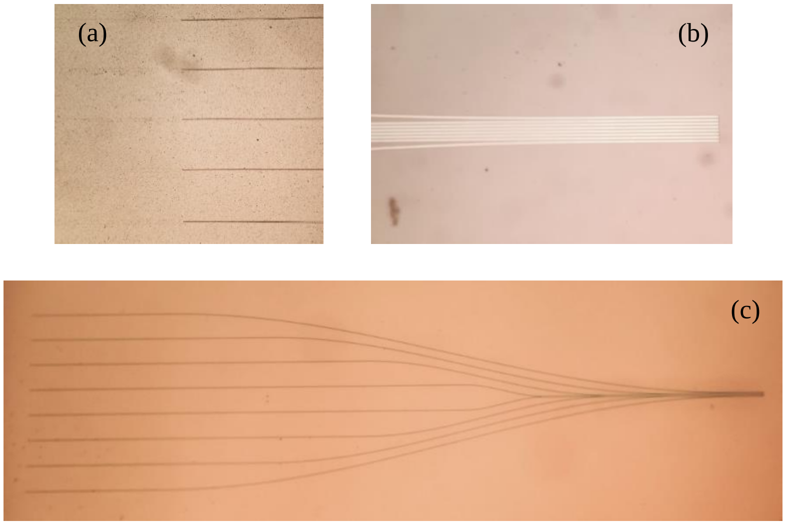

Fig. 43 a) Input taper tips, b) output array, and c) entire As_2S_3 waveguide structure.

Next, a wet buffered oxide etch is used to remove the protective layer from the As_2S_3 waveguides and chrome etch is used to remove any residual chromium. The last step in the As_2S_3 fabrication process is the deposition of a 150 nm buffer layer of SiO_2 by RF magnetron sputtering. The entire process flow of the As_2S_3 waveguide fabrication can be seen in Fig. 44.

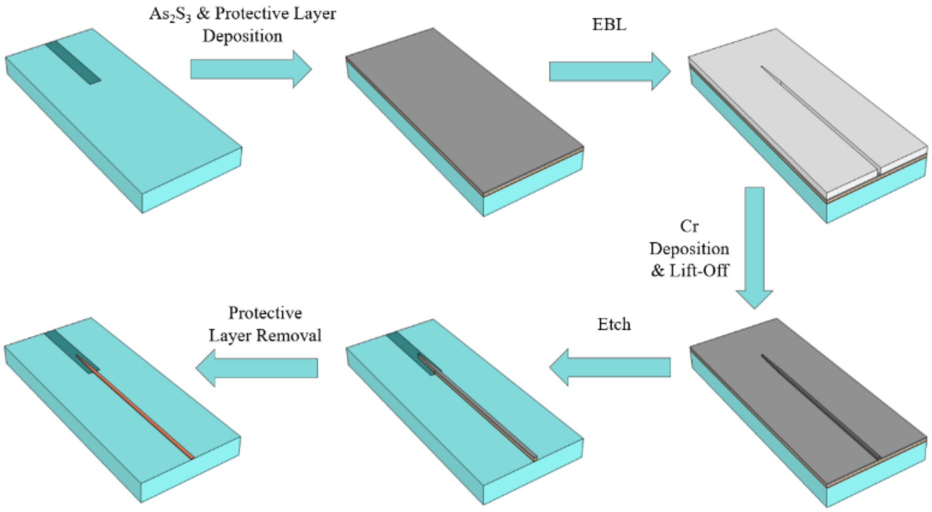

Fig. 44 As_2S_3 fabrication process flow [20].

The designed taper tip widths for this device are 0.5 μm with output widths of 1.6 μm. As seen in Fig. 45, the scanning electron microscope images show slightly smaller dimensions that are in agreeance with the designed numbers.

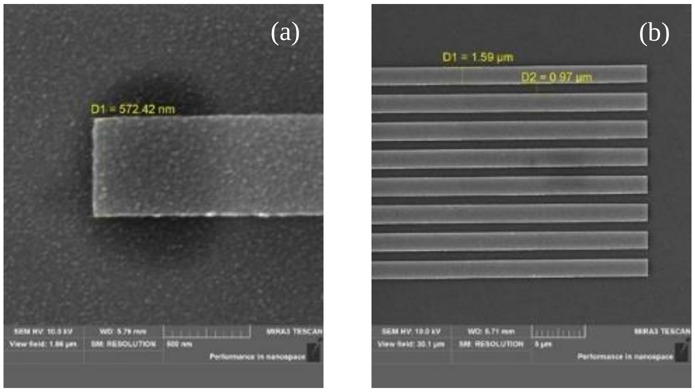

Fig. 45 SEM images of a) taper tip and b) array outputs [20].

III.C. Aluminum Electrode Fabrication

The final step in the fabrication process is the fabrication of the aluminum electrodes. A 500 nm layer of Al is deposited by DC magnetron sputtering. Photolithography is performed to pattern the areas where the electrodes will be formed. The mask has two different electrode designs, each having electrode arrays with different parameters. Fig. 46 displays the photolithography mask with one of the ten electrode arrays projected.

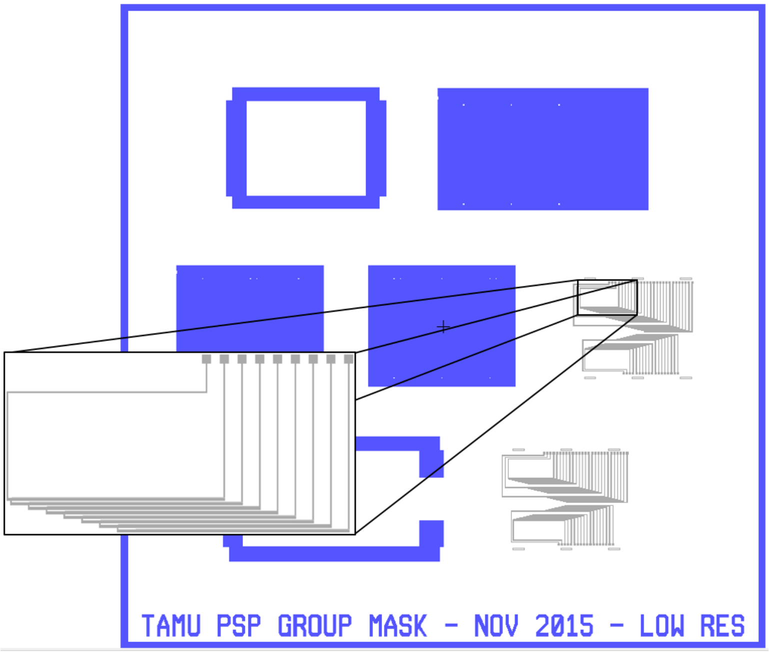

Fig. 46 Photolithography mask for aluminum electrodes. Projection: One of ten electrode arrays included on the mask.

After development, aluminum etchant is used to remove the unwanted Al. Proper alignment during the lithography processes is crucial for the performance of the device. If there is misalignment in any step, it could lead to high coupling losses or the electrodes not functioning properly. Fig. 47 displays an optical microscope image of the alignment marks used in the photolithography processes. As can be seen, the alignment of the aluminum layer with the tungsten alignment marks from the As_2S_3 waveguide fabrication process and the SiO_2 mask alignment marks from the APE waveguide process are very precise.

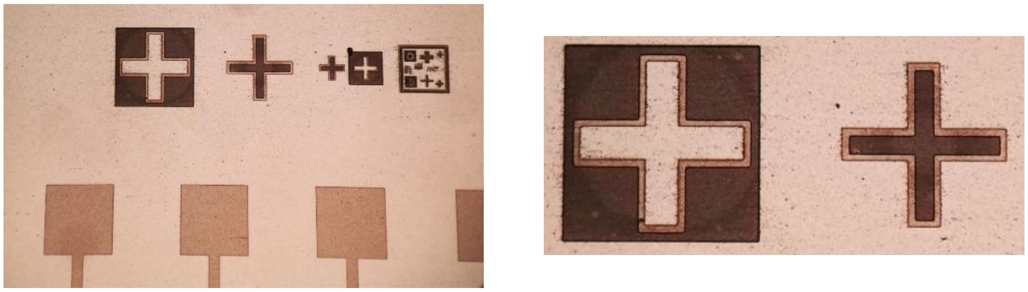

Fig. 47 Alignment marks after SiO_2 mask, tungsten, and aluminum photolithography processes.

Fig. 48 shows the process flow for patterning the Al electrodes. This is the region in which the electro-optic tuning will occur. After the tuning takes place, the light will be coupled into the As_2S_3 waveguides and output from the array of 8 As_2S_3 waveguides. The total dimensions of a complete OPA are approximately 14 mm x 2 mm with the limiting factors of the length and width being the electrode length and the APE/As_2S_3 fan-out, respectively.

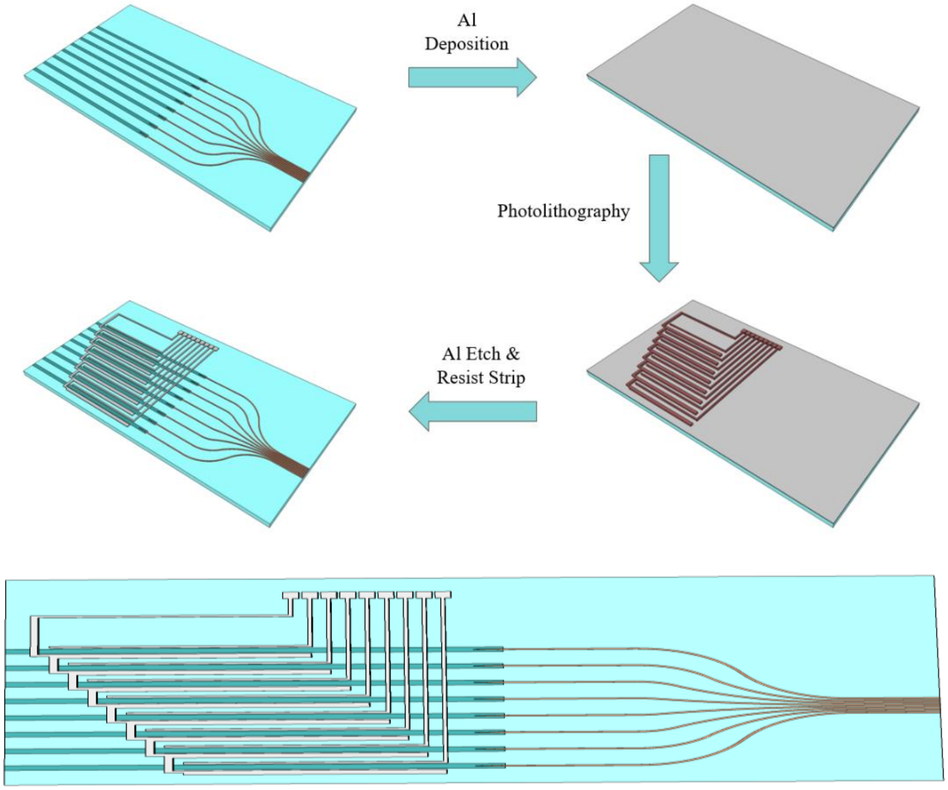

Fig. 48 Aluminum electrode fabrication process flow and completed device [20].

Fig. 49 shows the patterned Al electrodes surrounding the APE waveguides. Also shown in the bottom picture of Fig. 49, is the completed hybrid APE-As_2S_3 optical phased array.

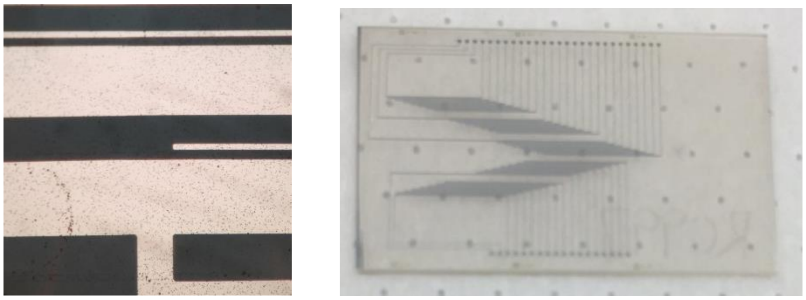

Fig. 49 Patterned aluminum electrodes and completed device.

III.D. Dicing and Polishing

The As_2S_3 waveguides are not fabricated to the edge of the sample. Therefore, after the electrode fabrication is complete, another dicing and polishing step is needed for the output As_2S_3 waveguides to be on the edge of the $LiNbO_3$ chip. This is a difficult task because peel-up of the As_2S_3 waveguides can occur. The first picture in Fig. 50 shows the As_2S_3 waveguide array before dicing occurred, and the second and third images picture the array after dicing. As can be seen, the As_2S_3 waveguides have peeled up.

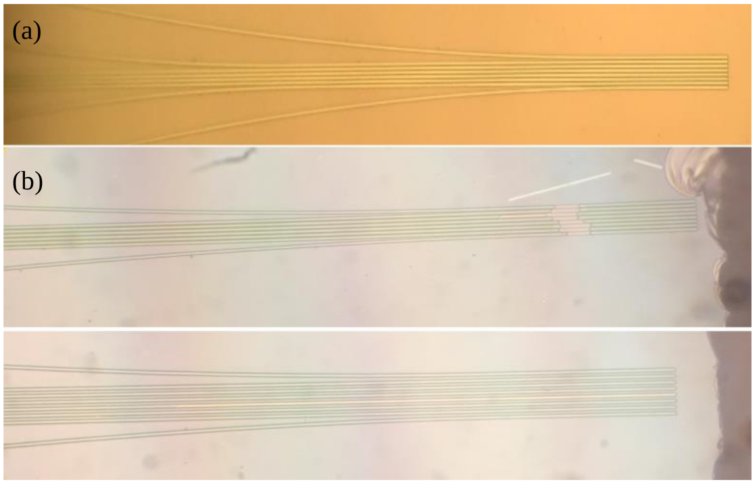

Fig. 50 As_2S_3 waveguide array (a) before dicing and (b) after dicing.

To combat this, dicing and polishing can be occur directly after the aluminum thin film layer has been deposited and before the electrodes are patterned. This process can, thus, use the 500 nm aluminum layer as a protective layer for the As_2S_3 waveguide array.

III.E. Thin Film Measurements

A Filmetrics thin-film measurement system was used to characterize the SiO_2 and As_2S_3 films that were deposited on dummy silicon samples. This setup can be seen in Fig. 51. We need to find the thickness, refractive index, and the extinction coefficient of the deposited films in order to confirm that they match well with the designed parameters from simulations and that they are of good optical quality so that reliable results are obtained.

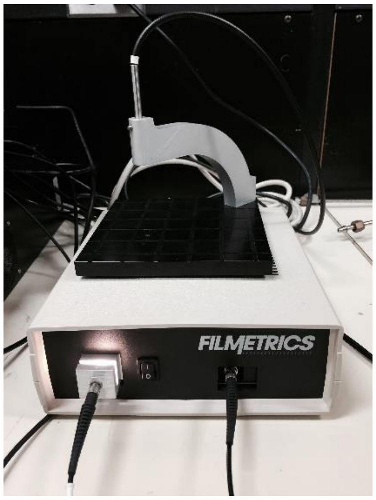

Fig. 51 Filmetrics thin-film measurement system.

As an example, the reflectance plot that was calculated and measured by Filmetrics for test runs of SiO_2 and As_2S_3 can be seen in Fig. 52. The calculated and measured data have good agreement, which tells us that the numbers calculated should be accurate. For the SiO_2, a 30 minute run was performed, which gave us a film thickness of 1188 Å and a refractive index of 1.461 at 640 nm. For reference, fused silica has a refractive index of 1.457 at 640nm. These are desirable numbers for the SiO_2 test run and give a deposition rate of 0.66 Å/s. The As_2S_3 test run gave a refractive index of 2.6099 at 640 nm and a thickness of 1323 Å. For reference, bulk As_2S_3 (e.g. our target) should have a refractive index of 2.6004 at 640nm, so we are in excellent agreement with optical quality As_2S_3 films.

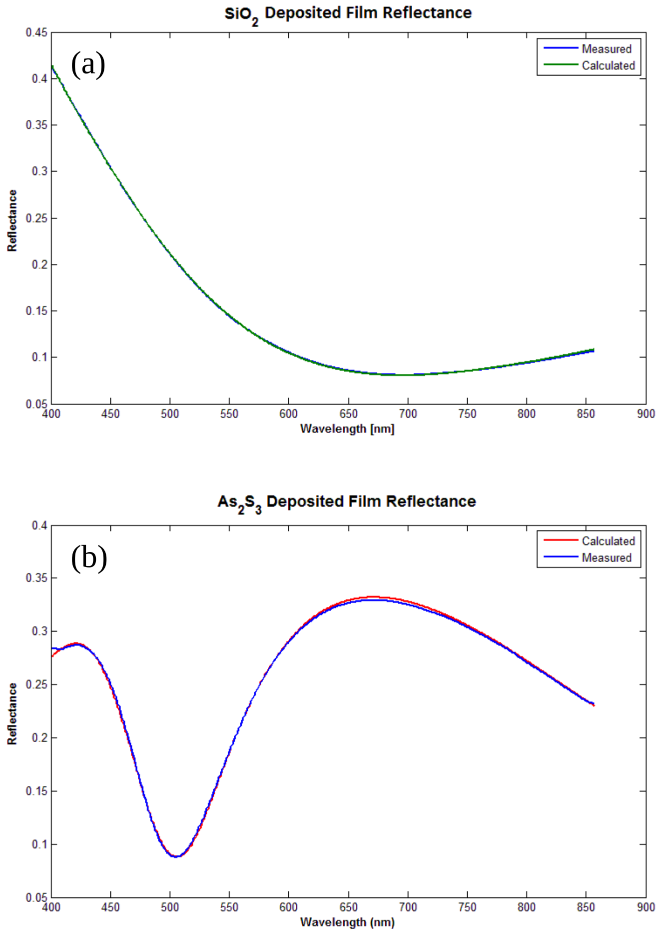

Fig. 52 a) SiO_2 and b) As_2S_3 deposited film reflectance.

For the films that are not optically transparent in the wavelength range of the Filmetrics, such as Ti, W, and Al, a Bruker DektakXT surface profilometer was used to measure the film thickness, Fig. 53. The Dektak uses a fine tip stylus with a radius of 12.5 µm that runs along the surface of the film and measures any surface variations. This machine has a scan length of 50 µm to approximately 30 mm and a vertical range of 65.5 nm. The vertical data resolution is 5 Å, which is sufficient for our film measurement needs.

Fig. 53 Bruker DektakXT surface profilometer.

Shows a dummy silicon sample with a thin film of titanium deposited onto the surface. The exposed region of the silicon substrate was formed by first marking the dummy silicon with a Sharpie marker before deposition. After the deposition is complete, an acetone soaked q-tip is used to "lift-off" the deposited film that covers the marked area.

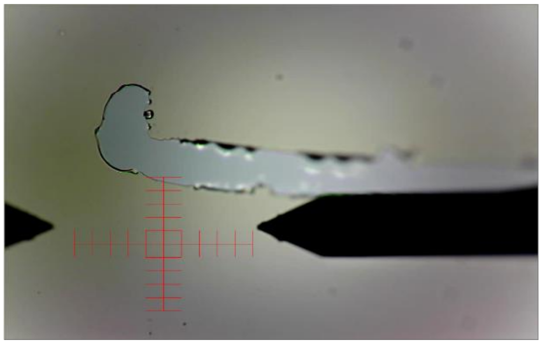

Fig. 54 View of deposited dummy sample and Dektak stylus.

The surface profile of this Ti sample along with W and Al samples can be seen in Fig. 55. The Dektak gives a thin-film thickness of approximately 460 Å for the titanium film, approximately 250 nm for the tungsten film, and approximately 500 nm for the aluminum film which are all in agreement with the desired thicknesses. The artifacts (high peaks) on the film of the titanium sample can be attributed to film disruption during the q-tip swab.

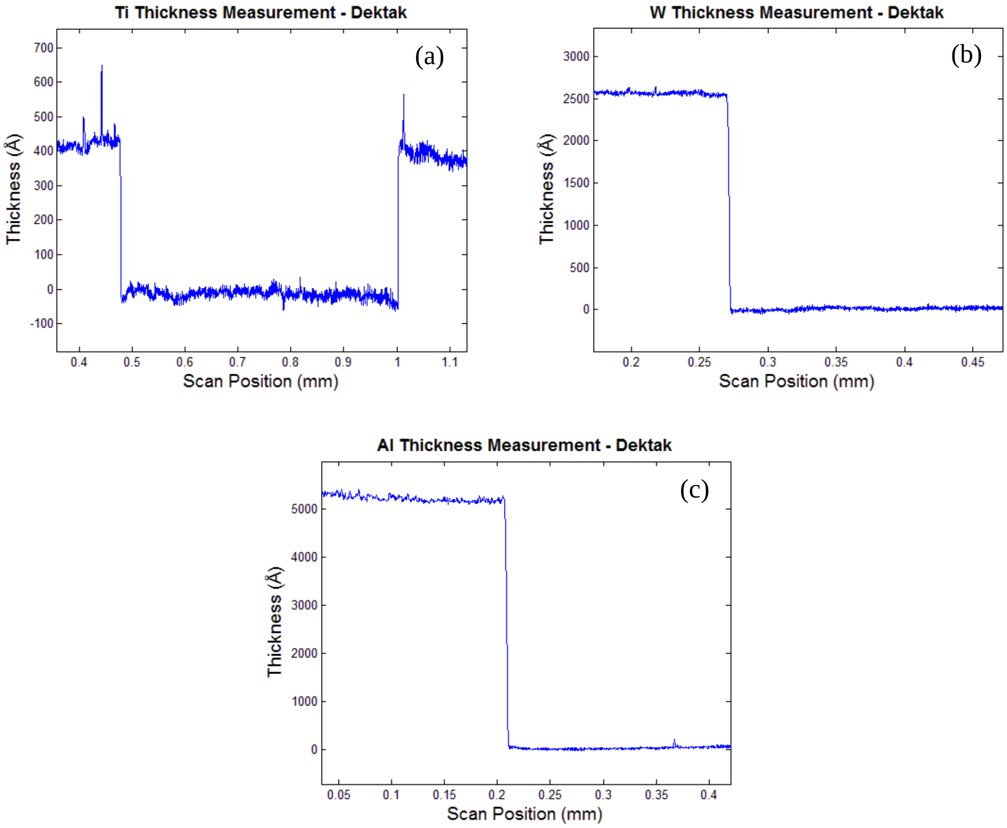

Fig. 55 Surface profile of a) titanium, b) tungsten, and c) aluminum thin-films from Bruker Dektak Profilometer.

CHAPTER IV

MEASUREMENTS & RESULTS*

In order to obtain accurate measurements, a robust measurement setup must be constructed. The initial test measurement setup includes three main component groups: the laser, translation stages for the optical fiber and DUT, and the imaging optics with an IR camera. All of these components work together on an optics table to provide precise alignment for accurate measurements, Fig. 56. 1550 nm light is output from a laser to a 1x8 PLC fiber array and the fiber array is butt coupled to the fabricated device. The light output from the device is coupled through a series of lenses that focuses the light on the sensor of an IR camera.

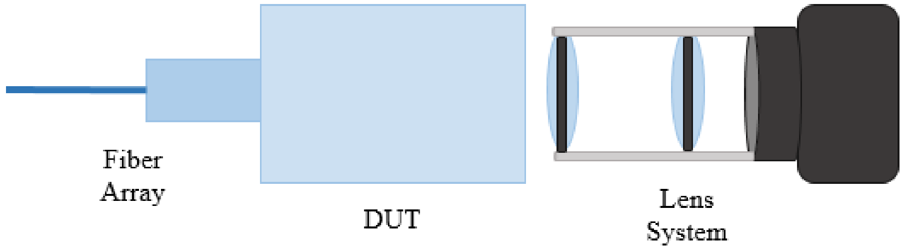

Fig. 56 Initial optical phased array measurement setup.

---

[*] Part of the data reported in this chapter is reprinted from D. D. Macik, T. E. Bravo, S. M. Pentecost, F. A. Espinal, and C. K. Madsen, “Optimization of electro-optic phase shifters for integrated optical phased arrays,” *Proc. SPIE*, vol. 10181, pp. 1018105-1 – 1018105-10, 2017.

IV.A. Fourier Optics

Being able to measure the near-field and the far-field of this device is an important part of the measurement setup. Therefore, a three lens Fourier optics system [47] was employed. Two lenses are always in the setup; this images the near-field pattern of the array onto the IR camera. A third lens can be inserted between the first two, to image the far-field pattern of the array. Fig. 57 visually displays the three lens setup. The red line represents a ray trace of the light when only lenses L_1 and L_3 are in the setup, which focuses the near-field pattern on the IR camera. When lens L_2 is inserted, the green line represents the ray trace of the light, which focuses the far-field on the IR camera.

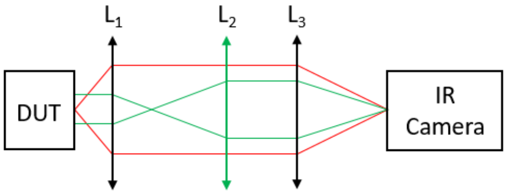

Fig. 57 Three lens near-field and far-field imaging setup.

The numerical aperture of the first lens is determined by the angular acceptance of light that is desired and is established by the optical phased array. Because the dimensions of the hybrid OPA allow for a maximum steering angle of approximately 34°, an acceptance angle of 35° is used for calculations. Where the angular acceptance is given by

$$a = 2\sin^{-1}\mathrm{NA} = 2\tan^{-1}\frac{D/2}{f}\ . \tag{74}$$

D is the diameter of the lens and *f* is the focal length of the lens. This concept is visualized in Fig. 58, below. Solving for NA and using an acceptance angle of 35° yields a numerical aperture of 0.3. Therefore, lens L_1 has an NA of 0.39 and focal length of 15 mm. Lenses L_2 and L_3 were chosen to have focal lengths of 100 mm and 50 mm, respectively.

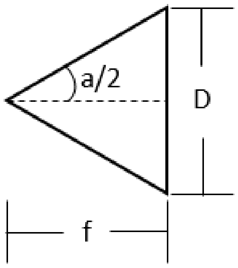

Fig. 58 Angular acceptance of a lens [21].

IV.B. Fiber Array Measurements

As a first test of the functionality of the setup, the 1x8 PLC fiber array was measured. Fig. 59 shows a drawing and a picture of the near-field imaging setup, with lens L_2 removed. As mentioned above, this allows for the imaging of the near-field intensity pattern. The near-field of the 1x8 PLC fiber array, as captured by the IR camera, is also shown.

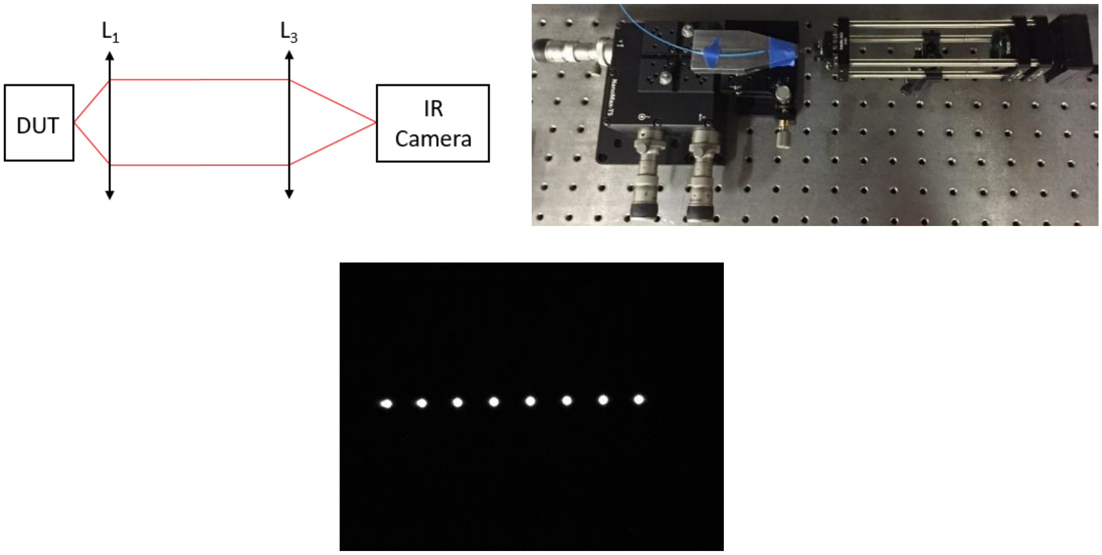

Fig. 59 Near-field imaging setup and near-field pattern of 1x8 PLC fiber array.

Next, lens L_2 was inserted into the setup so that the far-field intensity pattern of the 1x8 PLC fiber array could be observed. Fig. 60 shows a drawing and a picture of the far-field imaging setup, with all three lenses in the system. Also, a typical far-field intensity is observed with constructive and destructive interference of the output light. This confirms the functionality of the setup and leads to the measurement of the coupled APE:$LiNbO_3$ – Si_3N_4 optical phased array.

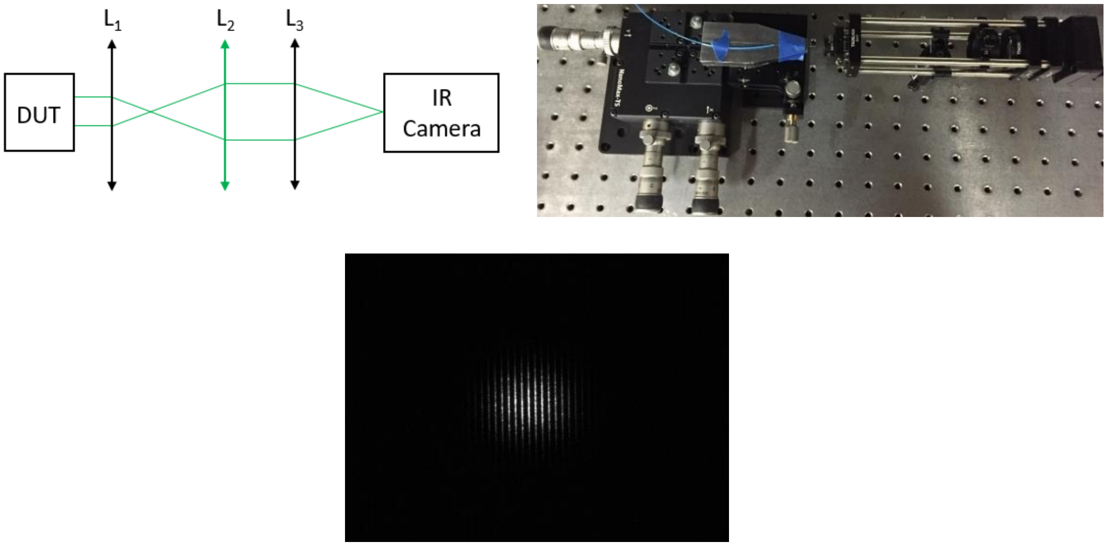

Fig. 60 Far-field imaging setup and far-field pattern of 1x8 PLC fiber array.

IV.C. OPA Measurement Setup

The OPA measurement setup consists of five main component groupings; the fiber stage, the APE:$LiNbO_3$ stage, the Si_3N_4 stage, the objective stage, and the lens system/camera stage. Each of these stages allows for at least 3 degrees-of-freedom with the fiber and Si_3N_4 stages having 5 DOF. The additional DOF for the fiber and Si_3N_4 stages allows for the tuning of the yaw and roll for better alignment with the APE:$LiNbO_3$ OPA. Fig. 63 displays an actual picture of the setup, as well as, a drawing of a linearized depiction for better comprehension of the optical components. This includes a 1x8 PLC fiber array that is edge coupled to the APE:$LiNbO_3$ OPA (DUT). This is also edge coupled to a Si_3N_4 8x8 waveguide array. The Si_3N_4 waveguide array utilizes the Triplex^{TM} waveguide structure which is designed for the fundamental TE mode at 1.55 µm, Fig. 61. This device has an effective index of 1.535 with a straight waveguide loss of 0.5 dB/cm.

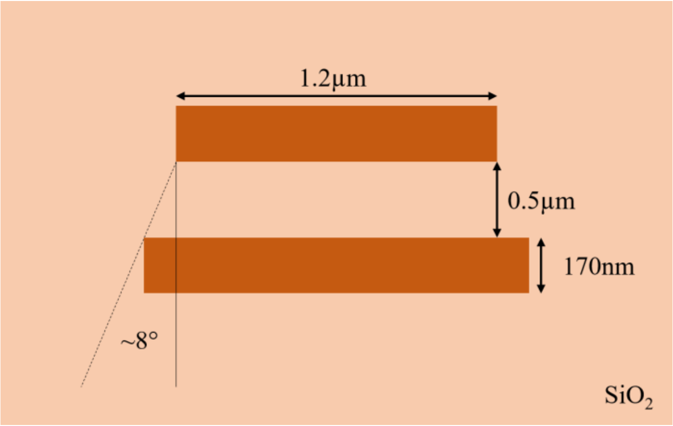

Fig. 61 Triplex^{TM} waveguide structure of Si_3N_4 waveguide.

Fig. 62 displays the layout of the 8x8 Si_3N_4 device with spot size converters on the input waveguides (right side) and tapered waveguide spacing on the output waveguides (left side). The reason for the spot size converters on the input waveguides is that this device will integrate to the output of the APE $LiNbO_3$ chip described above. It allows us to keep the tightly confined modes of the Si_3N_4 waveguides and closer spacing while taking advantage of the faster phase shifting of the $LiNbO_3$. This device has an output spacing of 5 μm which leads the useful scan zone to be approximately 14 ° and the far-field spot size to be 1.99 °.

(a)

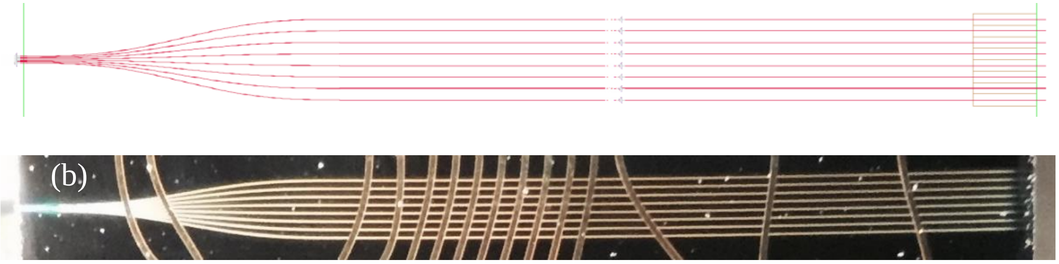

Fig. 62 8x8 splitter a) GDSII layout and b) actual device with spot size converters on inputs and tapered spacing on outputs.

The output of the Si_3N_4 waveguide array has a much smaller pitch than the 127 µm of the fiber array and APE:$LiNbO_3$ OPA, therefore, the output is coupled to a 40x microscope objective. This is used to magnify the output of the array to be adequately displayed on the detector of the camera. The last stage in the setup includes the Fourier optics lens system and camera configuration.

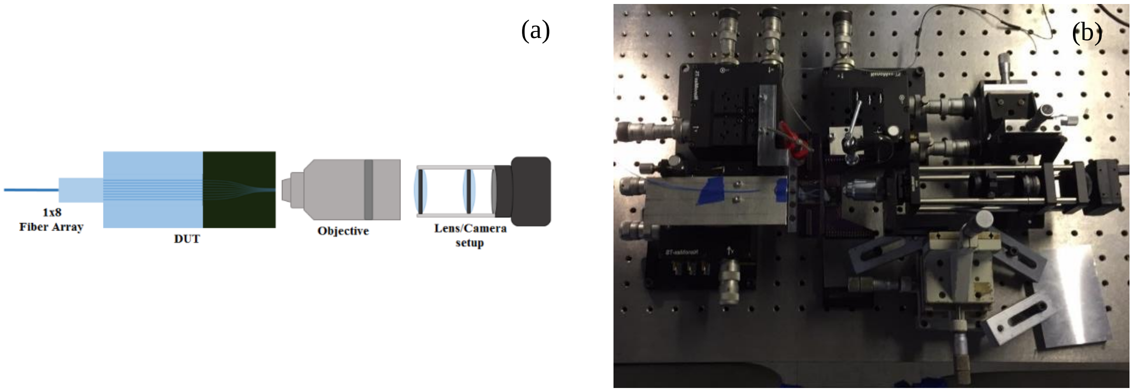

Fig. 63 (a) Drawing of simplified measurement setup with the main parts labeled and (b) a picture of the actual setup [21].

Fig. 65 pictures a closer look at the chip-to-chip optical coupling of the setup. Each chip has multiple arrays fabricated at various positions, thus, the two chips are mounted on two separate custom PCBs to allow for the alignment of the arrays of one chip to different arrays of the other. The APE:$LiNbO_3$ OPA is also wire bounded to the PCB in order to provide electrical control for phase tuning. Fig. 64 displays a schematic of the PCB along with the GDSII layout of the OPA. This helps visualize how each electrode is wired to the bonding pads located on the PCB. The right hand picture displays the actual wirebonded device with header pins to make the electrical connections.

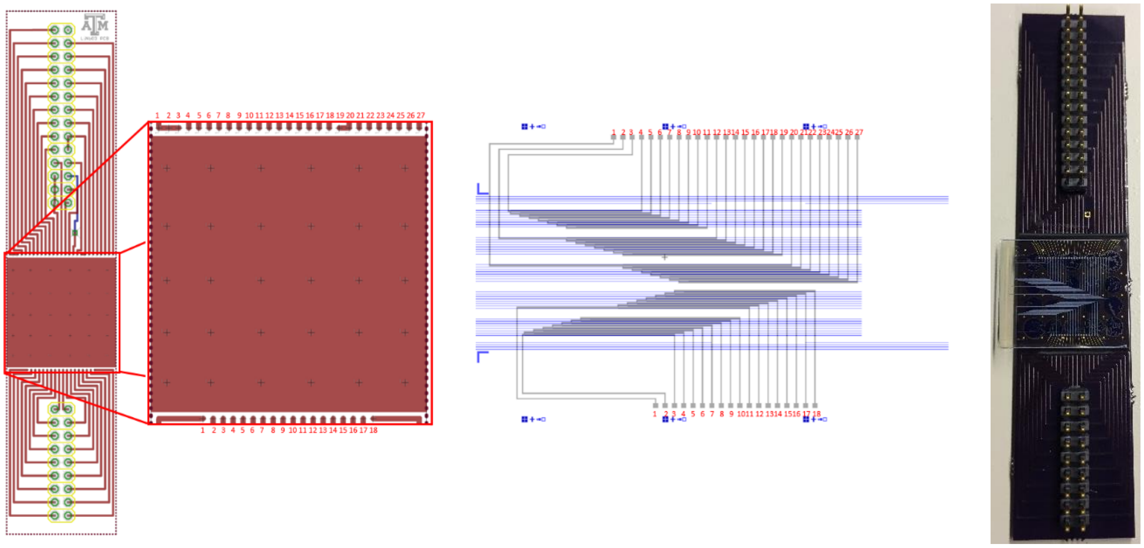

Fig. 64 PCB schematic and GDSII layout of OPA. Right hand picture is actual wirebonded device.

As mentioned earlier, the pitch of the APE:$LiNbO_3$ optical phased array has a large pitch of 127 µm. This is not only required for coupling to the fiber array and Si_3N_4 chip, but is also necessary to offer electrical isolation between adjacent electrodes.

Fig. 65 On-chip optical coupling portion of the setup. (a) Shows the 1x8 PLC fiber array coupled to the $LiNbO_3$ and Si_3N_4 chips and (b) shows a zoomed in vertical view of the edge coupling of the $LiNbO_3$ and Si_3N_4 chips [21].

Now that a microscope objective has been inserted into the Fourier optics system, the functionality has slightly changed. The system is still able to measure the near-field and the far-field of the output array, but the objective images the Fourier plane. Therefore, when lenses L_1 and L_3 are only in the setup, the far-field intensity pattern of the array is imaged onto the IR camera. When lens L_2 is inserted between the first, the near-field intensity pattern of the array is imaged. This is opposite from the setup above with no objective in place. Fig. 66 visually displays the new three lens setup. Again, when only lenses L_1 and L_3 are in the setup, the far-field pattern is focused on the IR camera and a ray trace of the light is represented by the red line. When lens L_2 is inserted, the near-field is imaged and the ray trace is represented by the green line. The same lenses from above were used for L_1, L_2, and L_3.

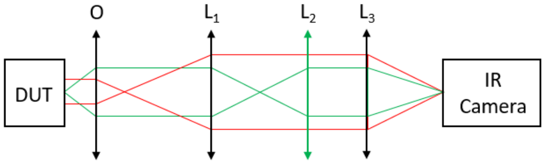

Fig. 66 Three lens near-field and far-field imaging setup with microscope objective [21].

IV.D. Voltage Control Hardware

The hardware used to apply a voltage across each element in the optical phased array is based on the Arduino platform. The Arduino is an open-source hardware device that grants the user a significant amount of design freedoms. The limiting factor of this device is the clock speed of 16 MHz. The complete hardware loop is displayed in Fig. 67, below. It consists of a 1.55 μm laser source, the optical phased array, the Arduino Mega with a custom designed shield, the IR camera that has transfer rates of up to 480 Mbits/s, and a computer.

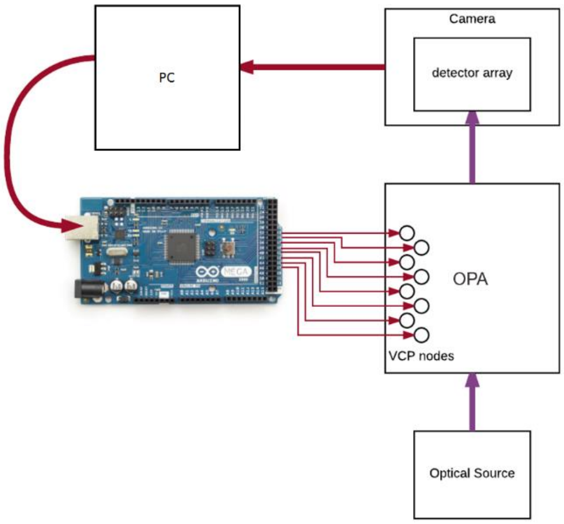

Fig. 67 Hardware loop for voltage control of the optical phased array.

As mentioned above, a custom shield was designed for the Arduino Mega, Fig. 68. This shield is vertically integrated which allows for the use of all of the pins of the Arduino. The control software, detailed in the next section, interfaces with the Arduino which outputs a PWM signal which is amplified by OpAmp circuits on the shield. This allows for a single high voltage source to be used to supply different voltages to each element in the optical phased array.

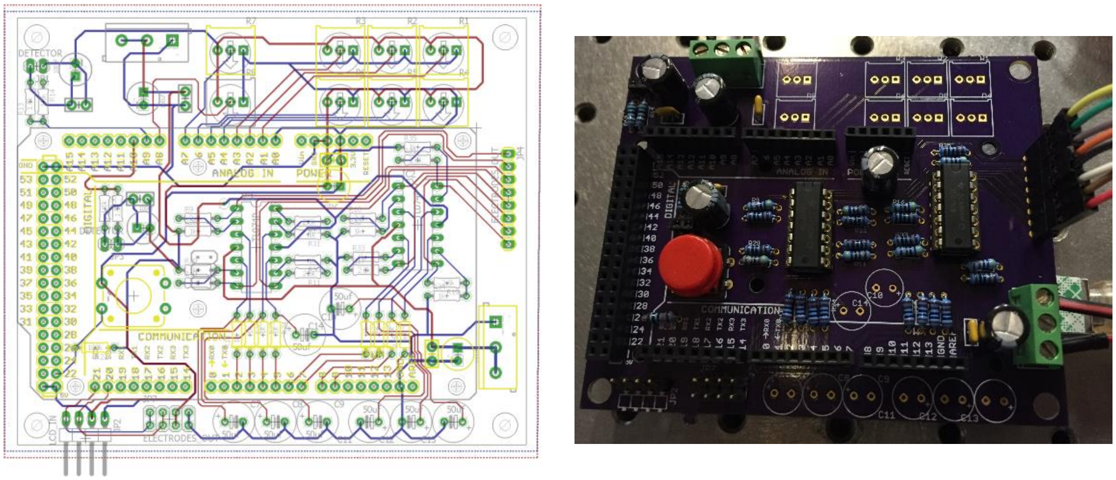

Fig. 68 a) Design layout and b) actual voltage control shield for the Arduino Mega.

IV.E. Phase Tuning Algorithm and Software

The tuning algorithm within the software is capable of allowing the far-field intensity pattern of the optical phased array to be tuned to any specified angle, within the confines of the parameter determined element factor and limited by the output mode widths. This tuning can be accomplished without any prior knowledge of the phase of each waveguide or element in the array. By choosing a desired steering position in the graphical interface, as seen in Fig. 69, and incrementally sweeping the voltage applied to the electrode of an array element, with each element being tuned individually, the far-field pattern will be tuned to the position represented by the red box in the upper left quadrant. The green line that is also pictured in this quadrant, represents the position of the cross-section of the image that will be displayed in the lower left quadrant. The upper right quadrant is where the voltages applied to each element, along with the measured intensity and steering positions, for each desired steering angle is stored with 8 different positions allowed to be saved to memory. This area of the software also allows for the auto tuning of the far-field intensity pattern to a specified angle and the exportation of the acquired cross section. Not only does this software allow for automatic tuning, but in the lower right quadrant has slider that allow for the manual tuning of each element in the array.

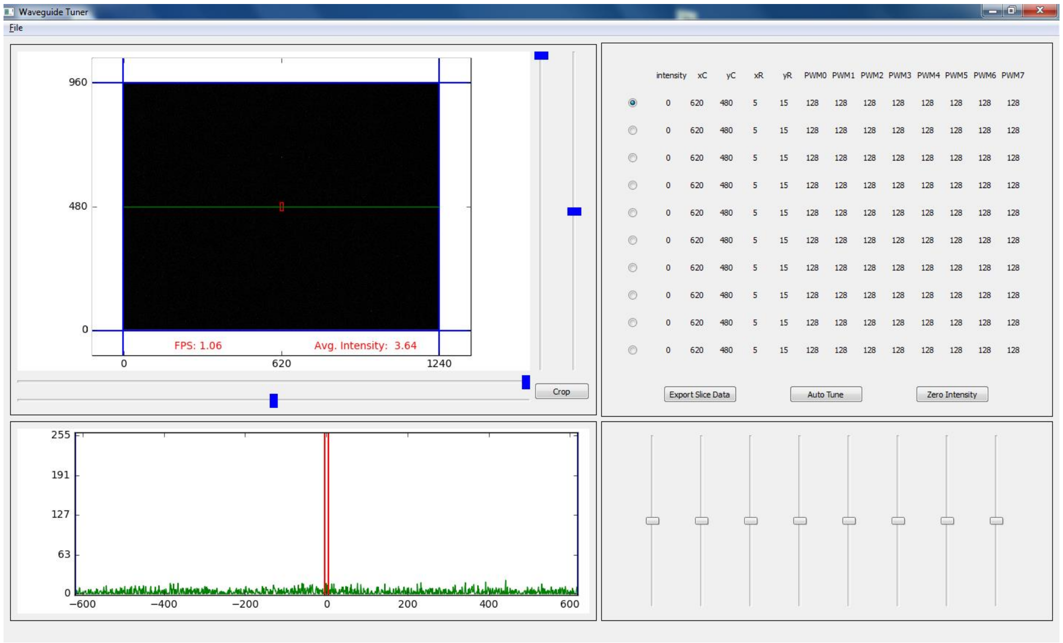

	intensity	xC	yC	xR	yR	PWM0	PWM1	PWM2	PWM3	PWM4	PWM5	PWM6	PWM7
●	0	620	480	5	15	128	128	128	128	128	128	128	128
○	0	620	480	5	15	128	128	128	128	128	128	128	128
○	0	620	480	5	15	128	128	128	128	128	128	128	128
○	0	620	480	5	15	128	128	128	128	128	128	128	128
○	0	620	480	5	15	128	128	128	128	128	128	128	128
○	0	620	480	5	15	128	128	128	128	128	128	128	128
○	0	620	480	5	15	128	128	128	128	128	128	128	128
○	0	620	480	5	15	128	128	128	128	128	128	128	128
○	0	620	480	5	15	128	128	128	128	128	128	128	128
○	0	620	480	5	15	128	128	128	128	128	128	128	128

Fig. 69 Graphical user interface of developed tuning software.

As mentioned above, during the sweep the software keeps track of the maximum intensity for each arm and the voltage that corresponds to it. Once the sweep of one element is complete, the voltage corresponding to the maximum intensity reading is applied to that element and the sweep of the next element. The progression of this sequence is carried out until the maximum intensity is found for every element. After that, a new position can be chosen and the process repeated. The voltage values pertaining to a previously tuned angle are stored in a look-up table for easy accessibility in the future. Fig. 70 graphically displays the process flow for maximizing the intensity of the far-field pattern at a specified position.

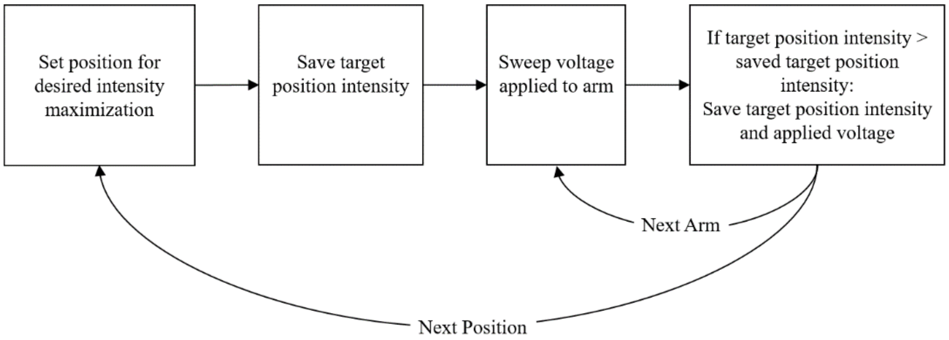

Fig. 70 Flowchart of software tuning process for maximizing the intensity of the far-field pattern at a specified position [21].

IV.F. APE:LiNbO$_3$ – Si$_3$N$_4$ Measurement Results

A laser with a wavelength of 1550 nm was used and coupled into the APE:LiNbO$_3$ OPA through the use of a 1x8 PLC fiber array. Both of these have waveguide pitches of 127 µm. The APE:LiNbO$_3$ OPA was, then, coupled to the input of the Si$_3$N$_4$ array which also has a 127 µm pitch. The output waveguide array of the Si_3N_4 device has waveguide widths of 1.2 µm with a pitch of 6.2 µm.

IV.F.1. Optical Phased Array Measurements

Before phase tuning was applied to the APE:$LiNbO_3$ optical phased array, the near-field intensity pattern of the output waveguide array was imaged onto the detector of the IR camera with the use of the Fourier lens system. Fig. 71 depicts the lens setup used to perform the imaging along with the actual near-field image acquired by the IR camera. This near-field intensity pattern allows for the calculation of a true magnification factor which is used to calculate the $1/e^2$ mode field diameter of the output waveguides.

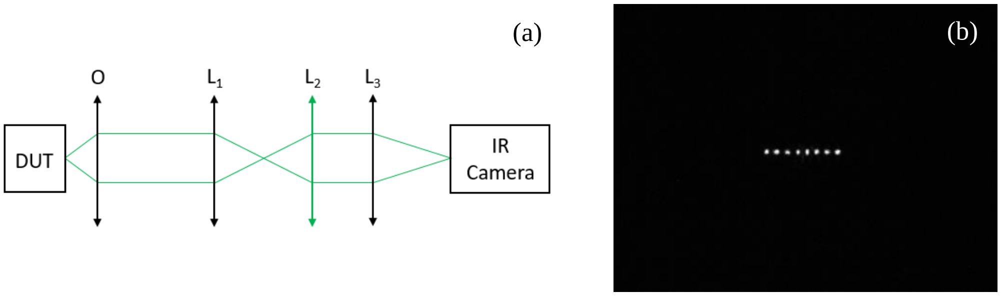

Fig. 71 (a) Lens setup used to image the near-field pattern of the output waveguide array and (b) the near-field pattern captured by the IR camera [21].

Now, in order to image the far-field intensity pattern of the Si_3N_4 output waveguide array, lens L_2 is removed from the lens system. A drawing of the lens setup, as well as the actual far-field intensity pattern, can be seen in Fig. 72. The far-field image exhibits a noticeably scattered pattern. This is because the phase of each element in the OPA are initially random. The contributing factors of this is the fact that the elements have different lengths and that there are slight fabrication differences, within tolerance, throughout the device.

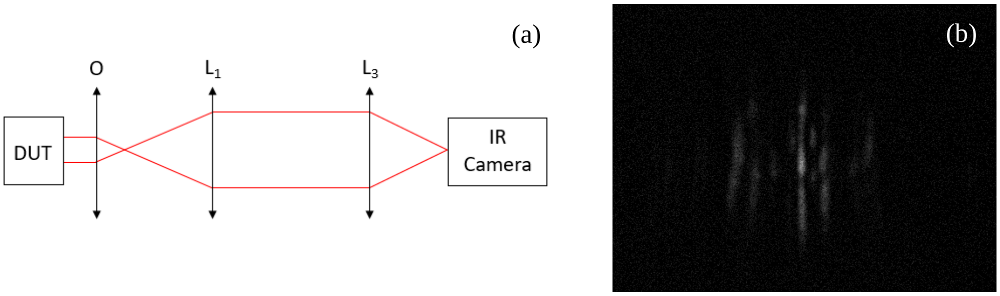

Fig. 72 (a) Lens setup used to image the far-field pattern of the output waveguide array and (b) the far-field pattern captured by the IR camera [21].

As mentioned above, the phase tuning software does not require any previous knowledge of the phase of each element or output waveguide. Therefore, after the far-field intensity pattern is found and displayed in the graphical interface of the tuning software, any allowable tuning position can be chosen and the software can be run. The phase tuned condition, or in other words the condition that every element in the array is in phase with one another, after one iteration or complete loop of the software is pictured in Fig. 73. The horizontal profile of the measured far-field intensity pattern obtained from the software along with the simulated far-field pattern are also given. As is evident, the side lobe levels of the measured far-field pattern are much smaller than those of the simulation. This is a desired result that shows that the element factor is not as wide as initially thought. These results will be discussed further, below.

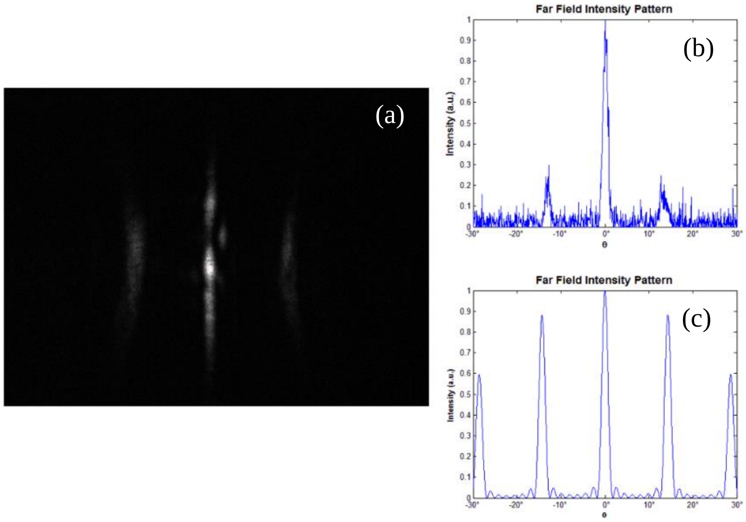

Fig. 73 (a) Image of the phased tuned far-field intensity pattern, (b) horizontal intensity profile of the measured far-field pattern and (c) the horizontal intensity profile of the simulated far-field pattern [21].

Next, the far-field intensity pattern is tuned to approximately 7° which corresponds to a π-phase shift of the periodic pattern. The IR camera image of the far-field intensity pattern tuned to this angle is pictured in Fig. 74. As above, the horizontal profiles of the measured and simulated far-field intensity patterns are also included.

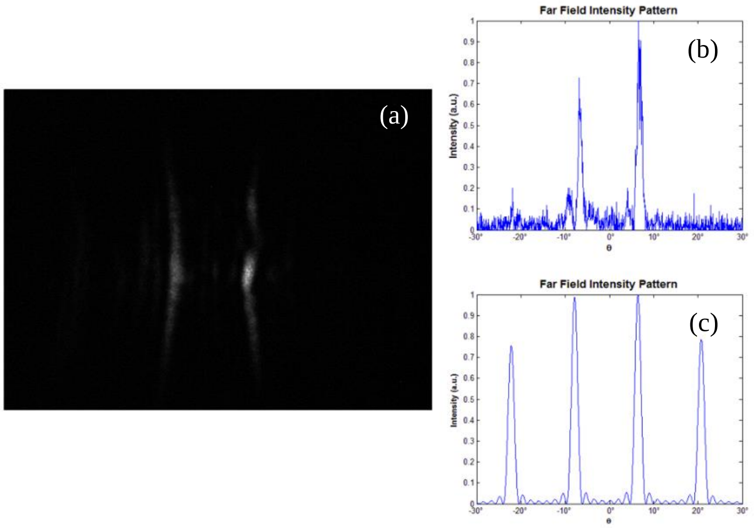

Fig. 74 (a) Image of the far-field intensity pattern tuned to approximately 7°, (b) horizontal intensity profile of the measured far-field pattern and (c) the horizontal intensity profile of the simulated far-field pattern [21].

As is evident from Fig. 73 and Fig. 74, the element factors of the simulated far-field pattern and the measured far-field pattern do not coincide. This can easily be explained by the MFD of the light from the output waveguides. During initial simulations of the optical phased arrays, the actual dimensions of the fabricated waveguide cores were used for the element width or individual aperture size. This is not a valid assumption as the optical mode extends beyond the boundaries of the physical waveguide core. Therefore, the waveguide width of 1.2 μm previously used was replaced with the $1/e^2$ MFD width of 4.15 μm found from the measured near-field intensity pattern of the output array. A comparison of the far-field intensity patterns of these two different simulated element widths along with the far-field intensity pattern of the measured results is displayed in Fig. 75. It can be seen that the element factor of the simulations match that of the measured data when using an element factor that is equal to the MFD of the optical mode from the Si_3N_4 output waveguides.

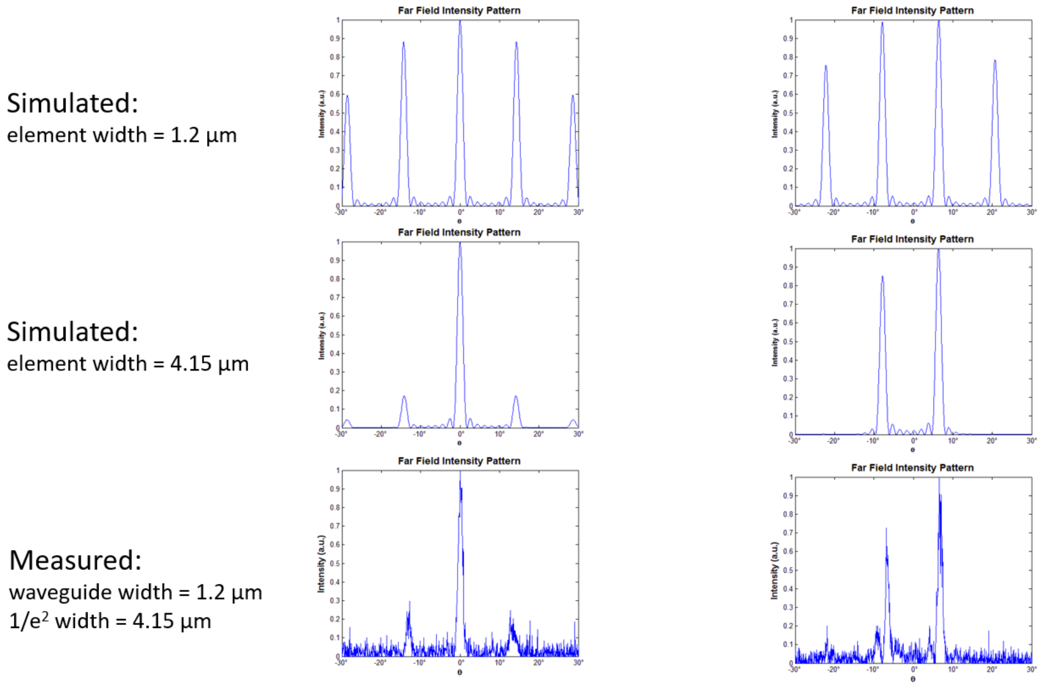

Fig. 75 Comparison of the simulated and measured far-field intensity patterns with a simulated element width matching the physical waveguide width and matching the $1/e^2$ mode width in the phase matched condition and with a π-phase shift [21].

IV.F.2. Magnification and Angle Calculations

In order to find the angle that the far-field intensity pattern of the OPA has been steered to, the pixels from the IR camera must be converted into an actual distance. Performing this conversion will allow the data to be plotted along the scan axis in degrees instead of being plotted in pixels as it is in the figures above. In order to do this, the removable lens L_2 was no longer used in the setup. This allowed for a more practical way of obtaining the steered angle of the far-field intensity pattern. Fig. 76 shows the measurement setup used for this operation. First, the near-field was obtained with the microscope objective, lens L_1, and lens L_3. Then, the far-field was obtained by translating the lens/IR camera system back a known amount. The green represents where the objects were previously located. After this data has been gathered, the pixel to angle conversion can be performed.

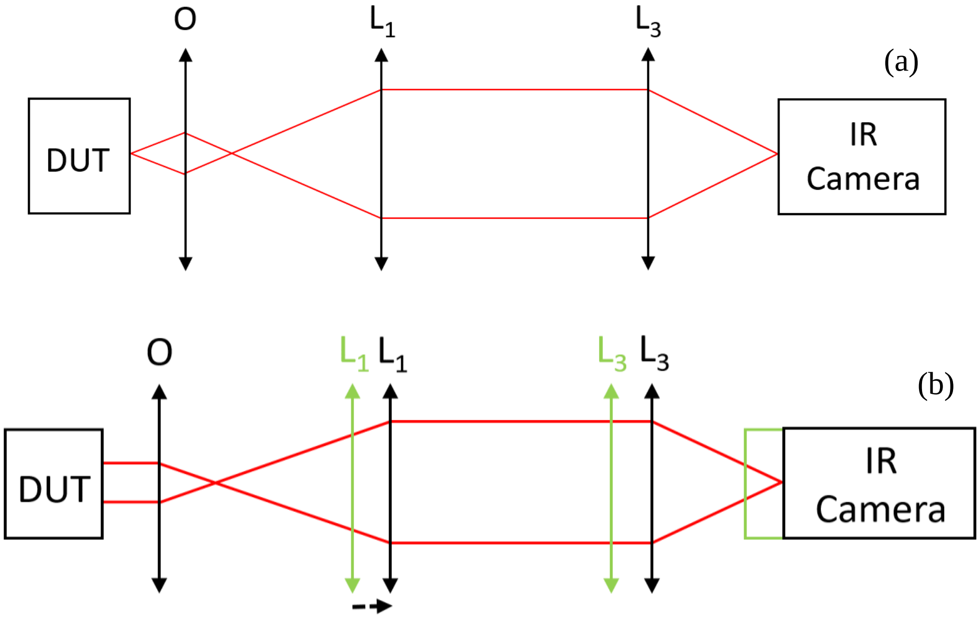

Fig. 76 Measurement setup used to measure the a) near-field and b) far-field intensity patterns of the optical phased array.

This can be done by first calculating the magnification of the output of the near-field intensity pattern. The magnification can be expressed as

$$M_{eff} = \frac{d_p p}{d} \tag{75}$$

where d_p is the pitch of the near field pattern in pixels as found from the IR camera image, p is the size of each pixel, and d is the pitch of the output waveguides of the array. Once this is complete, the free-space propagation distance can be found by

$$f_t = \frac{M_{eff} f_d}{M_d} = y \tag{76}$$

where f_t is the tube lens focal length and is equal to the free-space propagation distance y, f_d is the design tube lens focal length for the microscope objective, and M_d is the design magnification of the microscope objective. After this, the distance along the scan axis in pixels can be used to find this distance in degrees. The distance along the scan axis is given by

$$x = x_p p M_{eff} \tag{77}$$

where x_p is the distance along the scan axis in pixels. The scan axis in degrees can then be found by

$$\theta = \tan^{-1} \frac{x}{y} \,. \tag{78}$$

IV.G. Hybrid As_2S_3 – $LiNbO_3$ Measurement Results

After the proof-of-concept APE:$LiNbO_3$ – Si_3N_4 optical phased array was characterized, the hybrid device was measured. This device is integrated on a single chip which allows for the measurement setup to be simplified. The new setup is pictured in Fig. 77, below. The Si_3N_4 5 DOF stage has been removed leaving only four main component groupings; the fiber stage, the APE:$LiNbO_3$ stage, the objective stage, and the lens system/camera stage. The pitch of the 1x8 PLC fiber array and the input of the chip are the same 127 µm as earlier, but the output of the chip has the As_2S_3 waveguide arrays with an output pitch of 2.6 µm which will allow for a maximum steering angle of approximately 34°.

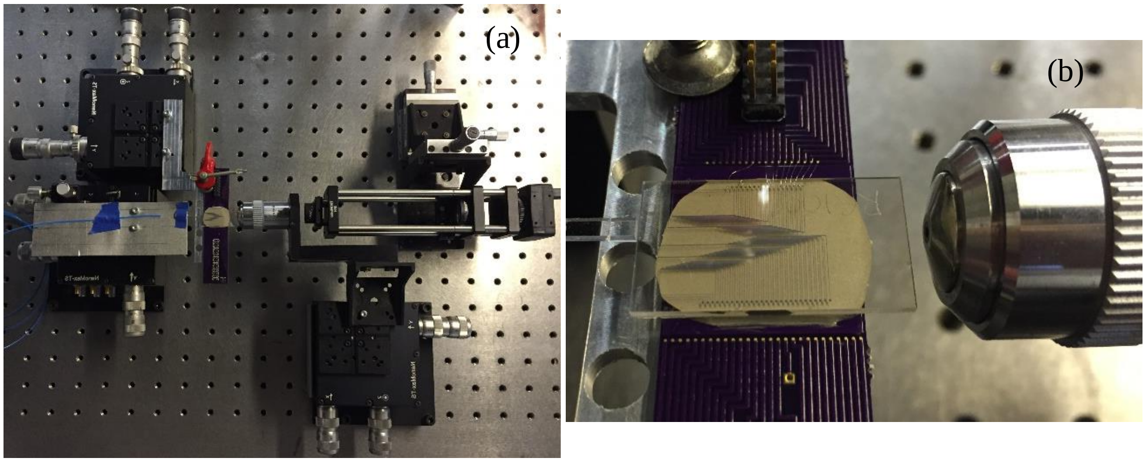

Fig. 77 Hybrid As_2S_3 – $LiNbO_3$ OPA measurement setup a) full view and b) zoomed in view of the coupling region.

The near-field and far-field intensity patterns of this device were both measured and are pictured in Fig. 78. As can be seen, there is a significant amount of noise from light diffraction which can be attributed to the fact that the As_2S_3 waveguides are not fabricated completely to the edge of the $LiNbO_3$ substrate due to fabrication limitations for in-house facilities. This hindered the ability to obtain meaningful beam steering results, but gave great insight into how future iterations of this device can be improved.

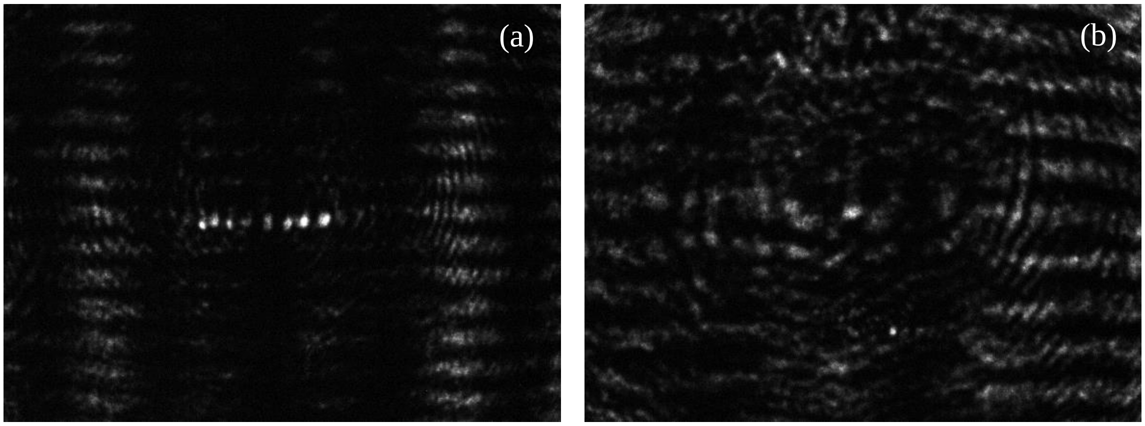

Fig. 78 Image of the a) near-field and b) far-field intensity patterns of the hybrid As_2S_3 – $LiNbO_3$ optical phased array captured by the IR camera.

CHAPTER V

CONCLUSIONS[*]

A low-loss hybrid annealed proton exchange waveguide with a vertically integrated arsenic trisulfide waveguide on a lithium niobate substrate has been fabricated and used to create an optical phased array that allows for the non-mechanical steering of 1.55 µm light. The expected APE propagation loss is as low as 0.2 dB/cm with a coupling loss of 1 dB and an As_2S_3 propagation loss of 1.2 dB/cm. This hybrid As_2S_3-$LiNbO_3$ device performs much better in this aspect in comparison to recent SOI OPAs, which have propagation losses of 1.8 dB/cm and coupling losses of 4 dB.

This is the first instance, to our knowledge, that such a device has been fabricated on an integrated $LiNbO_3$ substrate. While other optical phased array technologies have higher output waveguide pitch which hinders the maximum steering angle and suffer from slower steering speeds, this hybrid approach on a single $LiNbO_3$ substrate allows for the use of the high electro-optic coefficient of $LiNbO_3$ for fast tuning and the tight mode confinement of As_2S_3 for closer waveguide spacing and a 2π-steering angle of 34°. The near-field and far-field intensity patterns of this OPA were obtained which gave insights on how to further improve this device through fabrication and design modifications.

---

[*] Part of the data reported in this chapter is reprinted from D. D. Macik and C. K. Madsen, "Fabrication of $LiNbO_3$-As_2S_3 waveguides for beam steering applications," *Proc. SPIE*, vol. 9970, pp. 99700H-1 – 99700H-10, 2016 and D. D. Macik, T. E. Bravo, S. M. Pentecost, F. A. Espinal, and C. K. Madsen, "Optimization of electro-optic phase shifters for integrated optical phased arrays," *Proc. SPIE*, vol. 10181, pp. 1018105-1 – 1018105-10, 2017.

A low-loss annealed proton exchange waveguide array has also been fabricated and coupled to another chip to create an optical phased array that allows for NMBS. This device is edge coupled to a Si_3N_4 waveguide array fabricated with the Triplex^{TM} waveguide technology and has a narrow output waveguide pitch. These Si_3N_4 waveguides have a straight waveguide loss of less than or equal to 0.5 dB/cm. This coupled device performs much better, in this aspect. This coupled $LiNbO_3/Si_3N_4$ OPA has an overall insertion loss of ~3.5 dB which is advantageous to silicon-on-insulator OPAs that have shown overall insertion losses of ~14 dB [48].

It was demonstrated that, by using software to control the voltage induced phase shift of the optical phased array, our edge coupled $LiNbO_3/Si_3N_4$ OPA could be phase tuned and steered to a maximum angle of approximately ±7°. While other optical phased array technologies suffer from slower steering speeds, this edge coupled approach allows for the use of the high electro-optic coefficient of $LiNbO_3$ for fast tuning and the moderately high mode confinement of the Si_3N_4 waveguides for closer waveguide spacing and a 2π-steering angle of 14°.

V.A. Future Work

This is the first optical phased array fabricated on a single $LiNbO_3$ substrate, therefore, many improvements can be made to the design for better overall performance. The two most important characteristics of OPAs are steering speed and steering angle. With the use of the electro-optic properties and high electro-optic coefficient of $LiNbO_3$, the steering speed of the device is only limited by the electronics. However, the steering angle can be greatly improved. This can be accomplished by using non-uniform output arrays. By utilizing this, the number of output waveguides must also be increased. This device would have groups of waveguides at different pitches and would allow for the steering of the main lobe throughout the entire element factor by suppressing the grating lobes. As seen in Fig. 79, the layout of this 16 output OPA has 4 different array groups each having a different pitch.

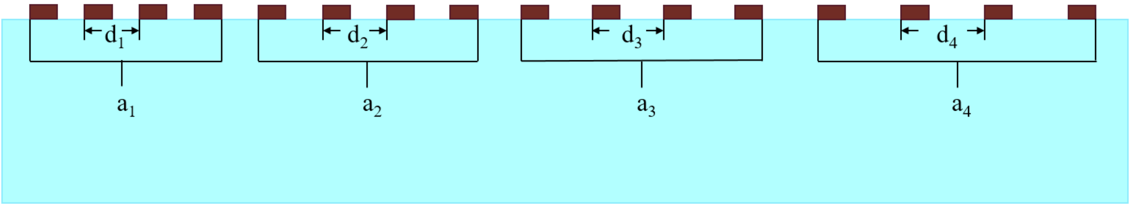

Fig. 79 Edge view of non-uniform output waveguide array for wide angle NMBS.

Both the hybrid As_2S_3-$LiNbO_3$ and the edge coupled $LiNbO_3$/Si_3N_4 optical phased arrays only steer in the horizontal direction. This can be improved by bringing a second vertical steering direction into play. Two-dimensional NMBS can be accomplished by two different techniques. The first way would be to overlay a grating on top of the output waveguides as seen in Fig. 80. This would cause the guided light to be out-coupled in a vertical or nearly vertical direction. Steering in the horizontal direction would be accomplished in the same way as before with electro-optic tuning. Steering in the vertical direction would be accomplished by wavelength tuning due to the wavelength dependence of the grating structure. The grating structure would need to a weak grating which would require it to have a long length in order to achieve a small beam divergence. The steering due to electro-optic phase tuning would occur in the horizontal x-z plane or the ψ-direction and the steering due to wavelength tuning would occur in the vertical x-y plane or the θ-direction.

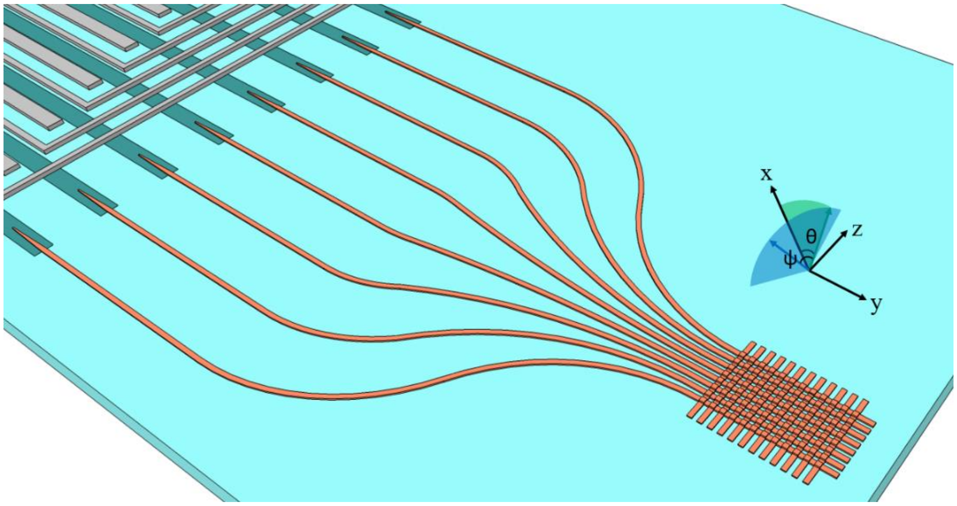

Fig. 80 Hybrid As_2S_3-$LiNbO_3$ optical phased array with grating overlay for two-dimensional beam steering.

The second technique that could be employed for two-dimensional beam steering would be to create a grating coupler for each output element which would form a two dimensional array. This would allow for the beam to be non-mechanically steered in two-dimensions by only electro-optic phase tuning for true beam steering. This, although, would increase the number of output waveguides by 2N or more in order to achieve the same steering results as previously in the one-dimensional case. The grating couplers would need to be designed in such a way that there was high-resolution in the far-field with low beam divergence. As can be seen in Fig. 81, this device would consist of a 4x4 grating coupler array in which each would be individually tuned electro-optically.

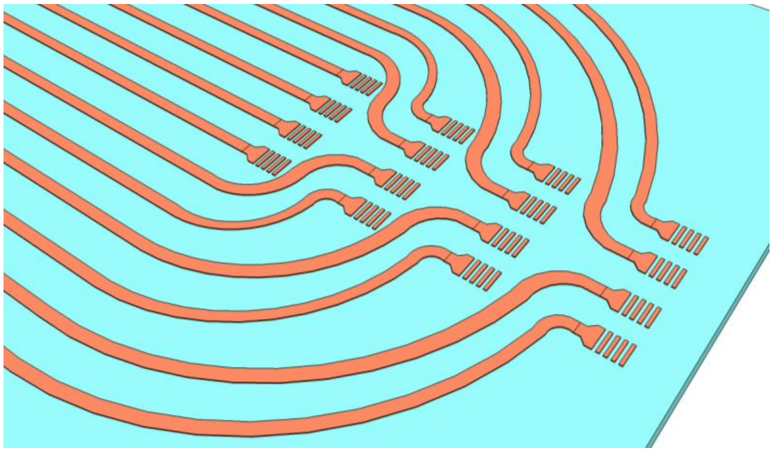

Fig. 81 Hybrid As_2S_3-$LiNbO_3$ optical phased array composed of a 4x4 grating coupler array.

In order to reduce the fabrication length and complexity, the proton exchange step could be eliminated entirely. A grating coupler specifically designed to couple light from a single mode fiber could be used at the input [49]. This would eliminate the need of aligning a fiber array to the input waveguides and allow for a large number of output waveguides to be realized. Because this design would only have one input waveguide, it would need a means of splitting the input power into a large number of output array elements. This could be accomplished by using a multimode interference coupler as seen in Fig. 82. To get a 16 output grating array, a two-stage 1x4 MMI array could be used where the outputs from the first MMI coupler would go to the inputs of four other 1x4 MMI couplers.

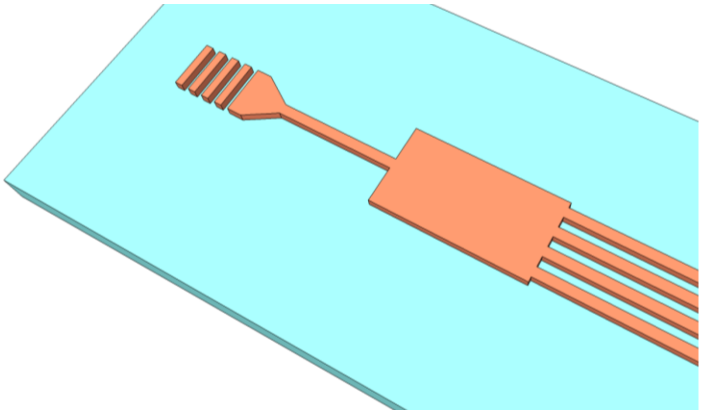

Fig. 82 Hybrid As_2S_3-$LiNbO_3$ optical phased array input that is composed of a grating coupler and a 1x4 MMI coupler.

An As_2S_3 MMI was designed and simulated as first steps in this improvement process. The light intensity pattern of a 1x4 As_2S_3 MMI can be seen in Fig. 83 along with the output field distribution. This device has single mode input and output waveguides that have a width of 2.4 µm and height of 0.3 µm. The MMI waveguide has a width of 40 µm, length of 596 µm, and height 0.3 µm. The efficiency of this device was calculated to be 94%.

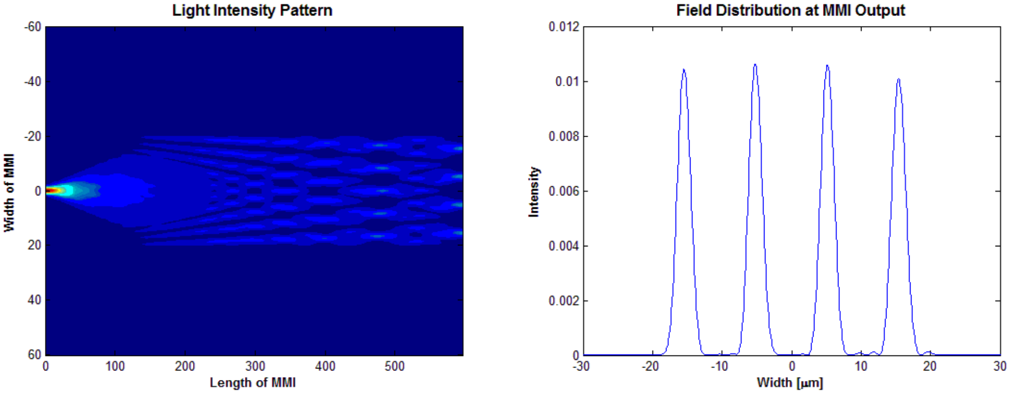

Fig. 83 (a) Light intensity pattern of 1x4 As_2S_3 MMI and (b) the output field distribution.

This design would still be able to take advantage of the electro-optic properties of $LiNbO_3$ because the As_2S_3 waveguides could be designed to allow a percentage of the optical mode to remain in the substrate. Fig. 84 displays the simulated mode profile of an As_2S_3 single mode waveguide with a height of 0.3 µm and a width of 2.4 µm. As is evident, much of the mode is still in the $LiNbO_3$ substrate with the mode having a confinement factor of 41.4% in the As_2S_3. This allows the mode to still be electro-optically tuned even though it is not being guided in the $LiNbO_3$.

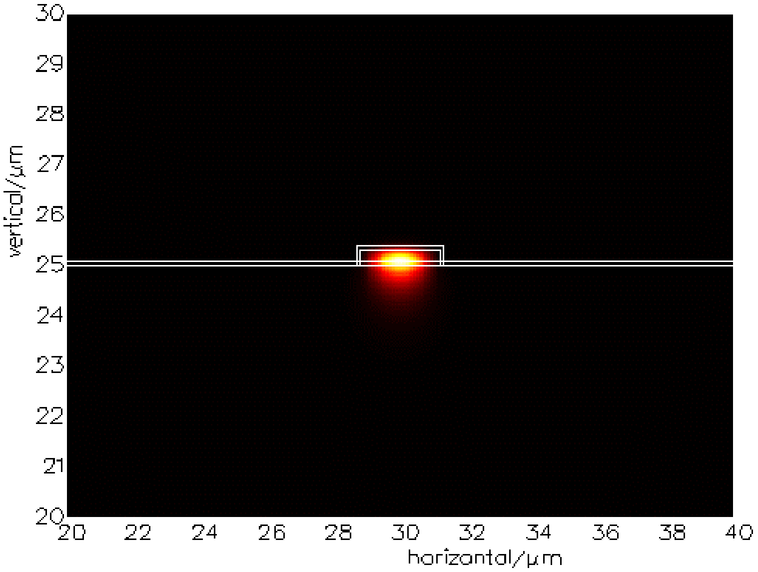

Fig. 84 Simulated mode profile for As_2S_3 waveguide with a height of 0.3 µm and a width of 2.4 µm.

REFERENCES

[1] B. Yoo, M. Megens, T. Chan, T. Sun, W. Yang, et *al.*, “Optical phased array using high contrast gratings for two dimensional beamforming and beamsteering,” *Opt. Exp.*, vol. 21, no. 10, pp. 12238-12248, 2013.

[2] D. P. Resler, D. S. Hobbs, R. C. Sharp, L. J. Friedman, and T. A. Dorschner, “High-efficiency liquid-crystal optical phased-array beam steering,” *Opt. Lett.*, vol. 21, no. 9, pp. 689-691, 1996.

[3] J. Kim, C. Oh, M. J. Escuti, L. Hosting, and S. Serati, “Wide-angle, nonmechanical beam steering using thin liquid crystal polarization gratings,” *Proc. SPIE*, vol. 7093, pp. 709302-1 – 709302-12, 2008.

[4] J. Sun, E. Timurdogan, A. Yaacobi, E. S. Hosseini, and M. R. Watts, “Large-scale nanophotonic phased array,” *Nature*, vol. 493, pp. 195-199, 2013.

[5] K. Van Acoleyen, H. Rogier, and R. Baets, “Two-dimensional optical phased array antenna on silicon-on-insulator,” *Opt. Exp.*, vol. 18, no. 3, pp. 13655-13660, 2010.

[6] J. K. Doylend, M. J. R. Heck, J. T. Bovington, J. D. Peters, L. A. Coldren, et *al.*, “Two-dimensional free-space beam steering with an optical phased array on silicon-on-insulator,” *Opt. Exp.*, vol. 19, no. 22, pp. 21595-21604, 2011.

[7] D. Kwong, A, Hosseini, Y. Zhang, J. Covey, X. Xu, et *al*, “Steerable free space optical interconnect with corrugated waveguide gratings optically isolated by 2D photonic crystal,” *IEEE*, pp. 64-65, 2013.

[8] D. Kwong, A. Hosseini, J. Covey, Y. Zhang, X. Xu, et *al*, “On-chip silicon optical phased array for two-dimensional beam steering,” *Opt. Lett.*, vol. 39, no. 4, pp. 941-944, 2014.

[9] B. Abiri, F. Aflatouni, A. Rekhi, and A. Hajimiri, “Electronic two-dimensional beam steering for integrated optical phased arrays,” *Opt. Soc. Am.*, 2014.

[10] F. Aflatouni, B. Abiri, A. Rekhi, and A. Hajimiri, “Nanophotonic projection system,” *Opt. Exp.*, vol. 23, no. 16, pp. 21012-21022, 2015.

[11] D. N. Hutchison, J. Sun, J. K. Doylend, R. Kumar, J. Heck, et *al*, “High-resolution aliasing-free optical beam steering,” *Optica*, vol. 3, no. 8, pp. 887-890, 2016.

[12] A. Leinse, R. G. Heideman, M. Hoekman, F. Schrueder, F. Falke, et *al*, "Triplex^{TM} waveguide platform: low-loss technology over a wide wavelength range," *Proc. SPIE*, vol. 8767, pp. 87670E-1 – 87670E-13, 2013.

[13] L. Zhuang, M. Burla, C. G. H. Roeloffzen, A. Meijerink, D. A. I. Marpaung, et *al*, “RF-to-RF characterization of a phased array receive antenna steering system using a novel ring resonator-based integrated photonic beamformer,” *IEEE*, 2009.

[14] H. Schippers, J. Verpoorte, P. Jorna, A. Hulzinga, L. Zhuang, et *al*, “Broadband optical beam forming for airborne phased array antenna,” *IEEE*, pp. 1-19, 2009.

[15] J. Verpoorte, H. Schippers, P. Jorna, A. Hulzinga, C. G. H. Roeloffzen, et *al*, “Development of the SANDRA antenna for airborne satellite communication,” *IEEE*, pp. 1-15, 2011.

[16] K. Horikawa, Y. Nakasuga, and H. Ogawa, "Self-heterodyning optical waveguide beam forming and steering network integrated on lithium niobate substrate," *IEEE Trans. Micro. Theo. Tech.*, vol. 43, no. 9, pp. 2395-2401, 1995.

[17] X. Zhang, D. Yang, D. Wang, S. Zhao, and Z. Wang, "Beam steering by phase control based on lithium niobate in laser-phased-array," *Proc. SPIE*, vol. 8192, pp. 819228-1 – 819228-6, 2011.

[18] W. R. Huang, J. Montoya, J. E. Kansky, S. M. Redmond, G. W. Turner, et *al*, "High speed, high power one-dimensional beam steering from a 6-element optical phased array," *Opt. Exp.*, vol. 20, no. 16, pp. 17311-17318, 2012.

[19] D. Yang, Z. Yang, and D. Wang, "Laser-phased-array beam steering controlled by lithium niobate waveguides," *Opt. Eng.*, vol. 53, no. 6, pp. 061605-1 – 061605-5, 2014.

[20] D. D. Macik and C. K. Madsen, "Fabrication of $LiNbO_3$-As_2S_3 waveguides for beam steering applications," *Proc. SPIE*, vol. 9970, pp. 99700H-1 – 99700H-10, 2016.

[21] D. D. Macik, T. E. Bravo, S. M. Pentecost, F. A. Espinal, and C. K. Madsen, "Optimization of electro-optic phase shifters for integrated optical phased arrays," *Proc. SPIE*, vol. 10181, pp. 1018105-1 – 1018105-10, 2017.

[22] W. Guo, P. R. A. Binetti, J. Althouse, H. P. M. M. Ambrosius, L. A. Johansson, et *al*, "Very fast ($>10^7$ degrees/s) 2D optical beam steering through an InP photonic integrated circuit," *IEEE*, pp. 842-843, 2012.

[23] D. K. Cheng, Fundamentals of Engineering Electromagnetics. New Jersey: Prentice Hall, 1993.

[24] R. S. Weis and T. K. Gaylord, “Lithium niobate: Summary of physical properties and crystal structure,” *Appl. Phys. A*, vol. 37, no. 4, pp. 191-203, Aug. 1985.

[25] K. Nassau and H. J. Levinstein, “Ferroelectric behavior of lithium niobate,” *Appl. Phys. Lett.*, vol. 7, no. 3, pp. 69-70, Aug. 1965.

[26] H. Nishihara, M. Haruna, and T. Suhara, Optical Integrated Circuits. New York: McGraw-Hill, 1989.

[27] L. Arizmendi, “Photonic applications of lithium niobate crystals,” *Phys. Stat. Sol.* (a), vol. 201, no. 2, pp. 253-283, Jan. 2004.

[28] D. E. Zelmon, D. L. Small, and D. Jundt, “Infrared corrected sellmeier coefficients for congruently grown lithium niobate and 5 mol. % magnesium oxide-doped lithium niobate,” *J. Opt. Soc. Am. B*, vol. 14, no. 12, pp. 3319-3322, December 1997.

[29] D. S. Smith, H. D. Riccius, and R. P. Edwin, “Refractive indices of lithium niobate,” *Opt. Comm.*, vol. 17, no. 3, pp. 332-335, Jun. 1976.

[30] G. J. Edwards and M. Lawrence, "A temperature-dependent dispersion equation for congruently grown lithium niobate," *Opt. and Quant. Elec.*, vol. 16, no. 4, pp. 373-375, Jul. 1984.

[31] E. H. Turner, “High-frequency electro-optic coefficients of lithium niobate,” *Appl. Phys. Lett.*, vol. 8, no. 11, pp. 303-304, June 1966.

[32] E. A. J. Marcatili, “Dielectric rectangular waveguide and directional coupler for integrated optics,” *Bell Systems Technology Journal*, vol. 48, no. 21, pp. 2071-2102, Sep. 1969.

[33] R. M. Knox and P. P. Toulios, “Integrated circuits for the millimeter through optical frequency range,” presented at the Symposium on Submillimeter Waves, Polytechnic Institute of Brooklyn, 1970.

[34] H. Chung, W. S. C. Chang, and E. L. Adler, “Modeling and optimization of traveling-wave $LiNbO_3$ interferometric modulators,” *J. Quant. Elec.*, vol. 27, no. 3, pp. 608-617, Mar. 1991.

[35] W. K. Burns, M. M. Howerton, R. P. Moeller, R. Krahenbuhl, R. W. McElhanon, et al., “Low drive voltage, broad-band $LiNbO_3$ modulators with and without etched ridges,” *J. Light. Tech.*, vol. 17, no. 12, pp. 2551-2555, Dec. 1999.

[36] M. M. Howerton and W. K. Burns, “Broadband traveling wave modulators in LiNbO3,” *RF Photonic Technology in Optical Fiber Links.* West Nyack, NY: Cambridge University Press, pp. 133-164, 2002.

[37] R. C. Alferness, “Waveguide electrooptic modulators,” *IEEE Trans. Micro. Theory and Techniques*, vol. 30, no. 8, pp. 1121-1137, Aug. 1982.

[38] C. T. Lee, M. L. Wu, L. G. Sheu, P. L. Fan, and J. M. Hsu, “Design and analysis of completely adiabatic tapered waveguides by conformal mapping,” *J. Light Tech.*, vol. 15, no. 2, pp. 403-410, Feb. 1997.

[39] M. E. Solmaz, D. B. Adams, S. Grover, W. C. Tan, X. Xia, et *al.*, “Compact bends for achieving higher integration densities for LiNbO3 waveguides,” *Phot. Tech. Lett.*, vol. 21, no. 9, pp. 557-559, May 2009.

[40] C. H. Bulmer, W. K. Burns, and T. G. Giallorenzi, “Performance criteria and limitations of electrooptic waveguide array deflectors,” *Appl. Opt.*, vol. 18, no. 19, pp. 3282-3295, 1979.

[41] J. A. Thomas and Y. Fainman, “Optimal cascade operation of optical phased-array beam deflectors,” *Appl. Opt.*, vol. 37, no. 26, pp. 6196-6212, 1998.

[42] J. L. Jackel, C. E. Rice, and J. J. Veselka, “Proton exchange for high-index waveguides in $LiNbO_3$,” *Appl. Phys. Lett.*, vol. 41, no. 7, pp. 607-608, 1982.

[43] A. Yi-Yan, “Index instabilities in proton-exchanged $LiNbO_3$ waveguides,” *App. Phys. Lett.*, vol. 42, no. 8, pp. 633-635, 1983.

[44] P. G. Suchoski, T. K. Findakly, and F. J. Leonberger, “Stable low-loss proton-exchanged $LiNbO_3$ waveguide devices with no electro-optic degradation,” *Opt. Lett.*, vol. 13, no. 11, pp. 1050-1052, 1988.

[45] M. De Micheli, J. Botineau, S. Neveu, P. Sibillot, and D. B. Ostrowsky, “Independent control of index profiles in proton exchanged lithium niobate guides,” *Opt. Lett.*, vol. 8, no. 2, pp. 114-115, 1983.

[46] C. Zhang, “Efficient light coupling for grating cavity using arsenic trisulfide grating coupler”, Ph.D. dissertation, Dept. Elect. And Comp. Eng., Texas A&M Univ., College Station, TX, 2017.

[47] N. Le Thomas, R. Houdre, M. V. Kotlyar, D. O'Brien, and T. F. Krauss, "Exploring light propagating in photonic crystals with Fourier optics," *J. Opt. Soc. Am. B*, vol. 24, no. 12, pp. 2964-2971, 2007.

[48] D. Kwong, A. Hosseini, J. Covey, X. Xu, Y. Zhang, et *al* "Corrugated waveguide-based optical phased array with crosstalk suppression," Ph. Tech. Let., vol. 26, no. 10, pp. 991-994, 2014.

[49] C. Zhang and C. K. Madsen, "Demonstration of an As_2S_3-on-$LiNbO_3$ grating coupler and its application of measuring a grating-based filter," *IEEE Phot. J.*, vol. 8, no. 6, 2016.

APPENDIX A

FABRICATION PROCEDURE

A.A. APE Waveguide Fabrication

- **SiO_2 Mask Layer Deposition**
  - Sputter 1500 Å SiO_2 on $LiNbO_3$ substrate

- **Lithography**
  - Clean Sample
    - *Rinse w/ acetone*
    - *Rinse w/ methanol*
    - *Rinse w/ isopropanol*
    - *Dry w/* N_2
  - Apply Photoresist
    - *Spin AZ5214 @ 4000 RPM for 40 sec w/ 5 sec ramp up/ramp down time*
    - *Soft bake on hotplate for 1 min 15 sec @ 125°C*
  - Photolithography
    - *Align waveguides w/ sample*
    - *Expose @ 85* mJ/cm^2
    - *Develop w/ AZ726 Developer*
    - *Check under microscope that development is complete; if not, develop longer*
    - *Hard bake for 8 min @ 135°C in oven*

- **Etch**
  - Use RIE to open channels in SiO_2
  - Remove undeveloped photoresist with AZ400T photoresist stripper

- **Proton Exchange**
    - Fill 100 mL beaker with 80 mL of benzoic acid and cover with Al foil
    - Fill 300 mL beaker with 150 mL of DI-water
    - Place on hotplate and set temp. @ 200°C
        - *Place thermal probe in water until BA is melted*
        - *Wait ~20 min for BA to melt*
    - Place magnetic stirrer in BA melt
        - *Stir @ 60 RPM*
    - Cover BA beaker with insulator sleeve
        - *Place thermal probe in lid opening of sleeve so that it is immersed in the BA melt*
    - When BA reaches 200°C place sample on sample holder
        - *Hold above acid for 1-2 min to avoid thermal shock*
    - Place sample in BA for 30 min
        - *Close thermal sleeve with clamp*
    - Remove sample from BA
        - *Hold above acid for 1-2 min to avoid thermal shock*
        - *Place on beta wipe and wait until cooled to room temp.*
        - *Turn off hotplate and dispose BA*
    - Clean sample with isopropanol
        - *If benzoic acid remains on sample use q-tip to remove*
        - *Dry w/* N_2

- **Anneal**
    - Before PE process turn on diffusion furnace
        - *Set to 400°C*
        - *Flow dry breathing air @ 30 sccm*
    - Place sample on boat
        - *Set boat in furnace at the edge for ~5 min*
        - *Slowly push boat with quartz rod to center of furnace to avoid thermal shock*
    - Anneal for 1 hr 45 min @ 400°C
        - *After time has expired turn off furnace and air flow*
        - *Allow to cool to room temp. ~4 hrs*
    - Remove from furnace

- **Polish Sample**
    - Turn on DI-water flow
    - Polish samples with diamond grit polishing pads while checking sample progress after each step
        - *15 µm pad: 2 min @ 135 RPM*
        - *3 µm pad: 2 min @ 85 RPM*
        - *0.5 µm pad: 2 min @ 55 RPM*
    - Clean sample w/ acetone, methanol, and isopropanol. Dry with N_2

A.B. As_2S_3 Waveguide Fabrication

- **SiO_2 Mask Clean-up**
  - Perform photolithography with SiO_2 clean-up mask
    - *Follow same steps as above*
    - *Do not hard bake*

- **Etch**
  - Use BOE to remove unwanted SiO_2
    - *Use slight agitation*
  - Remove remaining photoresist w/ acetone
  - Clean w/ acetone, methanol, and isopropanol
  - Dry with N_2

- **As_2S_3/Protective Layer Deposition**
  - Sputter 600 nm As_2S_3 on APE:$LiNbO_3$ substrate
  - Deposit 1500 Å SiO_2
  - Deposit 450 Å Ti

- **Lithography**
  - Perform photolithography with W alignment mark mask
    - *Follow same steps as above*
    - *Do not hard bake*

- **W Deposition**
  - Deposit 2500 Å W

- **Lift-off**
  - Perform lift-off to develop W alignment marks
    - *Fill 150 mL beaker w/ 50 mL of acetone*
    - *Suspend sample upside down in beaker for 3 min using tweezers*
    - *Place beaker w/ sample inside sonicator for an additional 3 min*
  - Remove sample from acetone
  - Clean sample with acetone, methanol, and isopropanol
  - Dry with N_2

- **E-beam Lithography**
    - Apply Resist
        - *Spin PMMA @ 2500 RPM for 1 min*
        - *Soft bake on hotplate for 2 min @ 180°C*
    - Place sample in piece-wise holder
    - Place piece-wise holder in loading chamber
    - Load sample into main chamber
    - Align GDSII mask with W alignment marks
    - Expose @ 350 $\mu C/cm^2$
    - Develop with mixture of 100 mL IPA and 50 DI-water for 1 min
        - *Slightly agitate throughout process*
    - Check under microscope that development is complete; if not, develop longer

- **O_2 Ash**
    - Perform oxygen ashing to remove residual resist for 5 sec

- **Cr Deposition**
    - E-beam evaporate 30 nm Cr

- **Lift-off**
    - Perform lift-off of Cr
        - *Follow same steps as above*

- **Etch**
    - Use RIE to etch As_2S_3 and protective layer
    - Use BOE to remove protective layer from As_2S_3
    - Use Cr etch to remove residual Cr

- **SiO_2 Buffer Layer Deposition**
    - Sputter 1500 Å SiO_2 to be used as buffer layer

A.C. Al Electrode Fabrication

- **Al Deposition**
    - Sputter 500 nm Al on sample

- **Lithography**
    - Perform photolithography with Al electrode mask
        - *Follow same steps as above*
        - *Do not hard bake*

- **Etch**
  - Use Al etch to etch Al for ~10 min
    - *Use slight agitation*
  - Remove remaining photoresist w/ acetone
  - Clean w/ acetone, methanol, and isopropanol
  - Dry with N_2

APPENDIX B

MATLAB CODE FOR SIMULATIONS

B.A. Mode Profile Simulations

```
%clc;
%clear all, close all;

%% Change Settings

% Exchange Region
width = 7;  % um

% Anneal Temperature
TC= 400;    % deg C
% Anneal Time
t= 2.5;       % hours

% Exchange Temperature
t1= 200;    % deg C


%% PE initial step Diffusion Coeff II

%***constants from Almeida et al.
% Do= 0.48e8; %um^2/hr for Benzoic Acid
% Q= 77.4e3; %J/mol
% R= 8.314472; %J/(mol*K)

%***constants from Wong et al.
% Do= 4.326e8; %um^2/hr for Benzoic Acid
% Q= 84e3; %J/mol
% R= 8.314472; %J/(mol*K)

    %***constants from Loni
Do= 1.468e8; %um^2/hr for Benzoic Acid
Q= 79.3e3; %J/mol
R= 8.314472; %J/(mol*K)

TCe=160:260;
T= TCe+273.15;
De= Do*exp(-Q./(R*T));

figure(1)
plot(TCe,De)
```

```
Title('H^+ proton diffusion of Benzoic Acid in LiNbO3, x dir
(Almeida,2007)');
xlabel('Temp deg \circC');
ylabel('Diffusion Coff De [\mum^2/h]');
%% PE step depth estimate
te= 1:60;  %time (min)
de=sqrt(4*De(t1-159)*te/60);

figure(2)
plot(te,de)
xlabel('Exchange time [min]'),ylabel('d_e [\mum]');
title(['Diffusion depth of PE in pure BA at ',num2str(t1),'\circC,
(Almeida,2007)']);

dummy = input('Select data point for diffusion, p1');

%% Annealed index in X and Z direction
%use diffusion coefficients from Almeida 2007
%Samples are X cut, y propagating.  Diffusion toward mask borders is in
z direction
%need a vector for x and y directions, distribution is a product of the
two

K= 8.617385e-5; %Boltzman const, [eV/K]
lambda=1531e-3;  %wavelength in um
%modified Sellmier EQ
ne= sqrt(4.5820- 0.099169/(0.04432-lambda^2) -0.021950*lambda^2);
nsub= ne; %substrate index (n_e extraordinary), (from Abouelleil 1989)
dn_pp= 0.096;  %wavelength dependent index change for initial PE layer,
1550nm

h= p1.Position(2);  %initial exchange depth [um](same as 'de')

w= width/2; %divide width by 2
T= TC+273.15;

% ---------- Almeida findings, Xcut diffusion
Dox= 22.0e12;  %x cut diffusion coeff[um^2/h],as reported by Almeida
Hx= 1.77;  %eV
Dx= Dox*exp(-Hx/(K*T));
% ---------- Almeida findings, Z direction diffusion
Doz= 0.44e12;  %z cut diffusion coeff[um^2/h],as reported by Almeida
Hz= 1.5;  %eV,   %1.77 yields square profile
Dz= Doz*exp(-Hz/(K*T));

% % ---------- Almeida ref [38], Xcut diffusion
% Dox= 0.27e12;  %x cut diffusion coeff[um^2/h],as reported by Almeida
% Hx= 1.44;  %eV
% Dx= Dox*exp(-Hx/(K*T));
% % ---------- Almeida ref [34], Z direction diffusion
% Doz= 0.01e12;  %z cut diffusion coeff[um^2/h],as reported by Almeida
% Hz= 1.21;  %eV
```

```
% Dz= Doz*exp(-Hz/(K*T));

% length(y)
Co= 0.8;

dd= 0.05;  %increment value for x and z directions

dx= 2*sqrt(Dx*t);
dz= 2*sqrt(Dz*t);
z= -7*w:dd:7*w; %plot 3x the mask width since the H+ also diffuse in y
direction
% x= -(h+da):0.05:(h+da)*2;  %visual for oval profile of WG
x= 0:dd:(h+dx)*2;

Cz= erf( (w-z)/dz) + erf( (w+z)/dz);
Cx= erf( (h-x)/dx) + erf( (h+x)/dx);

figure(3)
plot(z,Cz*Co/2);title('Index distribution in Z direction');
ylabel('Index');xlabel('Diffusion in Z direction');
figure(4);plot(x,Cx/2);title('Index distribution in X direction');
ylabel('Index');xlabel('Diffusion depth in X direction');

[X,Y]= meshgrid(Cz,Cx);  %make 2 matrices containing repeating rows or
columns of the original vectors so they may be multiplied together to
create a final visual of the 2D index profile
Z= X.*Y;

n_profile= nsub+ (dn_pp/4).*Z;   %from Almeida eq 9
% figure();imagesc(Z); axis image %visualize the concentration profile,
square pixels
figure(5);imagesc(n_profile); axis image %visualize the index profile,
square pixels
% set(gca,'ytick',[2 2.1 2.2 2.3 2.4 2.5])
% set(gca,'XTick',-pi:pi/2:pi)
%set(gca,'xtick',[0 w/dd 2*w/dd 3*w/dd 4*w/dd 5*w/dd 6*w/dd])
%set(gca,'XTickLabel',{'-3w','-2w','-w','0','w','2w','3w'})
% set(gca,'yTickLabel',{'-3w','-2w','-w','0','w','2w','3w'})
title(['index distribution for mask window w=
',num2str(width),'\mum']);
xlabel([num2str(t),'hour anneal @',num2str(TC),'\circC']);
ylabel('Z Direction');

num_out = 4;
pitch = 24;
n_profile_multi =
zeros(length(n_profile(:,1)),length(n_profile)+(pitch/dd)*(num_out-1));

for a = 0:num_out-1
    n_profile_multi(:,1+a*(pitch/dd):length(n_profile)+a*(pitch/dd)) =
(n_profile-
nsub)+n_profile_multi(:,1+a*(pitch/dd):length(n_profile)+a*(pitch/dd));
```

```
end

n_profile_multi = n_profile_multi + nsub;

z2 = -(length(n_profile_multi)/20)/2:dd:(length(n_profile_multi)/20)/2;

figure(6);imagesc(z2,x,n_profile_multi);
axis image

line([-(pitch/2)-pitch-w -(pitch/2)-pitch-w],[0 190],'LineStyle','-
','LineWidth',1.5,'Color','r')
line([-(pitch/2)-pitch+w -(pitch/2)-pitch+w],[0 190],'LineStyle','-
','LineWidth',1.5,'Color','r')

line([-(pitch/2)-w -(pitch/2)-w],[0 190],'LineStyle','-
','LineWidth',1.5,'Color','r')
line([-(pitch/2)+w -(pitch/2)+w],[0 190],'LineStyle','-
','LineWidth',1.5,'Color','r')

line([(pitch/2)-w (pitch/2)-w],[0 190],'LineStyle','-
','LineWidth',1.5,'Color','r')
line([(pitch/2)+w (pitch/2)+w],[0 190],'LineStyle','-
','LineWidth',1.5,'Color','r')

line([(pitch/2)+pitch-w (pitch/2)+pitch-w],[0 190],'LineStyle','-
','LineWidth',1.5,'Color','r')
line([(pitch/2)+pitch+w (pitch/2)+pitch+w],[0 190],'LineStyle','-
','LineWidth',1.5,'Color','r')

title(['index distribution for mask window w=
',num2str(width),'\mum']);
xlabel({'\mum';[];[num2str(p1.Position(1)),' minute exchange @
',num2str(t1),'\circC'];[num2str(t),' hour anneal @
',num2str(TC),'\circC']});
ylabel('Z Direction (\mum)');

%now calculate 2D index profile

% surf(z,x,Z)

Dn_max= max(max(n_profile)) -nsub;
no = 0.007 - 0.4*Dn_max;

fprintf('\n\nExchange depth: %fum\nAnneal time: %2.1fh\nVertical
Diffusion: %f\nHorizontal Diffusion: %f\nSubstrate index: %f at
%1.3fum\nMax index change: %f\nda/de:
%f',h,t,dx+h,dz,nsub,lambda,Dn_max,dx/h)

fprintf('\n\n****FOR FIMMWAVE****\nx: %f\ny: %f\nxx: %f\nyy: 0\nzz: -
%f\n\n',dz,dx+h,Dn_max,no)
% sprintf('Anneal time: %f',t)
```

```
% sprintf('Vertical Diffusion: %f',dx)
% sprintf('Horizontal Diffusion: %f',dz)
% sprintf('Substrate index: %f at %1.3fum',nsub,lambda)
% sprintf('Max index change: %f',Dn_max)
% sprintf('da/de: %f',dx/h)
% h,t,dx,dz
%
% dx/h

%for Xiaomin's code: Dh= 5.228, Dv=4.338

% %% Anneal Diffusion Coeff and depth calcs
% % ---------- Almeida findings, Xcut diffusion
%
% K= 8.617385e-5; %Boltzman const, [eV/K]
% Dox= 22.0e12;  %x cut diffusion coeff[um^2/h],as reported by Almeida
%     Hx= 1.77;  %eV
%
% t= 0:0.1:5;
% TC1= 391;   %Temperature vector
% T1= TC1+ 273.15;  %temperature [K]
% Dx= Dox*exp(-Hx/(K*T1));
%
% da= 2*sqrt(Dx*t); %anneal depth da(Da,T)
% % plot(t,da), grid on
% % Title(['H^+ proton diffusion depth in LiNbO3 for
',num2str(TC1),'\circC anneal, x dir, from (Almeida,2007)']);
% % xlabel('Time t[h]');ylabel('Anneal Depth da [\mum]');
```

B.B. Non-mechanical Beam Steering Simulations

```
%NMBS by using OPAs

clear all
close all
clc

format long

lambda = 1.55;                  %wavelength in um
d = 2.6;%24;%2.6;               %spaceing between output waveguides in
um (24 & 2.6)
c = 1.6;%7;%1.6;%10.7;%4.15;    %waveguide width in um (7 & 1.6) MFD in
um (10.7 & 4.15)
N = 8;                          %number of output waveguides
D = (N-1)*d;                    %full phased-array aperture

z = 60000;                      %distance beam has traveled in free
space in um
dx = 0.001;                     %resolution
```

```
x = -pi:dx:pi;                   %horizontal field
dphi = 0.5*pi;

alpha = (((pi*d)/lambda)*x)-(dphi/2);
beta = (c*x)/lambda;

AF = (sin(N*alpha)./(sin(alpha))).^2;
EF = ((c/d)*sinc(beta)).^2;

I = AF.*EF;

x_z = (lambda/d);
x_b = (lambda/D);

x_z_d = (lambda/d)*(180/pi);
x_b_d = (lambda/D)*(180/pi);

figure(1)
plot(x*(180/pi),I/(max(AF)*max(EF)),x*(180/pi),EF/max(EF),'--r')
line([(-x_z/2*(180/pi)) (-x_z/2*(180/pi))],[0 1],'LineStyle','--
','Color','g')
line([(x_z/2*(180/pi)) (x_z/2*(180/pi))],[0 1],'LineStyle','--
','Color','g')
xlabel('\theta','FontSize',14,'FontWeight','b')
ylabel('Intensity (a.u.)','FontSize',14,'FontWeight','b')
title('Far Field Intensity Pattern','FontSize',16,'FontWeight','b')
xlim([-60 60])
xt=get(gca,'xtick');
for k=1:numel(xt);
xt1{k}=sprintf('%2g°',xt(k));
end
set(gca,'xticklabel',xt1);
```

B.C. Multi-mode Interferometer Simulations

(Note: Effective Index Method must be run prior to Effective Index Method – Multi)

```
%Effective Index Method
%
%          n1                            n1
%______________________          _________________            |       |
%|  ^ |         |     |                                       |       |
%|  a |    n2   |     |                  n2                   |       |
%|  _ |_________|     |    =     _________________    +    n3 | neff1 |
n3
%|     <-- b -->      |                                       |       |
%|         n3         |                  n3                   |       |
```

```
%|____________________|                                       |       |
%
%%%%%%%%%%%%%%%%%%%%%%%%%%%%%%%%%%%%%%%%%%%%%%%%%%%%%%%%%%%%%%%%%%%%%%%%
%%%%
clear all;
close all;
clc;
%%

lambda = 1.55;
n1 = 1.4440236;
n2 = 2.4373;%2.4379666;
n3 = 2.1376;%2.1378008;
a = 0.6;%0.3;%0.6;
b = 1.6;%2.4;%3.2;

k0 = (2*pi)/lambda;
h_min = sqrt((k0^2)*n2^2 - (k0^2)*n2^2);
h_max = sqrt((k0^2)*n2^2 - (k0^2)*n3^2);

hm = 0:h_max/10000:h_max;
qm = sqrt(((k0^2)*((n2^2) - (n1^2))) - hm.^2);
pm = sqrt(((k0^2)*((n2^2) - (n3^2))) - hm.^2);

LHS = tan(hm.*a);
RHS = (qm + pm)./(hm - ((qm.*pm)./hm));

%find intersecting points of eigenvalue equation (LHS=RHS) to find
allowed
%values of hm
hmm = find(abs(RHS-LHS) < 0.01);        %finds all values in the
eigenvalue
                                        %equation that are within the
given
                                        %tolerance

tt = diff(hmm);                         %calculates the difference
between
                                        %adjacent elements in array to
find
                                        %consecutive numbers
consecutive
                                        %numbers indicate the tolerance
is
                                        %too high for that region

ttt = find(tt~=1);                      %finds the array indices that
are
ttt = horzcat(ttt,length(tt));          %not equal to 1

%builds an array with the median numbers from the consecutive numbers
found
```

```
%earlier. This is an array of the allowed h indices
xx = 1;
for tttt = 1:length(ttt)
    if length(ttt) == 1
        hxtemp = round(median(hmm(ttt(tttt)+1:length(hmm))));
    elseif tttt == 1
        hxtemp(xx) = round(median(hmm(1:ttt(tttt))));
        xx = xx+1;
    else
        hxtemp(xx) = round(median(hmm(ttt(tttt-1)+1:ttt(tttt))));
        xx = xx+1;
    end
end

%gets rid of the first unwanted values which the code thinks are
allowed
%values, but are in fact not
xxx = 1;
for temp = 1:length(hxtemp)
    if hxtemp(temp)>500
        hxtemp2(xxx) = hxtemp(temp);
        xxx = xxx+1;
    end
end

%makes an array of allowed h values from the array of h value indices
xxxx = 1;
for temp2 = 1:length(hxtemp)
    if hxtemp(temp2)>500
        hx(xxxx) = hm(hxtemp(temp2));
        xxxx = xxxx+1;
    end
end

%Propagation constant for allowed h values
Bm = sqrt((k0^2)*n2^2 - hx.^2);

figure(1)
plot(hm,LHS,'.r')
hold on
plot(hm,RHS,'.b')
plot(hm(hxtemp2),RHS(hxtemp2),'og','LineWidth',3)
ylim([-10 10]); xlabel('h');
xlim([0 h_max]); ylabel('tan(ht)');
grid on

%%

h0 = hx(1);
B0 = sqrt(((k0^2)*(n2^2)) - (h0^2));
q0 = sqrt((B0^2) - ((k0^2)*(n1^2)));
p0 = sqrt((B0^2) - ((k0^2)*(n3^2)));
```

```
n_eff1 = B0/k0;

dx = 0.001;
x1 = 0+dx:dx:3*a;
x2 = -a+dx:dx:0;
x3 = -16*a:dx:-a;

xx1 = flipud(horzcat(x3,x2,x1)');

E1E = exp(-q0*x1);
E2E = (cos(h0*x2) - (q0/h0)*sin(h0*x2));
E3E = (cos(h0*a) + (q0/h0)*sin(h0*a))*exp(p0*(x3 + a));

Ey1 = flipud(horzcat(E3E,E2E,E1E)');

Ey1 = Ey1/sqrt(sum(abs(Ey1).^2));
Ey1 = Ey1/sqrt(sum(abs(Ey1).^2));

figure(2)
plot(xx1,Ey1)
title('Field Distribution For m = 0 Mode','FontSize',14)
ylabel('E_y(x)','FontSize',10)
xlabel('t[\mum]','FontSize',10)
set(gca,'XDir','reverse')
%ylim([-a 10*a])

%%


h_min2 = sqrt((k0^2)*n_eff1^2 - (k0^2)*n_eff1^2);
%h_max2 = sqrt((k0^2)*n_eff1^2 - (k0^2)*n3^2);
h_max2 = sqrt((k0^2)*n_eff1^2 - (k0^2)*n1^2);

hm2 = 0:h_max2/10000:h_max2;
%qm2 = sqrt(((k0^2)*((n_eff1^2) - (n3^2))) - hm2.^2);
%pm2 = sqrt(((k0^2)*((n_eff1^2) - (n3^2))) - hm2.^2);
qm2 = sqrt(((k0^2)*((n_eff1^2) - (n1^2))) - hm2.^2);
pm2 = sqrt(((k0^2)*((n_eff1^2) - (n1^2))) - hm2.^2);

LHS2 = tan(hm2.*b);
%RHS2 = (((n_eff1^2)/(n3^2))*pm2 + ((n_eff1^2)/(n3^2))*qm2)./(hm2 -
(((n_eff1^2)/(n3*n3))^2)*((qm2.*pm2)./hm2));
RHS2 = (((n_eff1^2)/(n1^2))*pm2 + ((n_eff1^2)/(n1^2))*qm2)./(hm2 -
(((n_eff1^2)/(n1*n1))^2)*((qm2.*pm2)./hm2));

%find intersecting points of eigenvalue equation (LHS=RHS) to find
allowed
%values of hm
hmm2 = find(abs(RHS2-LHS2) < 0.01);        %finds all values in the
eigenvalue
```

```
                                        %equation that are within the
given
                                        %tolerance

tt = diff(hmm2);                        %calculates the difference
between
                                        %adjacent elements in array to
find
                                        %consecutive numbers
consecutive
                                        %numbers indicate the tolerance
is
                                        %too high for that region

ttt = find(tt~=1);                      %finds the array indices that
are
ttt = horzcat(ttt,length(tt));          %not equal to 1

%builds an array with the median numbers from the consecutive numbers
found
%earlier. This is an array of the allowed h indices
xx = 1;
for tttt = 1:length(ttt)
    if length(ttt) == 1
        hytemp = round(median(hmm2(ttt(tttt)+1:length(hmm2))));
    elseif tttt == 1
        hytemp(xx) = round(median(hmm2(1:ttt(tttt))));
        xx = xx+1;
    else
        hytemp(xx) = round(median(hmm2(ttt(tttt-1)+1:ttt(tttt))));
        xx = xx+1;
    end
end

%gets rid of the first unwanted values which the code thinks are
allowed
%values, but are in fact not
xxx = 1;
for temp = 1:length(hytemp)
    if hytemp(temp)>500
        hytemp2(xxx) = hytemp(temp);
        xxx = xxx+1;
    end
end

%makes an array of allowed h values from the array of h value indices
xxxx = 1;
for temp2 = 1:length(hytemp)
    if hytemp(temp2)>500
        hy(xxxx) = hm2(hytemp(temp2));
        xxxx = xxxx+1;
    end
```

```
end

h02 = hy(1);
B02 = sqrt(((k0^2)*(n_eff1^2)) - (h02.^2));
%q02 = sqrt((B02^2) - ((k0^2)*(n3^2)));
%p02 = sqrt((B02^2) - ((k0^2)*(n3^2)));
q02 = sqrt((B02^2) - ((k0^2)*(n1^2)));
p02 = sqrt((B02^2) - ((k0^2)*(n1^2)));
n_eff2 = B02/k0;

dy = 0.1;
x11 = (b/2)+dy:dy:2*b;
x22 = -(b/2)+dy:dy:(b/2);
x33 = -2*b:dy:-(b/2);

xx2 = horzcat(x33,x22,x11);

H1M = (h02/q02)*exp(-q02*(x11-(b/2)));
H2M = (h02/q02)*(cos(h02*x22)/cos(h02*(b/2)));
H3M = (h02/q02)*exp(q02*(x33+(b/2)));

Ex1 = horzcat(H3M,H2M,H1M);

Ex1 = Ex1/sqrt(sum(abs(Ex1).^2));
Ex1 = Ex1/sqrt(sum(abs(Ex1).^2));

[vl,el] = min(Ex1);
smin = abs(xx2(el))-(b/2);
%smin2 = 1/(((B0(1)^2)/(k0^2))-(n3^2));
%smin3 = 1/((n_eff2^2)-(n3^2));
smin2 = 1/(((B0(1)^2)/(k0^2))-(n1^2));
smin3 = 1/((n_eff2^2)-(n1^2));

[X,Y]= meshgrid(Ex1,Ey1);  %make 2 matrices containing repeating rows
or columns of the original vectors so they may be multiplied together
to create a final visual of the 2D index profile
Z= X.*Y;

figure(3)
plot(hm2,LHS2,'.r')
hold on
plot(hm2,RHS2,'.b')
plot(hm2(hytemp2),RHS2(hytemp2),'og','LineWidth',3)
ylim([-10 10]); xlabel('h');
xlim([0 h_max2]); ylabel('tan(ht)');
grid on

xx3 = -2*b:0.001:2*b;
Ex11 = interp1(xx2,Ex1,xx3);

figure(4)
```

```
plot(xx2,Ex1)
line([-(b/2) (b/2)],[0 0],'Color','k')
title('Field Distribution For m = 0 Mode','FontSize',14)
ylabel('E_x(x)','FontSize',10)
xlabel('w[\mum]','FontSize',10)
%xlim([-2*b 2*b])
%ylim([0 b])

%%
figure(5)
imagesc(xx2,xx1,abs(Z).^2)
set(gca,'YDir','normal')
line([-(b/2) (b/2)],[0 0],'Color','k')
line([-2*b 2*b],[-a -a],'Color','k')
line([-(b/2) -(b/2)],[0 -a],'Color','k')
line([(b/2) (b/2)],[0 -a],'Color','k')
title('Input Mode Profile','fontsize',12,'fontweight','b')
xlabel('Width [\mum]','fontsize',10,'fontweight','b')
ylabel('Thickness [\mum]','fontsize',10,'fontweight','b')
%axis image







%Effective Index Method - Multi
%
%          n1                           n1
%______________________         _________________             |       |
%|  ^ |         |     |                                       |       |
%|  a |    n2   |     |                 n2                    |       |
%|  _ |_________|     |    =    _________________     +    n3 | neff1 |
n3
%|     <-- b -->      |                                       |       |
%|         n3         |                 n3                    |       |
%|____________________|                                       |       |
%
%%%%%%%%%%%%%%%%%%%%%%%%%%%%%%%%%%%%%%%%%%%%%%%%%%%%%%%%%%%%%%%%%%%%%%%%
%%%%

close all;

lambda = 1.55;
n1 = 1.4440236;
n2 = 2.4373;%2.4379666;
n3 = 2.1376;%2.1378008;
a = 0.6;%0.3;%0.6;
b = 14;%40;

k0 = (2*pi)/lambda;
```

```
h_min = sqrt((k0^2)*n2^2 - (k0^2)*n2^2);
h_max = sqrt((k0^2)*n2^2 - (k0^2)*n3^2);

hm = 0:h_max/10000:h_max;
qm = sqrt(((k0^2)*((n2^2) - (n1^2))) - hm.^2);
pm = sqrt(((k0^2)*((n2^2) - (n3^2))) - hm.^2);

LHS = tan(hm.*a);
RHS = (qm + pm)./(hm - ((qm.*pm)./hm));

%find intersecting points of eigenvalue equation (LHS=RHS) to find 
allowed
%values of hm
hmm = find(abs(RHS-LHS) < 0.01);        %finds all values in the 
eigenvalue
                                        %equation that are within the 
given
                                        %tolerance

tt0 = diff(hmm);                         %calculates the difference 
between
                                        %adjacent elements in array to 
find
                                        %consecutive numbers
consecutive
                                        %numbers indicate the tolerance 
is
                                        %too high for that region

ttt = find(tt0~=1);                      %finds the array indices that 
are
ttt = horzcat(ttt,length(tt0));          %not equal to 1

%builds an array with the median numbers from the consecutive numbers 
found
%earlier. This is an array of the allowed h indices
xx = 1;
for tttt = 1:length(ttt)
    if length(ttt) == 1
        hxtemp = round(median(hmm(ttt(tttt)+1:length(hmm))));
    elseif tttt == 1
        hxtemp(xx) = round(median(hmm(1:ttt(tttt))));
        xx = xx+1;
    else
        hxtemp(xx) = round(median(hmm(ttt(tttt-1)+1:ttt(tttt))));
        xx = xx+1;
    end
end

%gets rid of the first unwanted values which the code thinks are 
allowed
%values, but are in fact not
```

```
xxx = 1;
for temp = 1:length(hxtemp)
    if hxtemp(temp)>500
        hxtemp2(xxx) = hxtemp(temp);
        xxx = xxx+1;
    end
end

%makes an array of allowed h values from the array of h value indices
xxxx = 1;
for temp2 = 1:length(hxtemp)
    if hxtemp(temp2)>500
        hx(xxxx) = hm(hxtemp(temp2));
        xxxx = xxxx+1;
    end
end

%Propagation constant for allowed h values
Bm = sqrt((k0^2)*n2^2 - hx.^2);

figure(1)
plot(hm,LHS,'.r')
hold on
plot(hm,RHS,'.b')
plot(hm(hxtemp2),RHS(hxtemp2),'og','LineWidth',3)
ylim([-10 10]); xlabel('h');
xlim([0 h_max]); ylabel('tan(ht)');
grid on

%%

h0 = hx;
B0 = sqrt(((k0^2)*(n2^2)) - (h0.^2));
q0 = sqrt((B0.^2) - ((k0^2)*(n1^2)));
p0 = sqrt((B0.^2) - ((k0^2)*(n3^2)));
n_eff1 = B0./k0;

dy = 0.001;
x1 = 0+dy:dy:3*a;
x2 = -a+dy:dy:0;
x3 = -16*a:dy:-a;

xx1 = flipud(horzcat(x3,x2,x1)');

for z = 1:length(h0)
    E1E = exp(-q0(z)*x1);
    E2E = (cos(h0(z)*x2) - (q0(z)/h0(z))*sin(h0(z)*x2));
    E3E = (cos(h0(z)*a) + (q0(z)/h0(z))*sin(h0(z)*a))*exp(p0(z)*(x3 +
a));
    Ey(:,z) = flipud(horzcat(E3E,E2E,E1E)');
end
```

```
Ey = Ey/sqrt(sum(abs(Ey).^2));
Ey = Ey/sqrt(sum(abs(Ey).^2));

figure(2)
plot(xx1,Ey(:,1))
title('Field Distribution For m = 0 Mode','FontSize',14)
ylabel('E_y(x)','FontSize',10)
xlabel('t[\mum]','FontSize',10)
set(gca,'XDir','reverse')
%ylim([-a 10*a])

%%

h_min2 = sqrt((k0^2)*n_eff1^2 - (k0^2)*n_eff1^2);
%h_max2 = sqrt((k0^2)*n_eff1^2 - (k0^2)*n3^2);
h_max2 = sqrt((k0^2)*n_eff1^2 - (k0^2)*n1^2);

hm2 = 0:h_max2/10000:h_max2;
%qm2 = sqrt(((k0^2)*((n_eff1^2) - (n3^2))) - hm2.^2);
%pm2 = sqrt(((k0^2)*((n_eff1^2) - (n3^2))) - hm2.^2);
qm2 = sqrt(((k0^2)*((n_eff1^2) - (n1^2))) - hm2.^2);
pm2 = sqrt(((k0^2)*((n_eff1^2) - (n1^2))) - hm2.^2);

LHS2 = tan(hm2.*(b/2));
RHS2even = qm2./hm2;
RHS2odd = -hm2./qm2;

%find intersecting points of eigenvalue equation (LHS=RHS) to find
allowed
%values of hm

hmm2eventemp1 = find(abs(RHS2even(200:950)-LHS2(200:950)) < 3)+200;

hmm2eventemp2 = find(abs(RHS2even-LHS2) < 0.08); %finds all values in
the eigenvalue
                                        %equation that are within the
given
hmm2even = horzcat(hmm2eventemp1,hmm2eventemp2);%tolerance

tt1 = diff(hmm2even);                    %calculates the difference
between
                                        %adjacent elements in array to
find
                                        %consecutive numbers
consecutive
                                        %numbers indicate the tolerance
is
                                        %too high for that region

ttt = find(tt1~=1);                      %finds the array indices that
are
```

```
ttt = horzcat(ttt,length(tt1));          %not equal to 1

%builds an array with the median numbers from the consecutive numbers
found
%earlier. This is an array of the allowed h indices
xx = 1;
for tttt = 1:length(ttt)
    if length(ttt) == 1
        hytempeven =
round(median(hmm2even(ttt(tttt)+1:length(hmm2even))));
    elseif tttt == 1
        hytempeven(xx) = round(median(hmm2even(1:ttt(tttt))));
        xx = xx+1;
    else
        hytempeven(xx) = round(median(hmm2even(ttt(tttt-
1)+1:ttt(tttt))));
        xx = xx+1;
    end
end

%gets rid of the first unwanted values which the code thinks are
allowed
%values, but are in fact not
xxx = 1;
for temp = 1:length(hytempeven)
    if hytempeven(temp)>100 && hytempeven(temp)<length(hm2)-50
        hytemp2even(xxx) = hytempeven(temp);
        xxx = xxx+1;
    end
end

%makes an array of allowed h values from the array of h value indices
xxxx = 1;
for temp2 = 1:length(hytempeven)
    if hytempeven(temp2)>100 && hytempeven(temp2)<length(hm2)-50
        hyeven(xxxx) = hm2(hytempeven(temp2));
        xxxx = xxxx+1;
    end
end

hmm2oddtemp1 = find(abs(RHS2odd(9700:end)-LHS2(9700:end)) < 0.3)+9700;
hmm2oddtemp2 = find(abs(RHS2odd-LHS2) < 0.07); %finds all values in the
eigenvalue
                                        %equation that are within the
given
hmm2odd = horzcat(hmm2oddtemp2,hmm2oddtemp1);%tolerance

tt2 = diff(hmm2odd);                        %calculates the difference
between
                                        %adjacent elements in array to
find
```

```
                                        %consecutive numbers
consecutive
                                        %numbers indicate the tolerance
is
                                        %too high for that region

ttt = find(tt2~=1);                      %finds the array indices that
are
ttt = horzcat(ttt,length(tt2));          %not equal to 1

%builds an array with the median numbers from the consecutive numbers
found
%earlier. This is an array of the allowed h indices
xx = 1;
for tttt = 1:length(ttt)
    if length(ttt) == 1
        hytempodd =
round(median(hmm2odd(ttt(tttt)+1:length(hmm2odd))));
    elseif tttt == 1
        hytempodd(xx) = round(median(hmm2odd(1:ttt(tttt))));
        xx = xx+1;
    else
        hytempodd(xx) = round(median(hmm2odd(ttt(tttt-
1)+1:ttt(tttt))));
        xx = xx+1;
    end
end

%gets rid of the first unwanted values which the code thinks are
allowed
%values, but are in fact not
xxx = 1;
for temp = 1:length(hytempodd)
    if hytempodd(temp)>500 && hytempodd(temp)<length(hm2)-45
        hytemp2odd(xxx) = hytempodd(temp);
        xxx = xxx+1;
    end
end

%makes an array of allowed h values from the array of h value indices
xxxx = 1;
for temp2 = 1:length(hytempodd)
    if hytempodd(temp2)>500 && hytempodd(temp2)<length(hm2)-45
        hyodd(xxxx) = hm2(hytempodd(temp2));
        xxxx = xxxx+1;
    end
end

hy = sort(horzcat(hyeven,hyodd));
%%
h02 = hy;
B02 = sqrt(((k0^2)*(n_eff1^2)) - (h02.^2));
```

```
%q02 = sqrt((B02.^2) - ((k0^2)*(n3^2)));
%p02 = sqrt((B02.^2) - ((k0^2)*(n3^2)));
q02 = sqrt((B02.^2) - ((k0^2)*(n1^2)));
p02 = sqrt((B02.^2) - ((k0^2)*(n1^2)));
n_eff2 = B02./k0;

dx = 0.1;
x11 = (b/2)+dx:dx:1.5*b;
x22 = -(b/2)+dx:dx:(b/2);
x33 = -1.5*b:dx:-(b/2);

xx2 = horzcat(x33,x22,x11);

for z = 1:length(h02)
    if mod(z-1,2)==0
        H1M = (h02(z)/q02(z))*exp(-q02(z)*(x11-(b/2)));
        H2M = (h02(z)/q02(z))*(cos(h02(z)*x22)/cos(h02(z)*(b/2)));
        H3M = (h02(z)/q02(z))*exp(q02(z)*(x33+(b/2)));
    else
        H1M = -(h02(z)/q02(z))*exp(-q02(z)*(x11-(b/2)));
        H2M = -(h02(z)/q02(z))*(sin(h02(z)*x22)/sin(h02(z)*(b/2)));
        H3M = (h02(z)/q02(z))*exp(q02(z)*(x33+(b/2)));
    end
    Ex(z,:) = horzcat(H3M,H2M,H1M);
end

M = 14;%length(hy);         %number of modes

for m = 1:M
    Ex(m,:) = Ex(m,:)/sqrt(sum(abs(Ex(m,:)).^2));
    Ex(m,:) = Ex(m,:)/sqrt(sum(abs(Ex(m,:)).^2));
end

%%
[X,Y]= meshgrid(Ex(1,:),Ey);  %make 2 matrices containing repeating
rows or columns of the original vectors so they may be multiplied
together to create a final visual of the 2D index profile
Z= X.*Y;

figure(3)
plot(hm2,LHS2,'.r')
hold on
plot(hm2,RHS2even,'.b')
plot(hm2,RHS2odd,'.b')
plot(hm2(hytemp2even),RHS2even(hytemp2even),'og','LineWidth',3)
plot(hm2(hytemp2odd),RHS2odd(hytemp2odd),'og','LineWidth',3)
ylim([-10 22]); xlabel('h');
xlim([0 h_max2]); ylabel('tan(ht)');
grid on

figure(4)
plot(xx2,Ex(1,:))
```

```
title('Field Distribution For m = 0 Mode','FontSize',14)
ylabel('E_x(x)','FontSize',10)
xlabel('w[\mum]','FontSize',10)
%xlim([-2*b 2*b])
%ylim([-b/20 b/20])

%%
figure(5)
imagesc(xx2,xx1,abs(Z).^2)
set(gca,'YDir','normal')
line([-(b/2) (b/2)],[0 0],'Color','k')
line([-b b],[-a -a],'Color','k')
line([-(b/2) -(b/2)],[0 -a],'Color','k')
line([(b/2) (b/2)],[0 -a],'Color','k')
xlim([-b b])
%axis equal
%axis image
%%

 temp = zeros(1,length(Ex));
 temp(1,round((length(Ex)/2)-
(length(Ex1)/2)):round((length(Ex)/2)+(length(Ex1)/2))-1) = Ex1;
 Ex1 = temp;
%%
M = 14;%length(hy);          %number of modes
N = 4;

%beat length
Lpi = pi/(B02(1)-B02(2));
L1 = 72.8;%(3*Lpi)/(4*N);%73.5;
%length of MMI 1

%%
W = b;
nc = n3;
nc = n1;

We = sqrt((3*lambda*Lpi)/(4*nc));
Ww = (1/((2*N)^(1/4)))*sqrt((lambda*We)/(n_eff2(1)));

Nmax = We/(Ww+(smin2));
Sout = We/N;

%%
z1 = 0:L1/(length(xx2)-1):L1;

cm = zeros(M,1);

for m = 0:M-1
   %cm(m+1,:) =
(sum(Ex1.*Ex(m+1,:))*dx)./(sqrt(sum((Ex(m+1,:)).^2)*dx));
```

```
    cm(m+1,:) =
((sum(Ex1.*Ex(m+1,:)*dx))*(sum(Ey1.*Ey*dy)))./(sqrt((sum(((Ex(m+1,:)).^
2)*dx)*sum(((Ey).^2)*dy))*(sum((Ex1.^2)*dx)*sum(((Ey1).^2)*dy))));
end

Psi_out = zeros(length(z1),length(xx2));

for m = 0:M-1
    %Psi1 = cm(m+1,:)*Ex(m+1,:)'*exp(1i*((m*(m+2)*pi)/(3*Lpi))*z1);
    Psi1 = cm(m+1,:)*Ex(m+1,:)'*exp(-1i*(B02(m+1)-B02(1))*z1);
    Psi_out = Psi_out + Psi1;
end

z2 = 0:300/(length(xx2)-1):300;
Psi2 = Ex1'*exp(1i*((0*(0+2)*pi)/(3*300))*z2);

for q = 0:(N/2)-1
    theta_q(q+1) = (-B02(1)*L1) + (((N-2-((4*q)*(q+1)))/(4*N))*pi);
end

%%
figure(6)
%imagesc(horzcat(fliplr(-
z2(2:length(z2))),z1),xx2,cat(2,fliplr((abs(Psi2(:,1:length(Psi2)-
1)).^2)/max(max(abs(Psi2).^2))),(abs(Psi_out).^2)/max(max(abs(Psi_out).
^2))));
imagesc(z1,xx2,(abs(Psi_out).^2)./(max(max(abs(Psi_out).^2))));
% imagesc(fliplr(-z2),xx2,(abs(Psi2).^2)/max(max(abs(Psi2).^2)));
% line([-100 0],[-(3.5/2) -(3.5/2)],'Color','k')
% line([-100 0],[(3.5/2) (3.5/2)],'Color','k')
% line([0 0],[-(b/2) -(3.5/2)],'Color','k')
% line([0 0],[(3.5/2) (b/2)],'Color','k')
% line([0 L1],[-(b/2) -(b/2)],'Color','k')
% line([0 L1],[(b/2) (b/2)],'Color','k')
% xlim([-100 L1])
title('Light Intensity Pattern','fontsize',12,'fontweight','b')
xlabel('Length of MMI','fontsize',10,'fontweight','b')
ylabel('Width of MMI','fontsize',10,'fontweight','b')

%length(Psi_out)

figure(7)
plot(xx2,abs(Psi_out(:,length(Psi_out))).^2)
title('Field Distribution at MMI
Output','fontsize',12,'fontweight','b')
xlabel('Width [\mum]','fontsize',10,'fontweight','b')
ylabel('Intensity','fontsize',10,'fontweight','b')
xlim([-b+5 b-5])
%xlim([-b+10 b-10])
```

B.D. Pixel to Angle Conversion

```
%Pixel to angle conversion

close all
clear all
clc

nf = imread('data');
ff_middle = dlmread('data');
ff_steered = dlmread('data');

y = 493;                  %y position of near field

pp = 34;                  %pitch of near-field output beams in pixels
ps = 3.75;                %size of each pixel (um). total size of array:
1348 x 976
                          % chip size: 6.26mm x 5.01mm
p = 6.2;                  %pitch of output waveguides (um)

mag = (pp*ps)/p;          %actual magnification of near field output

fd = 150000;              %design focal length of microscope objective in
um
Md = 40;                  %design magnification of microscope objective

ft = (mag*fd)/Md;         %tube lens focal length in um
z = ft;                   %distance beam has traveled in free space in um

dp = ff_middle(:,1);      %distance of y-axis in pixels
d = dp.*ps.*mag;          %distance of y-axis in um
theta = atand(d./z);      %distance of y-axis in degrees

figure(1);
imshow(nf)

figure(2);
plot(theta,ff_middle(:,2)/max(ff_middle(:,2)))
xlabel('\theta','FontSize',12,'FontWeight','b')
ylabel('Intensity (a.u.)','FontSize',12,'FontWeight','b')
title('Far Field Intensity Pattern','FontSize',14,'FontWeight','b')
xlim([-30 30])
xt=get(gca,'xtick');
for k=1:numel(xt);
xt1{k}=sprintf('%2g°',xt(k));
end
set(gca,'xticklabel',xt1);
```

```
figure(3);
plot(theta,ff_steered(:,2)/max(ff_steered(:,2)))
xlabel('\theta','FontSize',12,'FontWeight','b')
ylabel('Intensity (a.u.)','FontSize',12,'FontWeight','b')
title('Far Field Intensity Pattern','FontSize',14,'FontWeight','b')
xlim([-30 30])
xt=get(gca,'xtick');
 for k=1:numel(xt);
xt1{k}=sprintf('%2g°',xt(k));
end
set(gca,'xticklabel',xt1);

nf2 = im2double(nf(y,:));

figure(4);
plot(nf2/max(nf2))
xlabel('Pixels (a.u.)','FontSize',12,'FontWeight','b')
ylabel('Intensity (a.u.)','FontSize',12,'FontWeight','b')
title('Near Field Intensity Pattern','FontSize',14,'FontWeight','b')
xlim([400 850])
ylim([0 1.1])
```